Modified Natural Fibers and Green Composites for Sustainable Applications

by

Louise C. Batta

A dissertation submitted in partial fulfillment
of the requirements for the degree of
Doctor of Philosophy
(Materials Science and Engineering)
in the University of Michigan
2026

Doctoral Committee:

Professor Alan Taub, Chair
Professor Mihaela Banu
Professor Brian Love
Professor Erik Nielsen

Louise C. Batta

lcbatta@umich.edu

ORCID iD: 0000-0003-1247-2139

© Louise C. Batta 2026

Dedication

To Bill, Ed, and especially to Sasha.

Acknowledgements

Many cultures have words for the type of benevolence that has befallen me over the course of my PhD. Whether it be ‘blessings’ or ‘good fortune’, I have had the opportunity to be enriched with a large community of people that ensured the success of my PhD, even when I myself did not ensure my own success. To begin, I must thank my committee, who I can say with confidence has been a part of each step along my journey. My thanks go to Professor Brian Love, who was one of the first faculty members I talked to at the University of Michigan, who initially piqued my interest in this world of materials science of sustainable outcomes. To Professor Erik Nielsen, and his tenacity for plant biology; he assured that I have a necessary background for my work and was instrumental of my understanding of my work. To Professor Mihaela Banu who did the same, with respect to mechanical engineering, and who also went to bat for me in my pursuit of my goals after my PhD, putting so many professional opportunities in front of me that went on to shape my future goals. I have the most immense gratitude for my advisor, Professor Alan Taub. Joining the Taub Lab altered the course of my PhD and ultimately my life. His dedication to his students, to my research, and development, set me on a course for success that I would not have received elsewhere. Works cannot express the value of this, so the best I can say is: thank you. Very much, thank you.

I must also thank the staff in the Materials Science department for all of the work they did to make this PhD a success—and it was a lot because the researcher was demanding. I must thank Dr. Sahar Farjami, Dr. Ying Qi, and Dr. Xiang Gao for the help they have provided me on

instrumentation in Van Vlack Laboratories. Thanks to Jack Eilers, not just for his work as a staff member in Van Vlack, but for his mentorship on experimentation and testing, and for being someone I can rely on in the department. The MSE department staff were also extremely critical in this work. While all of the staff were instrumental, I thank Renee Hilgendorf, Kristen Freshley, Shelley Fellers, and Tina Longenbarger for all of their help with the administrative aspects related to the pursuit of this academic research. Ellen Kampf: *no meeting*, no gathering, and research would not have happened without her intercession. Lastly, I would like to thank D. Todd Richardson for his advice, his power of the purse, and his willingness to listen to student voices and improve the student experience. Alongside Department Chair Dr. Liz Holm, I am grateful that I could be a part of improving the department I was fortunate to call home.

I would like to thank our collaborators who provided financial and material support for the research conducted in pursuit of this dissertation. The utmost thanks go to Angela Wartes-Kahl, Shannon Welsh, Dr. Jennifer Kling, and Will Altshwager at Coast Fibers who have been incredibly supportive and involved in our progress. I would also like to thank Brian Beimel and Emily Cieslinski and everyone at PulFlex for their help with a very arduous task and chapter. Thank you to Dr. Ali Zolali and Dr. Elias Shakur at BASF, who provided both material support but also professional support, introducing to opportunities for growth.

In 2022, after my mother was diagnosed with Stage 1 breast cancer, I seriously considered leaving the PhD program. Dr. Wenhao Sun reminded me of how much of a disappointment this would be for the department. I would like to thank all the people who reinforced that my grass was greener where it was watered. My research group—past and present, my friends across MSE and other departments in engineering, Slow Start, Club Gymnastics, Ann Arbor Rec and Ed Volleyball, Milan Volleyball and HVVC, my family and friends here and around to world: Thank you.

Table of Contents

Dedication ii

Acknowledgements iii

List of Tables viii

List of Figures ix

List of Appendices xv

Abstract xvi

Chapter 1 Introduction 1

1.1 Dissertation Outline 18

Chapter 2 Modification and Enhancement of Growth of Flax Plants via Nanocellulose 20

2.1 Materials and Methods 20

2.1.1 Preparation of In-Vivo Flax Seeds for Treatment[59] 20

2.1.2 Treatment of Cellulose Nanofibril 20

2.1.3 Treatment with Cellulose Nanocrystal 21

2.1.4 Preparation of Flax Plants for Analysis 22

2.2 Results and Discussion 25

2.2.1 Enhancement of growth via Cellulose Nanofibril 25

2.2.2 Enhancement of growth via Cellulose Nanocrystal 33

2.2.3 Experimental Process Improvement and Comparisons between CNF and CNC 44

2.2.4 Hypothesis on the Enhancement of Growth 46

2.3 Conclusion 48

Chapter 3 Modification of Mechanical Properties in Nanocellulose Treated Flax Stems and Fibers.....51

3.1 Materials and Methods..... 51

3.1.1 Preparation of Flax Stems for Mechanical Testing..... 51

3.1.2 Preparation of Flax Fibers for Mechanical Testing 52

3.1.3 Statistical Modeling[81] for Fiber Mechanical Behavior 53

3.2 Results and Discussion 55

3.2.1 Mechanical Behavior of Flax Stems 55

3.2.2 Mechanical Behavior of Flax Fibers..... 57

3.3 Conclusion 69

Chapter 4 Techno-Economic Analysis of Nanocellulose Enrichment of Flax Fibers 71

4.1 Preface..... 71

4.2 Exploratory Synthesis of Cellulose Nanoparticles 74

4.2.1 Materials and Methods[22] 75

4.2.2 Results and Discussion 76

4.3 Results and Methodology for Techno-Economic Analysis 79

Chapter 5 Pultruded Composites Using Recycled Carbon Fiber and Green Polyurethane 89

5.1 Introduction..... 89

5.2 Materials and Methods..... 94

5.2.1 Interfacial Property Analysis of BASF© Polyurethane and CrossLinks© Carbon Fiber 94

5.2.2 Interfacial Property Analysis of the Composite System..... 95

5.2.3 Pultruded Composite Creation at PulFlex, Inc. 96

5.2.4 Volume Fraction Confirmation of Pultruded Coupons..... 97

5.2.5 Mechanical Testing of Pultruded Coupons..... 98

5.3 Results and Discussion 101

5.4 Conclusion 116

5.4.1 CRediT Statement of Contribution 117

Chapter 6 Conclusion 118

Appendices 121

Bibliography 142

List of Tables

Table 1-1. Fiber types and their lignocellulosic composition. Adapted from Asim et. al.[45] 10

Table 1-2. Fiber types and their associated mechanical properties. Adapted from Asim et. al.[45] 11

Table 2-1. Cellulose functional groups and their expected peak values in FTIR and Raman spectroscopy..... 27

Table 2-2. Detailed view of saccharides present in an amount of wood pulp based cellulose nanofibril..... 28

Table 2-3. Evaluation of the germination rate for each treatment condition 37

Table 2-4. Comparisons of plant linear density across various treatment conditions. 40

Table 2-5. Area density for treated flax plants based on the area occupied by plant matter--excludes hollow space/pith area..... 42

Table 2-6. Percentage of plant matter occupied (excluded hollow space/pith) cross-section occupied by bast fibers..... 44

Table 2-7. Differences in baseline flax shoot length between CNF treated and CNC treated plants..... 45

Table 3-1. Weibull shape and scale parameters for tested fiber treatments..... 61

Table 3-2. Griffith's Parameters for flax fibers treated with nanocellulose..... 63

Table 5-1. Stress and strain equations for three and four-point bending based on ASTM D7264..... 99

Table 5-2. Volume fraction measurements for pultruded coupons..... 106

Appendix Table 1. Results from soil testing on soil obtained from field trial at Coast Fibers in Oregon..... 135

List of Figures

Figure 1-1. Process describing nanocellulose synthesis from wood pulp. Adapted from Thomas et. al.[11] 2

Figure 1-2. Nanocellulose dimensions based on source of origin. Adapted from Kumar et. al (2025).[16] 3

Figure 1-3. Secondary cell wall deposition in terminally differentiating cells. Adapted from Marinho et. al.[38] 7

Figure 1-4. Image of Flax Cross-section by Ryan R. McKenzie[11]. 8

Figure 1-5. SEM Image of a Flax Stem, captured by Louise Batta. 8

Figure 1-6. Flax stem as depicted from macro level to nanoscale. Adapted from Woigk et. al[49]. 11

Figure 1-7. Scanning Electron Microscopy image of a flax technical fiber bundle. 12

Figure 1-8. Flax technical fiber bundle and associated elementary fibers. 13

Figure 1-9. Hackle photographed at Ecole Nationale d'Ingenieurs de Tarbes. 14

Figure 1-10. Mechanism for nanoparticle uptake. Adapted from Tripathi et. al[58]. 16

Figure 2-1. Schematic depicting the addition of celluose nanofibril to flax seeds. 21

Figure 2-2. Schematic depicting the application of CNC to flax seeds. 22

Figure 2-3. Methodology for calculating the phloem area for a given flax cross-section. The lengths from the center of the stem to points A, B, a, and b are determined and the area is calculated using equation II. 24

Figure 2-4. Snap point of a flax stem, the point below which stems experience cell wall thickening. 24

Figure 2-5. Raman spectrum for cellulose nanofibril paste with 90% water 26

Figure 2-6. Structure of Cellulose with functional groups indicated. 27

Figure 2-7. Matrix Polysaccharide Analysis of an amount of cellulose nanofibril paste. 28

Figure 2-8. Flax plants grown in biochambers and treated with cellulose nanofibril..... 29

Figure 2-9. Flax plant with labelled parts for measuring..... 30

Figure 2-10. Root length for control and CNF treated flax plants..... 31

Figure 2-11. Shoot length for fibrillated nanocellulose treated flax plants. 31

Figure 2-12. Mass of CNF treated flax shoots..... 33

Figure 2-13. FTIR Spectrum of cellulose nanocrystal obtained from Nanografi (Ankara, Turkiye)..... 34

Figure 2-14 A.) SEM image of a sample of cellulose nanocrystal from Nanografi at 200 μm. B.) SEM image of a sample of cellulose nanocrystal from Nanografi captured at 20 μm.. 35

Figure 2-15. X-ray diffraction data from a sample of cellulose nanocrystal (Nanografi, Ankara, Turkiye)..... 35

Figure 2-16. Shoot height of flax plants treated with cellulose nanocrystal. All heights were normalized to the control. Different treatment conditions are grouped by color, with similar treatment conditions across differing iterations being depicted by the same color. 38

Figure 2-17. Dried weights for primary flax shoots treated with cellulose nanocrystal, normalized to the control. 39

Figure 2-18. Cross-sectional area of treated flax stems normalized to control populations..... 41

Figure 2-19. Fraction of cross-section occupied by hollow space/pith. 42

Figure 2-20. a) Phloem and b) xylem area normalized to the control population. 43

Figure 2-21. Fraction of the plant matter occupied cross-sectional area (excluding hollow space/pith) that is occupied by bast fibers. 44

Figure 2-22. Enzyme cleaving mechanism for nanocellulose enhanced upregulation of growth. 47

Figure 2-23. The enzymatic cleavage of polymeric cellulose to glucose, the monomer unit..... 48

Figure 3-1. Stem samples created for tensile testing. 51

Figure 3-2 Diagram depicting single fiber tensile testing..... 52

Figure 3-3. Flax fiber before and after single fiber tensile testing..... 53

Figure 3-4. Tensile modulus for treated flax stems. 55

Figure 3-5. Ultimate strength and tensile modulus values for CNC treated flax stems..... 56

Figure 3-6. Representative points for calculating cross-sectional area of a flax fiber. These points are taken using ImageJ imaging software and then halved to determine radius. 57

Figure 3-7. Stress-Strain Curve for Control Flax Fibers. 58

Figure 3-8. Stress-Strain Curve for Single Treatment Flax Fibers. 59

Figure 3-9. Stress-Strain Curve for Weekly Treatment Flax Fibers. 60

Figure 3-10. Weibull model analysis for all treated stem showing fracture probability versus stress. 62

Figure 3-11. Calculated regression model of strength at break for control flax fibers. 64

Figure 3-12. Regression model of Young's modulus as a function of fiber diameter in control flax plants. 65

Figure 3-13. Regression model of strength as a function of fiber diameter in single treatment flax fibers. 66

Figure 3-14. Regression model of Young's modulus as a function of fiber diameter in single treatment fibers. 67

Figure 3-15. Regression model for strength as a function of diameter in weekly treatment fibers. 68

Figure 3-16. Regression model for Young's modulus as a function of diameter in weekly treatment fibers. 69

Figure 4-1. Share of US export value as reported by the USDA. 71

Figure 4-2. Flax circular synthesis flow chart from growth to synthesis of flax-based cellulose nanocrystal. 73

Figure 4-3. Cellulose nanocrystal observed under scanning electron microscope at a.) 200 microns and b.) 20 microns. 75

Figure 4-4. Scanning electron micrographs of Softwood-derived synthesized cellulose nanocrystals. 76

Figure 4-5. Fourier Transform Infrared Spectrograph of Softwood-derived synthesize cellulose nanocrystal. 77

Figure 4-6. Scanning electron micrographs of flax-based cellulose nanocrystals. 78

Figure 4-7. Fourier Transform Infrared Spectroscopy for flax-based cellulose nanoparticles. 78

Figure 4-8. Baseline economics of a flax producing farm. 80

Figure 4-9. Modified economics of a flax producing farm treating plants with crystalline nanocellulose..... 81

Figure 4-10. Baseline economics of a flax producing farm regenerating crystalline nanocellulose, with which they treat their flax plants..... 82

Figure 4-11. Economics of cellulose nanocrystal treatment of flax by process step..... 83

Figure 4-12. Cost of flax production per step..... 85

Figure 4-13. Cost of cellulose nanocrystal modified flax production by step..... 86

Figure 5-1. Model of a standard pultrustion line for polyurethane resins. 90

Figure 5-2. Resin bath and resin injection boxes on pultrusion lines..... 90

Figure 5-3. Izod impact test experimental setup..... 100

Figure 5-4. Contact angle measurement for a droplet of glycerol on woven carbon fiber..... 101

Figure 5-5. Contact angle measurement of a drop of bio-based polyurethane on a carbon fiber tow..... 102

Figure 5-6. Stress-strain curves for single carbon fibers tested on paper frames. 103

Figure 5-7. Stress-strain curve for polyurethane dogbone samples..... 104

Figure 5-8. Scanning electron microscopy imaging for a cross-section of a 74% volume fraction composite sample..... 105

Figure 5-9. Fraying of CrossLink carbon fiber during the pultrusion process. 107

Figure 5-10. Stress-strain tensile data for the 74% volume fraction using an extensometer, and from the cross-head displacement..... 108

Figure 5-11. Tensile stress-strain curve for the 60% volume fraction using an extensometer... 108

Figure 5-12. Tensile samples following testing. Failure occurs between the fibers and matrix. 109

Figure 5-13. Stress-strain curve from flexural testing for the 74% volume fraction composite. 110

Figure 5-14. Stress-strain curve for flexural testing of the 60% volume fraction composite samples..... 111

Figure 5-15. Izod impact failure of carbon fiber composite samples: (a) 60% and (b) 74%..... 112

Figure 5-16. Izod impact failure mode counts for 60% and 74% carbon fiber samples..... 113

Figure 5-17. (a) 60% and 74% CF impact resistance, (b) 60% and 74% CF impact strength.... 114

Figure 5-18. Impact resistance ECDF for 60% and 74% CF samples. 115

Figure 5-19. Break Energy vs Percent Dissipated CDF for 60% and 74% CF samples..... 116

Appendix Figure 1. Procedural guidelines for creating CNF droplets. 123

Appendix Figure 2. CNF droplets on pre-germinated Arabidopsis plants. 124

Appendix Figure 3. CNF droplet treated Arabidopsis plants following two weeks of growth. . 125

Appendix Figure 4. Hydrogel synthesized from cellulose nanocrystals..... 126

Appendix Figure 5. FTIR spectrograph comparing a standard of cellulose nanocrystal to synthesized cellulose hydrogel. 127

Appendix Figure 6. Cross-section of a control flax stem (Stem 1). 128

Appendix Figure 7. Cross-section of a control flax stem (Stem 4). 129

Appendix Figure 8. Xylem for an enzyme-retted flax stem, untreated. (Stem 4)..... 129

Appendix Figure 9. Cross-section for a flax stem treated with one single treatment of cellulose nanocrystal. (Stem 1). 130

Appendix Figure 10. Cross-section of a flax stem treated weekly with cellulose nanocrystal. (Stem 2)..... 130

Appendix Figure 11. Cross-section of a flax stem treated once a week for 12 weeks. (Stem 5). 131

Appendix Figure 12. Technical fibers derived from flax plants treated once a week for 12 weeks. 131

Appendix Figure 13. Technical flax fiber bundle derived from flax plants treated once a week for 12 weeks. 132

Appendix Figure 14. Winter flax planted in November 2025 at Coast Fiber's farm in Oregon. 133

Appendix Figure 15. Flax photographed at 8 weeks of growth at Coast Fibers in Oregon..... 134

Appendix Figure 16. Flax plants photographed at 14 weeks of growth at Coast Fibers. Control flax plants were observed to be between 24-30 inches with treated flax plants reaching heights of between 19-29 inches. 135

Appendix Figure 17. Crushed hemp stem reinforced composites. 137

Appendix Figure 18. Crushed hemp stem composite. 137

Appendix Figure 19. Enzyme retted flax crushed flax stem composites..... 138

Appendix Figure 20. Force-displacement curve for CNC treated crushed flax stem composites..... 139

Appendix Figure 21. Process for creating pultruded plaques of glass fiber and flax fiber..... 140

Appendix Figure 22. Glass fiber-flax fiber reinforced pultruded coupons in hollow rectangle geometry. 141

List of Appendices

Appendix A: Supplemental Work.....121

A.1 Controlled Growth of Arabidopsis on CNF Modified Growth Media..... 121

A.2 Creation of Hydrogels using Cellulose Nanocrystal..... 126

A.3 Scanning Electron Microscopy Images of Flax Stems and Fibers..... 128

Appendix B: Future Work 133

B.1 Growth of CNC Treated Flax Plants on Small-Farm Scale 133

B.2 Creation of CNC Treated Flax Fiber-Epoxy Composite Materials..... 136

B.3 Hybrid Flax-Carbon Fiber Composites via Pultrusion..... 139

Abstract

The impending culmination of the UN Paris Agreement has ignited a necessity to pursue technological advances to reduce human reliance on materials that require vast amounts of energy to produce without the benefit of greenhouse gas sequestration or recyclability. In this thesis, bio-based additives for growth (as outlined in US Patent No 7935-3340-US1 (2026-435)) and bio-based composites are investigated to determine performance viability in pursuit of this goal. Cellulose nanoparticles added to flax plants enhanced masses up to 55% in treated stems, and enhanced growth of flax shoots up to 33% in select treatment conditions. These increases differed depending on the cellulose nanoparticle type, with cellulose nanocrystal treatments resulting in a larger increase in mass and shoot height with respect to control plants. Cellulose nanocrystal treatment also resulted in changes in morphology, increasing the density of flax plants as compared to the control. Treated flax plants exhibited larger tensile properties in the stem, but no significant change in properties when observing single fiber tensile data. Additionally, a slight increase was observed in the Young's modulus of fibers treated weekly with cellulose nanocrystal. Investigations in fiber reliability and dependence of fiber diameter on tensile properties were limited due to the number of available samples, a problem set to be remedied with larger samples sizes obtained from field trials.

Focusing on scaling up, a techno-economic analysis was conducted on outdoor flax with comparison studies focused on the addition of cellulose nanocrystal as a growth additive. Cellulose nanocrystal costs usurps farm costs for growing flax however, the potential to sell excess nanocellulose produced on the farm may offset costs incurred, over time, for the use of cellulose nanocrystal as an additive. This study will continue as additional treatment conditions emerge for improving baseline properties of flax fibers. Alongside this operation at scale, research was conducted into production of a fully bio-based composite using pultrusion. Pultrusion is a process of creating continuous fiber composites, and is used for structural materials. The recycled carbon fiber synthesized by CrossLink had a modulus of 289.9 ± 99.9 GPa which placed it in the low range for a recycled carbon fiber, and the BASF bio-based polyurethane modulus between 770 and 810 MPa which placed the resin in the mid-range for recycled polyurethanes. As a composite system, issues arose with fiber-matrix compatibility, and resin hygroscopicness which caused the composite to perform below theoretical expectations. The system, which was able to be successfully pultruded, provides a baseline to be built upon for the synthesis of green composites. Future work is focused on scalability and application of these green research outcomes.

Chapter 1 Introduction

In 2015, the United Nations Framework Convention on Climate Change set a goal to hold the global average temperature to less than 2 °C above the pre-industrial global average[1]. In order to do this, UN member countries agreed that they must decrease global greenhouse emissions by 43% before the year 2025[1]. Though the United States exited the Paris Agreement, as this compromise was billed, efforts are still ongoing to combat the ever-present rise in global temperatures. COP30 continues to be supported by efforts made across the globe. Renewable energy usage surpassed coal usage for the first time in 2025, and the use of solar outpaces the use of fossil fuels in the European Union[2]. While the energy sector progresses to using renewable materials, the high-performance materials sector exercises a reliance on non-recyclable materials like glass fiber. Glass fibers represent as much as 95% of fiber reinforced composite materials[3]. In wind turbine blades, for example, glass fiber reinforced composites make up 62% of the weight of the turbine, and 10-15% of the weight of material unable to be recycled[3]. More broadly, 1.567 billion pounds of glass fiber rovings were used in production each year in 2010, with 485 million pounds used in the automotive industry[4]. Advancement in the materials sector can begin with the usage of plant biomass in place of glass fiber to enhance recyclability of decommissioned composites. This can be furthered by using bio-based resin and bio-based performance fibers (such as recycled carbon fiber) in addition to natural fiber. Natural fibers, such as hemp, have been shown to store 325 kg of carbon per metric ton of plant biomass and act in carbon sequestration[5]. An essential material for carbon sequestration, and for providing mechanical support for plant based fibers, is cellulose[6].

There is a vast supply of cellulose (annual production of 180 billion tons of pulp annually[7]) that exists for usage. Cellulosic fibers have been used over time in lumber, pulp and paper, and cordage[8]. More recent advances in technology have allowed for uses in new niches including explosives[9], textiles, and even as a dietary supplement. Lignocellulosic plant material is an essential load-bearing and combustible component of the plant biomass[10]. When subjected to hydrolysis and/or shear force, elongated crystalline nanofibrils can be obtained. These nanofibrils vary in length from tens of nanometers to the low micrometer range[11]. With more intense filtration, we can get crystalline cellulose on the single-digit nanometer scale[12]. Nanocellulose is known for its small size, low density, non-toxicity, bio-affinity, and ease of degradation[12]. Advancements in nanotechnology have given way to the ability to continue to customize surface chemistry and sugar end groups in ways that can enhance other properties of nanocellulose (flame retardancy, transparency, flexibility)[13,14].

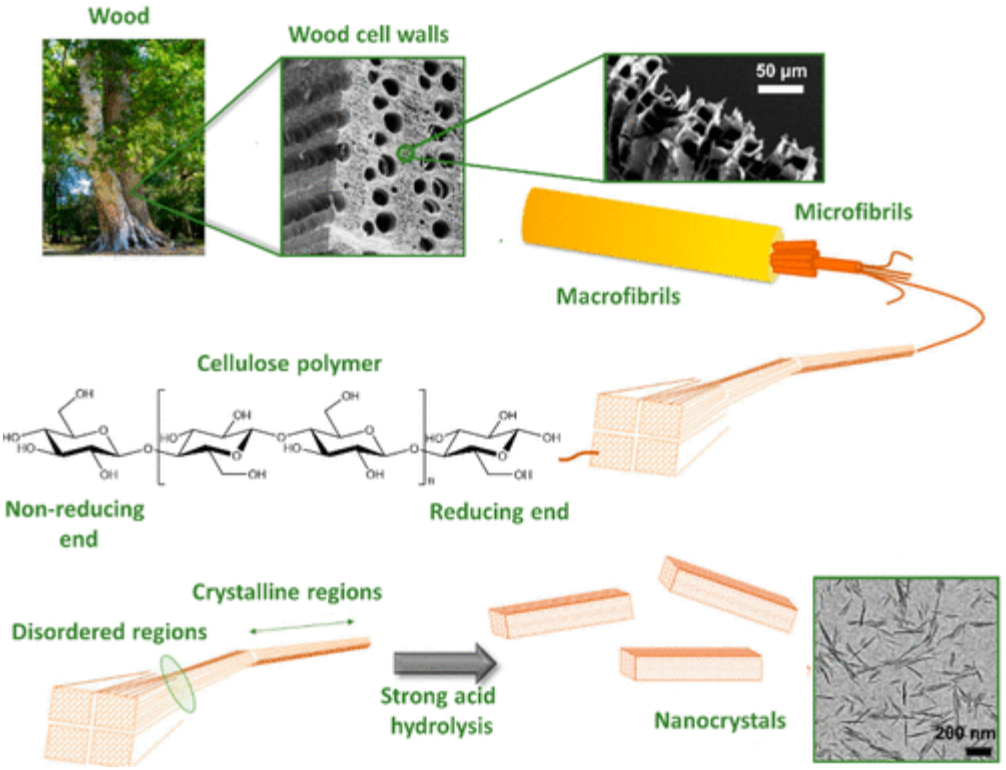


Figure 1-1. Process describing nanocellulose synthesis from wood pulp. Adapted from Thomas et. al.[11]

Nanocellulose $(C_6H_{10}O_5)_n$ is a structure composed of D-glucose monomer units linked in β(1-4) polymeric linkage by an ether bond called a glycosidic bond[15]. Water insoluble and hydrophilic, cellulosic components are biodegradable and are typically consumed by animals, plants, and micro-organisms[16]. Nanocellulose has different types from a variety of origin sources. The types can be shown below:

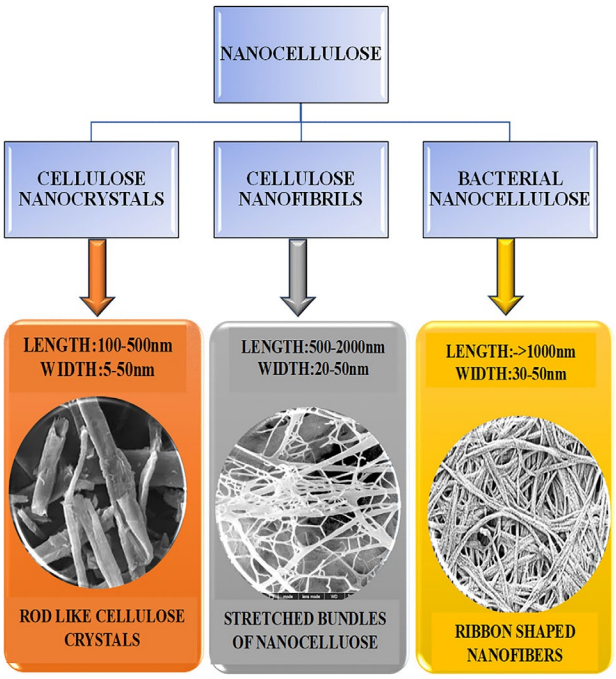


Figure 1-2. Nanocellulose dimensions based on source of origin. Adapted from Kumar et. al (2025).[16]

Bacterial nanocellulose (BNC) is often produced or derived from the biologically engineered microorganisms[15]. With synthesis pathways originally discovered in 1886, *Acetobacter xylinum*, *Agrobacterium tumefaciens*, *Salmonella enterica*, and *Escherichia coli* have all been common sources of bacterial nanocellulose[15]. BNCs have been researched for their high purity, high absorbency, and biodegradability for usages as biodegradable food packaging and even in the space of medical care as wound dressings, drug delivery, and in vitro usages.[17]

Cellulose nanocrystals and cellulose nanofibrils come from a diverse range of sources. The vast majority of plants on earth, as well as some bacteria and algae, have cellulose as a major component of their cell walls[18]. Starting material selection for recovering cellulose nanoparticles is essential for differentiating between crystalline and fibrillated cellulose nanomaterials. High cellulose content plant material, such as cotton bolls (>90% cellulose), or bast fibers (50-90% cellulose for various species) can produce high crystallinity cellulose[19]. Wood pulp, which is between 40 -50% cellulose in content, is typically the starting material of choice for the synthesis of cellulose nanofibril[8]. Pretreatment is often needed for both the color of the product and crystallinity of the nanomaterial. Pretreatment could be physical: milling, cryogrinding, and chipping reduce particle sizes to several tens to several hundreds of millimeters prior to the chemical treatment process[20]. Enzyme hydrolysis and use of ionic liquid[21], as well as pulp bleaching, are pre-treatments that can occur to remove the presence of secondary sugars such as pectin and hemicelluloses. Following pretreatment, the pulp or fibers undergo an alkali treatment[22]. This treatment further degrades the secondary sugars, including lignin, as well as cleaving bonds to reduce the size of the cellulosic polymer change to achieve fine particle sizes[23]. Acid hydrolysis is often the final step to obtaining nanocellulose from plant sources.[22] Acid hydrolysis with a strong acid is essential for full extraction of non-crystalline cellulose and non-cellulosic polysaccharides, as we as the removal of amorphous regions of cellulose to obtain purified crystalline cellulose[24]. By this point in the production step, fine particle sizes have already been obtained, and selection and synthesis of a more ordered product is the goal. Choosing the right acid, and consecutive washing steps is what allows for the proper removal of the highly amorphous region of the biopolymer.[19,25] Difference in preparation is also what drives the size differences between the fibrillated and crystalline forms of nanocellulose. Nanocellulose is derived from cellulose

microfibrils by milling can vary in width from 5 to 100 nanometers and have lengths of several microns[26]. Individual nanocrystals of nanocellulose can have a size of 3-20 nanometers[26].

The use of nanocellulose as a biopolymer has extended from biodegradable packaging to drug delivery[27]. Composite materials are another avenue for the use of nanocellulose. Because of cellulose's high ordering and strong intermolecular bonding hydrogen bonding[28]. Cellulose as a nanoparticle has seen increased research interest as a substantive material for both bio-composite and resin based composite materials as well[29]. Investigations of ideal nanocellulose sources for composite materials have leaned heavily towards wood pulp, highly crystalline sources (cotton), or to plant materials that have been seen to grow in excess– that is to say, waste plant materials (bamboo, palm).[19] The diversity of use and success of nanocellulose based composite materials can also be attributed to what makes plant fiber composites successful.

Cellulose is located in the cell wall of lignocellulosic plants[30]. The primary cell wall of plants contains hemicellulose, pectins, and proteins and is some of the first material to emerge in the plant physiognomy– primary cell wall is typically found in immature plants (seedlings or saplings)[31]. The secondary cell wall is rich in cellulose, which orders along the primary axis of plant growth[31]. Hemicellulose orders along the major axis, along with cellulose, to provide additional rigidity and stability for the plant by crosslinking with the cellulose fibrils. To finish, the middle lamella acts as the interface between cells. The middle lamella is high in pectin and provides a role as a binder between individual cell walls. The intercellular space for an individual cell is called the apoplast[32]. The apoplastic space is partially responsible for the transport of water and nutrients throughout the

cell wall matrix and apoplastic thickness varies vastly between plant species and even individual fiber samples[32].

Plant cells differ in structure from animal cells in various ways. Though both have cytoplasm, nuclei, and cell membranes, the plant cell features important structures that make up the recognizable body of the plant[18]. These cells differentiate to better serve the plant: dermal tissue, ground tissue, and vascular tissue appear as a result of this differentiation. Dermal tissue, like the epidermis in animal tissue, is the protective tissue that surrounds the stem. Ground tissue acts similarly to animal tissue in that it composes the internal organs and the body of the plant[33]. Parenchymal cells are differentiated to act as the storage site to starches and proteins but are also essential in photosynthesis and short-range transport of water and nutrients[33]. Vascular tissue, which forms the xylem and phloem (food transport from the leaves) also serves this purpose, specializing in long-range transport between plant tissues and organs[34]. The xylem is the location of water transport across the plant[35]. After water is absorbed by the root, it makes its way across the root epidermis and then into the cortex and endodermis (the inside) of the root[36]. From there, it arrives at the xylem and travels along the cell wall via the apoplastic pathway. The inside of the apoplastic pathway is lined with a hydrophobic substance that prevents water from escaping, forcing it to move across the pathway[37]. While in the xylem, water moves freely, crossing cell walls and entering into the stems and finally the leaves. The driving force behind the movement of water is a process known as cohesion-tension[37]. The cohesive properties of water as well as the pressure of the capillaries in plants drives water upward.[38]

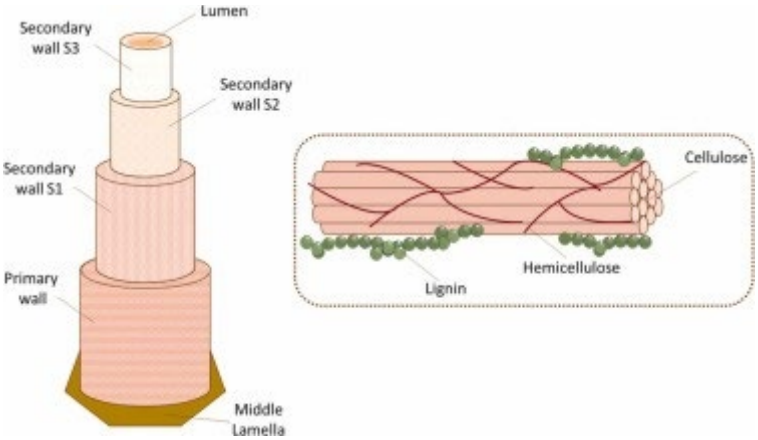


Figure 1-3. Secondary cell wall deposition in terminally differentiating cells. Adapted from Marinho et. al.[38]

Outside of their importance in water and food transport, the xylem and phloem tissues are typically embedded within sclerenchymal fiber cells, and together the reinforced primary and secondary walls in these vascular bundles and have importance with regards to their roles in providing structural support for plant fiber materials and plant-based materials. The xylem, made of lignified (but dead) ring-like cell structures provide some mechanical support to the plant stem.[39,40] Phloem, found in bast plants like flax, hemp, and jute, are unlignified, cellulose enriched, and quite long– on the order of centimeters in length.[39,40] In flax stems, the phloem fibers originate from the procambium (which in turn, originate from ground tissues derived from shoot apical meristems). The procambium could be seen in a similar vein as embryonic stem cells for the plant and allow growth of specialized plant cells[40].

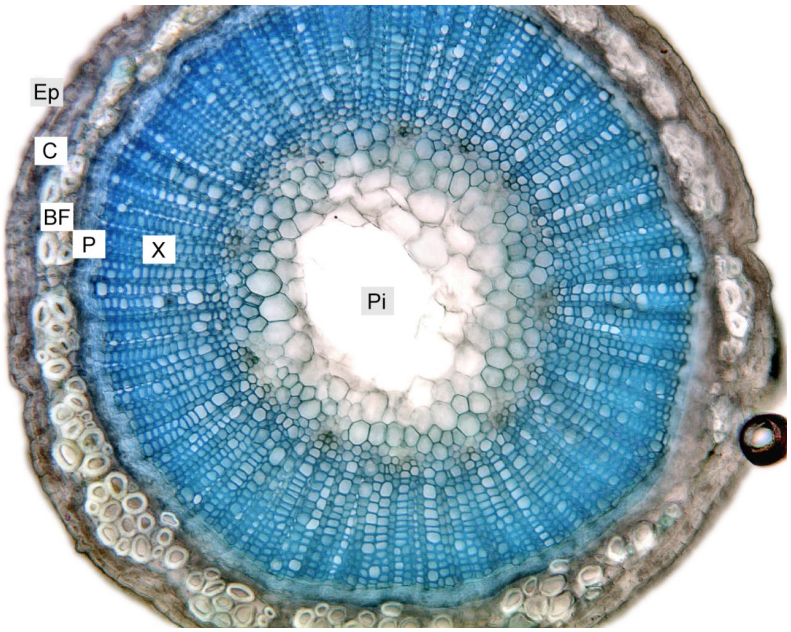


Figure 1-4. Image of Flax Cross-section by Ryan R. McKenzie[11].

This image shows the presence of xylem (X) and sclerenchyma fiber cells (BF) and bast fibers (P) located in the cross-section of a flax stem. In addition to these regions which provide much of the mechanical support of the plant, there are also pith (Pi), cortex (C), and epidermis (Ep) that exist as a result of the additional cells and plant sugars that make up the remaining body of the plant.

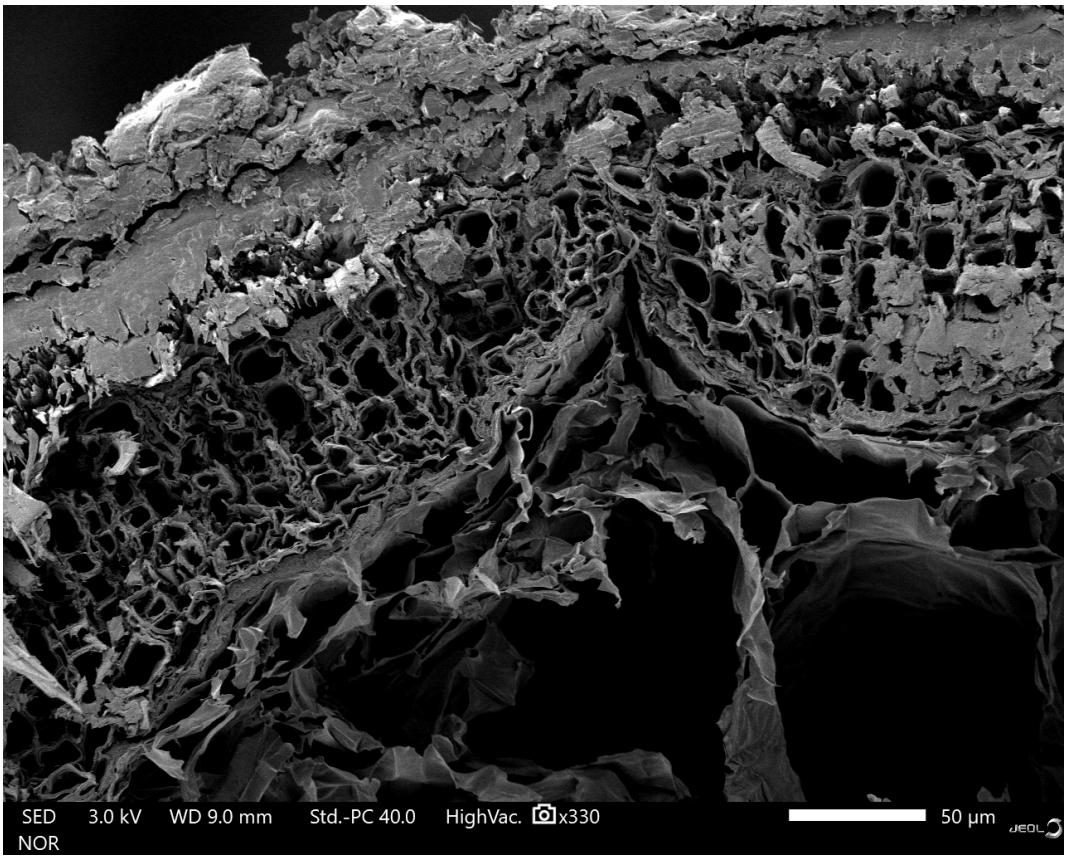


Figure 1-5. SEM Image of a Flax Stem, captured by Louise Batta.

By design, plant fibers have evolved to withstand the effects of adverse weather conditions including heat, water and humidity, wind, and other environmental conditions that pair quite well with expectations of high-performance composites[41]. Categories of plant fibers are grouped by the origin of the fibers from the plant's physiology and structure. Seed fibers are trichomes and form out of growths that are filled with cellulose.[42] Trichomes appear in the flowering stage and are fine hairs that form a protective barrier for the seeds against environmental hazards[43]. Trichomes also appear in other plants, including hemp. Coconut and cotton fibers are popular examples of seed fibers and, as previously discussed, cotton fibers' high cellulosic content makes them apt for the synthesis of nanocellulose[42]. Leaf fibers are found in vascular bundles of leaves, containing phloem and xylem tissue[44]. The increased lignin content of these fibers makes them tough and more rigid on average, with humans adapting these properties for use in materials for cordage. The fiber types, as well as their sugar content, is shown in the subsequent figure.[44] Seed fibers have a high cellulose content but lack many secondary sugars that form in other fibers, they tend to have greater elongation at break than bast fibers like flax, but have lower strain.[45] The modulus for cotton fibers also tends to be lower overall than for flax and other bast fibers[45].

Table 1-1. Fiber types and their lignocellulosic composition. Adapted from Asim et. al.[45]

Type of fiber	Cellulose (%)	Lignin (%)	Hemicellose (%)	Pectin (%)	Ash (%)	MC (%)	Wax (%)	Fibril Angle (°)
Flax	71	2.2	18.6–20.6	2.3	–	8–12	1.7	5–10
Jute	45–71.5	12–26	13.6–21	0.2	0.5–2	12.5–	13.7	0.5 8
Hemp	57–77	3.7–13	14–22.4	0.9	0.8	6.2–12	0.8	2.6.2
Ramie	68.6–91	0.6–0.7	5–16.7	1.9	–	7.5–17	0.3	7.5
Kenaf	37–49	15–21	18–24	–	2–4	–	–	2–15
Jute	41–48	21–24	18–22	–	0.8	12.5–13.7	0.5	8
Abaca	56–63	7–9	15–17	–	3	5–10	–	–
Sisal	47–78	7–11	10–24	10	0.6–1	10–22	2	10–22

Pineapple, banana, and agave leaves are used both professionally and among various cultural groups in this manner[44]. Bast fibers are true fibers, derived from fiber bundles associated with phloem elements of the vascular bundles of plant stems.[46] This is juxtaposed to wood pulp fibers which are derived from sclerenchymal fiber cells associated with secondary xylem tissue in macerated woody plant species bodies. The mechanical properties of fibers are listed below.

Table 1-2. Fiber types and their associated mechanical properties. Adapted from Asim et. al.[45]

Fiber	Density (g/cm^3)	Elongation (%)	Tensile strength (MPa)	MC (%)	Young's modulus (GPa)
Cotton	1.5–1.6	3.0–10.0	287–597	8–25	5.5–12.6
Jute	1.3–1.46	1.5–1.8	393–800	12	10–30
Flax	1.4–1.5	1.2–3.2	345–1500	7	27.6–80
Hemp	1.48	1.6	550–900	8	70
Ramie	1.5	2.0–3.8	220–938	12–17	44–128
Sisal	1.33–1.5	2.0–14	400–700	11	9.0–38.0
Coir	1.2	15.0–30.0	175–220	10	4.0–6.0
Softwood Kraft	1.5	–	1000	–	40.0

Flax (*Linum usitstissimum*) is a flowering annual plant[47]. While modern flax may be known from its seed– which has been used as a sort of superfood– flax has been cultivated for its fibers for 30,000 years[47,48]. These fibers have primarily been used for linen (as were its proto-ancestors) but have seen much review as the fiber in Fiber Reinforced Composite (FRC) materials[49].

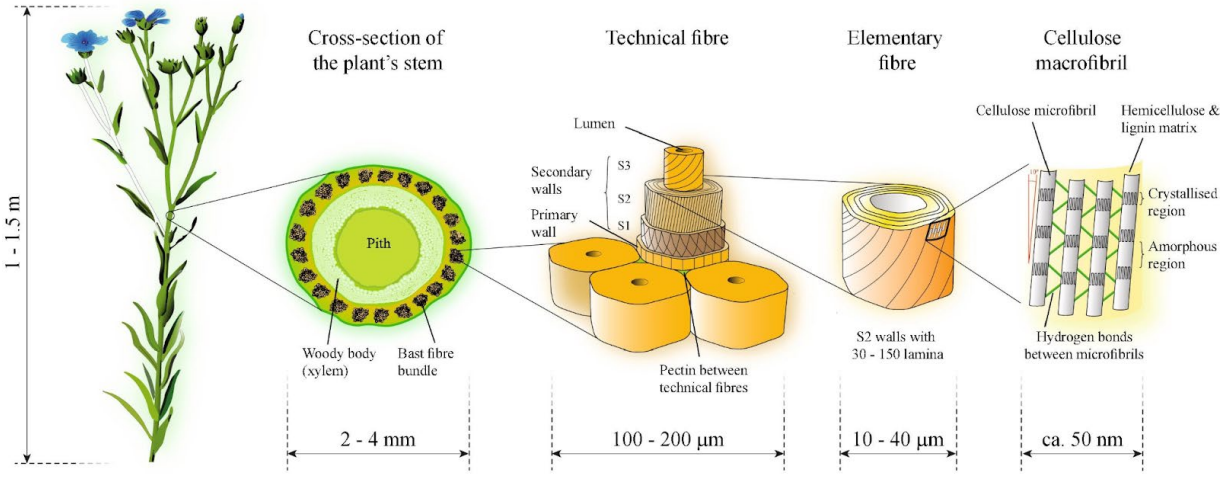


Figure 1-6. Flax stem as depicted from macro level to nanoscale. Adapted from Woigk et. al[49].

Technical fiber bundles are responsible for the majority of flax fiber products, including linen and continuous fiber composites[50]. Flax fibers are selected in FRC for their strength and modulus and low-cost[51,52]. The majority of the world's flax is produced in Europe, with France leading as a majority provider (75% in 2022)[53].

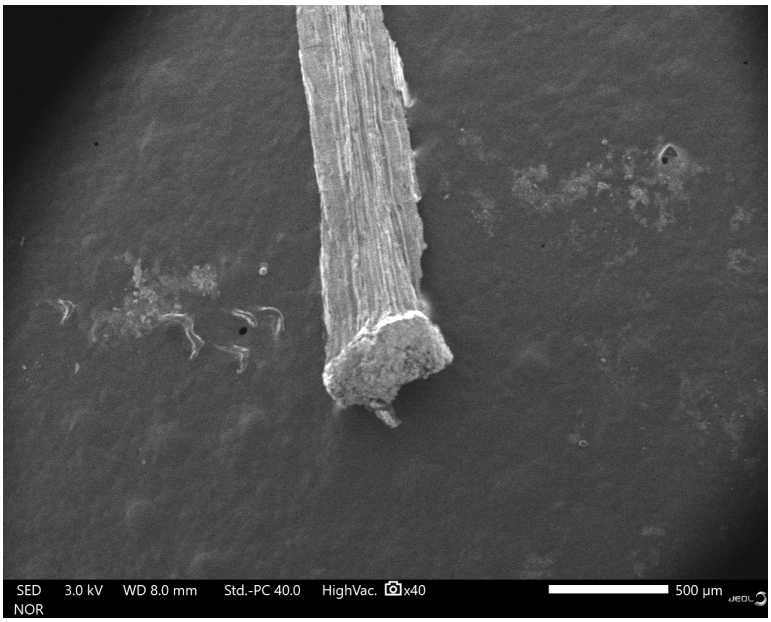


Figure 1-7. Scanning Electron Microscopy image of a flax technical fiber bundle.

Flax fiber processing involves multiple steps, with retting being the first one. Retting is the process of removing waxy structures and sugars from the stem to allow for the easy access of the bast fibers[54]. Dew retting is the industry standard, allowing for natural morning dew to bring microbes that consume lignin, pectin, and hemicelluloses from the stem[54]. Water retting controls this process by allowing closed containers, full penetration of the stem, and temperature control[55]. Enzyme retting further specializes in this process by introducing selective enzymes to consume specific sugars and also avoids some of the less advantageous parts of retting, particularly high microbial and biological waste runoff which can cause algal blooms[54]. After retting, stems are then broken (which removes the bark), scutched (which removes the remaining chives), and hackled (which removes non-continuous fibers) in order to prepare flax fibers to be used in continuous products, like linen and FRCs[56].

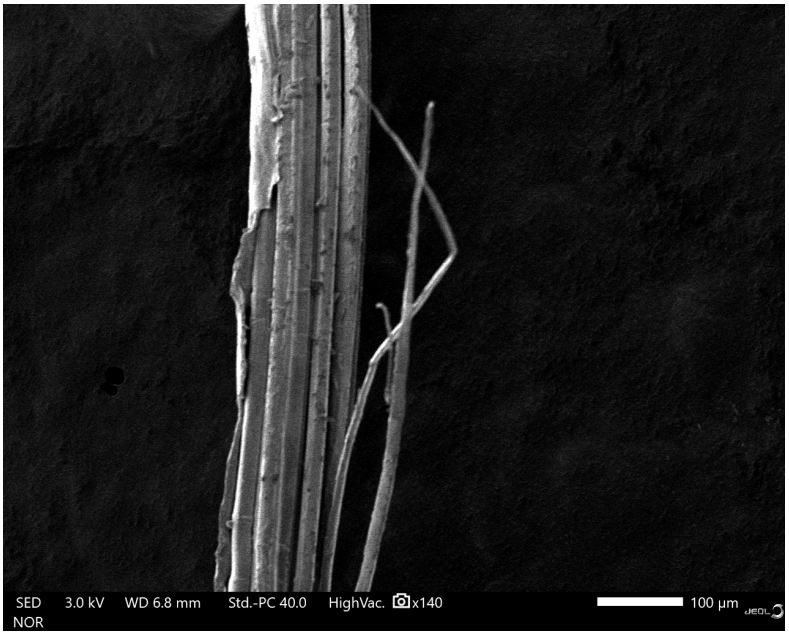


Figure 1-8. Flax technical fiber bundle and associated elementary fibers.



Figure 1-9. Hackle photographed at Ecole Nationale d'Ingenieurs de Tarbes.

Many mechanical properties of fibers are reliant on the sugar composition and location of these sugars in the plant morphology. Cellulose is a load bearing component of the cell wall and are a determinant of growth anisotropy in plant cells[18,31]. This polysaccharide plays an integral role in the mechanical properties of wood matrices and the microfibrils of celluloses exhibit high tensile strength and strong structural resistance[18]. The elastic modulus of cellulose can range from between 25 GPA and 220 GPA depending on whether intermolecular non-bonding forces such as hydrogen bonding are included in the calculations.[57] While we have examined the role of plant derived nanocelluloses for bio-composites, nanocellulose could have a role as a bio-based nanoparticle to enhance the natural properties of plants.

Nanoparticles have been a subject of interest in bioengineering, and the field of nanoparticles is responsible for increasing global investment in the trillions of dollars[58]. Nanoparticle uptake or infiltration in plant systems creates more complicated challenges due to the nature of the plants

vascular system, which is ideal for the uptake of water and charged nutrient ions such as nitrate, nitrite, phosphate, and potassium[58,59]. In addition to the nutrients derived from the soil, which plants need to survive and thrive as a part of their regulatory system, plants also need glucose. Glucose, a monosaccharide, is obtained by plants through photosynthesis[60]. Photosynthesis is the process by which plants take carbon dioxide, water, and light, and produce oxygen and sugars that become glucose[60]. During the dark reactions of photosynthesis, the RUBISCO enzyme creates 3-phosphoglycerate molecules from the reaction of ribulose-1,5-bisphosphate and carbon dioxide[60]. This reduces to glyceraldehyde-3-phosphate, with carbon molecules feeding back into the Calvin cycle to regenerate ribulose-1,5-bisphosphate[60]. One of every six glyceraldehyde-3-phosphate molecules is harvested from the Calvin cycle, two of which combine to form the dimer fructose-1,6-bisphosphate[60]. This gets converted to glucose-6-phosphate, which can then be converted to free glucose[60]. The organelles responsible for these reactions are highly specialized. Much plant focused nanotechnology is centered on selection or design of bio-compatible nanoparticles with the plant organ systems in mind[61]. Plants that are nanoparticle stressed can experience reduced photosynthesis and gene expression.[58]

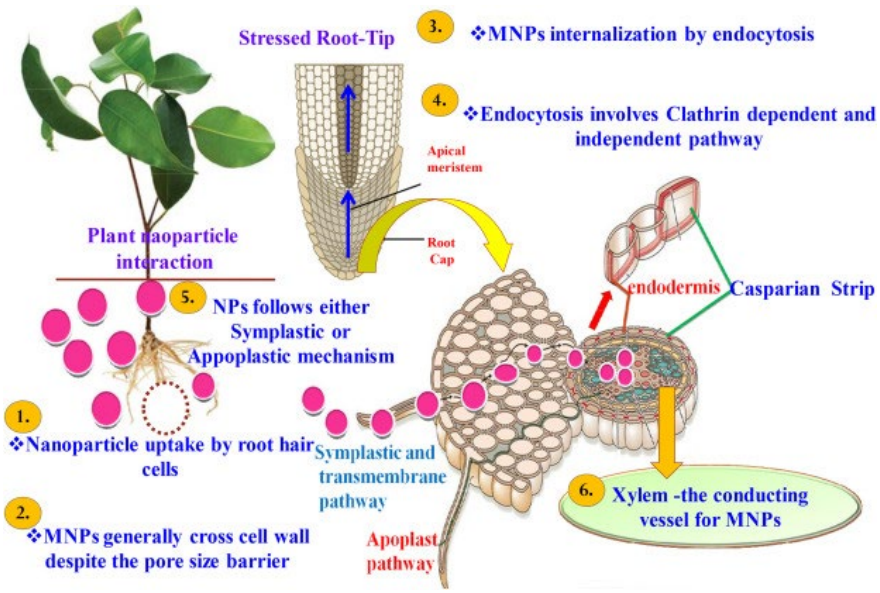


Figure 1-10. Mechanism for nanoparticle uptake. Adapted from Tripathi et. al[58].

While exact pathways for nanoparticle uptake is an ongoing field of research, several mechanisms have been proposed[62]. Uptake following the symplastic mechanism would suggest that the intercellular machinery of living cells is directly interacting with nanoparticulates located within the cellular cytoplasm. Movement of nanoparticles through the apoplastic mechanism would mean interactions primarily with extracellular matrix of the plant, such as the plant cell wall. In both cases, nanoparticle size would also function as a selection condition as the selectively permeable plant cell wall features pore sizes of around 3-8 nm. An ideal candidate for a nanoparticle with possibility to provide mechanical property enhancement in plants would have to share in favorable qualities (high strength and modulus), be biocompatible and unlikely to induce nanoparticle stress response, and to be small in size in order to pass through the plant cell wall either by the symplastic or apoplastic pathways. Nanocellulose exhibits the desired mechanical properties[63], is inherently biocompatible[11], but the current research regarding nanocellulose in plant systems is emerging.

Nanocellulose has been investigated in different plant systems. As a foliar fertilizer, nanocellulose has been shown as a potential additive to enhance the yield of blueberry plants[64]. Continuing in blueberry models, there has been interest in the use of nanocellulose as a topical coating for protection against frost[64]. One of the more interesting, and potentially roundabout, applications of nanocellulose is tied to elephant excrement[65]. Elephant excrement has been used as a fertilizer in communities in Africa and Asia[66]. Even further, elephant excrement has commonly been believed in certain communities to enhance the growth and flowering of plants, due to high phosphorous content [66]. In elephant excrement studied in Malawi, elephant dung had the highest Carbon:Nitrogen ratio of all tested fertilizers, and had a higher overall carbon content than standard fertilizer[67]. From elephant excrement, cellulose nanofibrils can also be recovered following an alkaline treatment at 80 °C. Elephants as a herbivorous species have enzymes that allow them to break down cellulose stored in branches and plants[65]. Understanding the mechanisms in the elephant gut biome could help researchers further understand nanocellulose and its role in plants.

Li, Biraku et. al conducted early studies on the addition of nanocellulose to flax plants for the enhancement of the plant mechanical properties[59]. Their study featured flax plants grown in controlled growth conditions culled and transferred to vials with water and nanocellulose. The research was to understand root propagation in these plants[59]. The researchers found that nanocellulose treated water allowed for greater propagation of roots and enhanced mechanical properties of flax stems[59]. Due to the variability in the properties of flax fibers, overall enhancement of the fiber would improve the quality of flax fiber reinforced composite (FFRC) materials[68]. The work presented in this thesis builds off of the foundation set by the aforementioned researchers, and expands it for better understanding the behavior of flax plants as a result of

nanocellulose treatment at germination, how these changes affect flax fibers extracted from treated plants, and whether or not this treatment is commercially viable for farms and communities that grow flax fibers.

Previous work conducted in this research group has focused on the addition of nanoparticles at or beyond 45 days of growth. Langhorst et. al incorporated titanium dioxide nanoparticles into fully grown flax fibers using supercritical CO_2[69]. There is a large gap, both in the literature and based on previous research conducted in the research group, on the addition of cellulose nanoparticles into soil for incorporation into the plant biome and modification of fiber properties. Subsequent chapters in this thesis will address these fixtures.

1.1 Dissertation Outline

This dissertation focuses on the research and creation for bio-based composites. In Chapter 2, we investigate the effect of cellulose nanoparticles on flax plant growth characteristics when these nanoparticles were provided to plants within the soil matrix Flax plants were grown in growth chambers with short-day (12 hours of light/dark) conditions and then harvested to observe their baseline properties, such as height, mass, and internal morphology. In Chapter 3, the harvested flax plants underwent fiber extraction and their mechanical properties were tested. In addition to these tests, Weibull probability function and a Griffith model were applied to the dataset to understand the reliability of data obtained from mechanical testing. This, paired with tensile testing performed on the flax stems, were used to determine if application of cellulose nanoparticles yield improvements in flax fiber performance. Chapter 4 evaluates to the necessity to market innovations

in the creation of natural fiber composites that will likely be necessary for the integration of these "natural fibers" into industrial processes. A techno-economic analysis was conducted to relay the cost of growing nanoparticle enhanced flax, and also introduce a circular economic model in which flax farms generate cellulose nanoparticles from their flax waste. Finally, we end with an application of bio-based composites using existing techniques. Chapter 1 presents research done in collaboration with doctoral students Steven Mamolo, Jacob Harris, and Luohaoran Wang, and master's student Chiamaka Odenigbo. We switch from bio-derived flax to pultrusion of a bio-based carbon fiber and polyurethane resin, which are used to create composites. Chapter 6Appendix A:can be used to supplement main chapters with work done to better understand mechanistic problems, or to further innovation done in individual chapters. Appendix A includes experiments related to nanocellulose enhanced in-vitro growth in alternate plant models, creation of cellulose nanocrystal based hydrogels to improve packaging and dosage of particles, and scanning electron microscopy images for better understanding flax plant morphology.

Chapter 2 Modification and Enhancement of Growth of Flax Plants via Nanocellulose

2.1 Materials and Methods

2.1.1 Preparation of In-Vivo Flax Seeds for Treatment[59]

Flax seeds *(Linum usitatissimum* L., Agetha variety) sourced from Coast Fibers (formerly FibreEvolution) in Willameter Valley, Oregon were surface sterilized. Seeds were immersed in 70% ethanol, followed by 20% bleach (sodium hypochlorite) and Tween-20. The supernatant was purged and seeds re-submerged in autoclaved, deionized multiple times to ensure all remaining microbes, bleach, and detergent are washed and discarded from the seeds. Immediately following sterilization, seeds were sown in 2" gardening trays filled with soft, nutrient soil (Sun Gro Horticulture, Agawam, MA, USA). One seed was sown per tray, with soil being saturated by a 1:4 ratio of NPK fertilizer water and well water.

2.1.2 Treatment of Cellulose Nanofibril

Cellulose nanofibril was obtained from a researcher affiliated with Sappi (Turkiye). Approximately 0.23g of cellulose nanofibril paste were weighed and separated, then transported to the growth facility[70]. The treatment condition was a selected to ensure sufficient surface carea for contact with the seed. Flax seeds were planted in nutrient rich peat media and watered until saturation with a 25% by volume concentration of nutrient water in tap water. Following planting, the pre-weighed CNF was placed in a divot of soil with the seed and then fully covered.

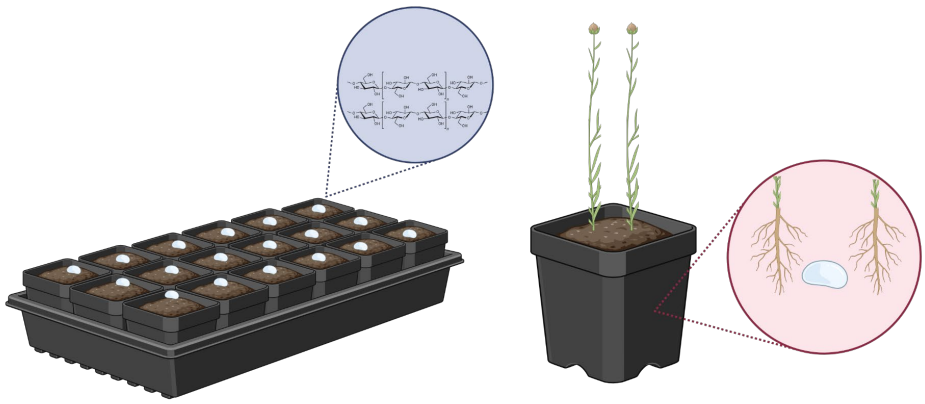


Figure 2-1. Schematic depicting the addition of celluose nanofibril to flax seeds.

Cellulose nanofibril was characterized using a JASCO Fourier Transform Infrared Spectrometer (Oklahoma City, OKC, USA), a Raman spectrophotometer with Renishaw inVia microscope and RenCam CCD Detector at 532 nm, and Matrix Polysaccharide Analysis conducted at Michigan State University. Flax seeds were cultivated for 12 weeks in growth chambers (Flex FXC-9, Biochamber, Winnipeg, Canada) controlled at 20 °C. The chamber was calibrated to short day conditions, with plants experiencing 16-hour light periods followed by 8-hours of dark. Following the first week of growth, plants were treated solely with water and their respective experimental dose of cellulose nanofibril; no additional fertilizer was delivered to the Agetha flax.

2.1.3 Treatment with Cellulose Nanocrystal

Two suspensions of cellulose nanocrystal (CNC) in well water were prepared. Laboratory grade cellulose nanocrystal (Nanografi, Ankara, Turkiye) was placed in 50 mL of water in 1% and 2.5% w/v concentrations then sonicated until fully suspended. 1 mL of each suspension was transferred via micropipette on top of the sterilized flax seed. The high weight percent concentration, at 1 mL delivered, roughly matches the expected nanocellulose mass delivered in Chapter 2.1.2. Varying treatment conditions were explored: seeds treated only once at germination and seeds treated once

weekly for 8 weeks. These treatment conditions were replicated at each of the experimental CNC concentrations. Control treatments were also conducted, with no cellulose nanocrystal being added in any amount for the duration of the experiment. An additional treatment condition was conducted at 2.5 w/v% concentration, with the final treatment group undergoing CNC addition weekly for the entirety of the 12 week growth period. Cellulose nanocrystal was characterized using a JASCO Fourier Transform Infrared Spectrometer (Oklahoma City, OKC, USA).

Flax seeds were cultivated for 12 weeks in growth chambers (Flex FXC-9, Biochamber, Winnipeg, Canada) controlled at 20 °C in the same peat media as previously discussed. The chamber was calibrated to short day conditions, with plants experiencing 16-hour light periods followed by 8-hours of dark. Following the first week of growth, plants were treated solely with water and their respective experimental dose of cellulose nanocrystal; no additional fertilizer was delivered to the Agetha flax.

2.1.4 Preparation of Flax Plants for Analysis

After the twelve-week growth period, flax plants were removed from their growth chambers and processed. Height and weight measurements were obtained by primary data for each plant.

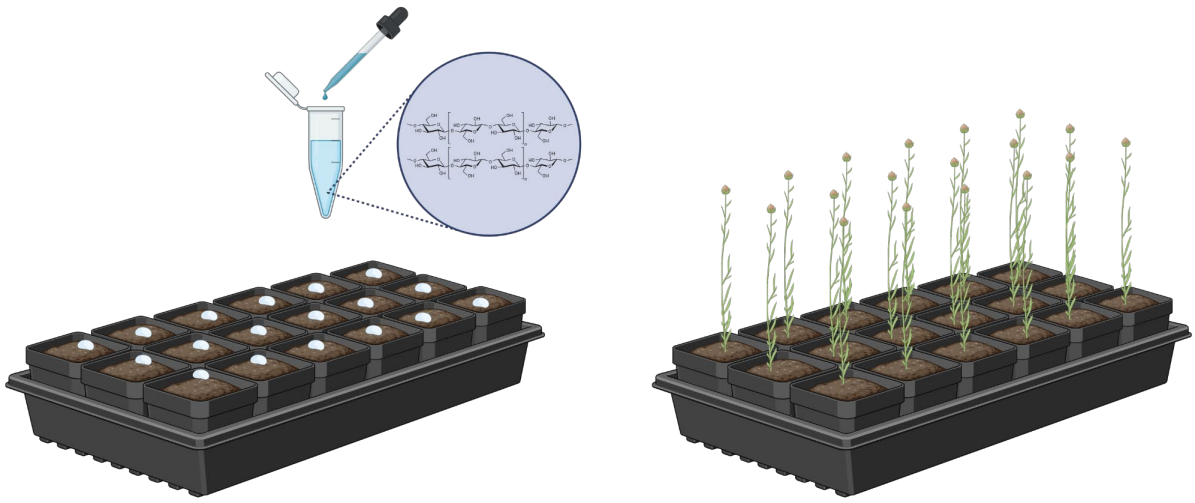


Figure 2-2. Schematic depicting the application of CNC to flax seeds.

Stems were separated from their roots by shearing at the base of the root nodule. The root was weighed and then dried. Post fresh processing, flax stems were then air dried over a period of weeks or oven dried at 80 °C until all water had evaporated from the stem. Stems were then re-weighed; cross-sections of the stems were obtained using a hot wire cutter (THERMOCUT 115/E, Proxxon Inc, Hickory, NC) and sanded with grit paper, making sure to use pressurized air to remove dust from the surface of the stem. Using an Olympus GX51 Inverted microscope, information on the morphology of the cross-section of each flax stem was obtained. This includes information regarding the size of the outer bark, the size and location of phloem fibers, the xylem area of each treated plant, and the size of the hollow space/pith area. Images taken using the inverted microscope were then analyzed using ImageJ software to calculate cross-sectional areas for each stem, as well as the cross-sectional area of the aforementioned plant features. The formulas for calculating the cross-sectional area were as follows:

$$Area_{ellipse} = \pi AB \qquad \text{(I)}$$

$$Area_{ellipse,ring} = \pi(AB - ab) \qquad \text{(II)}$$

where ab is the area of the inner ring, and AB the area of the outer ring. Equation (I)$\mathrm{Area}_{\mathrm{ellipse}} = \pi AB$ (I) was used to calculate the total cross-sectional area, and Equation (II) was used to calculate the areas of the xylem and phloem, which exists as rings inside the larger structure of the stem.

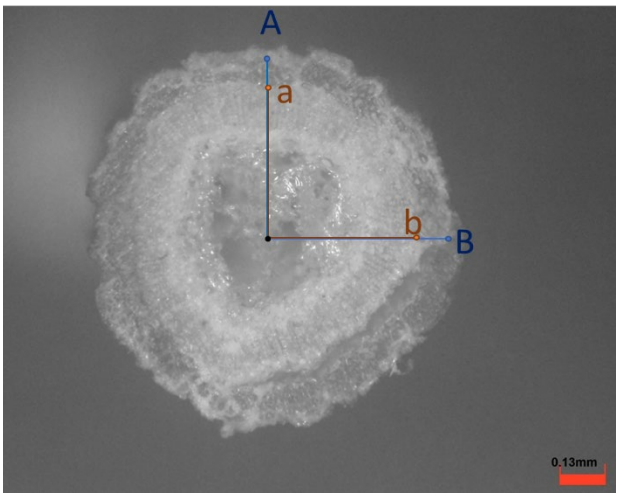


Figure 2-3. Methodology for calculating the phloem area for a given flax cross-section. The lengths from the center of the stem to points A, B, a, and b are determined and the area is calculated using equation II.

Sections taken from below the snap point of the treated flax stems were flattened and aligned to prepare for X-Ray Diffraction. A Rigaku SmartLab X-Ray Diffractometer (Tokyo, Japan) with Cu-KR radiation (k=0.154 nm, 40 kV, 44 mA) was used to obtain information about the presence and crystallinity of crystalline cellulose located in the walls of the flax specimen. Diffraction data was collected from 8° to 40° at a scanning rate of 2°/min[69]. Crystallinity was calculated as described in **Equation 3** by Segal et. al[71] and is shown below:

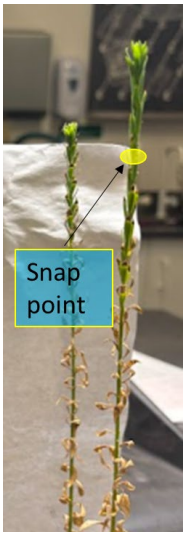


Figure 2-4. Snap point of a flax stem, the point below which stems experience cell wall thickening.

$$\chi = \frac{I_{200} - I_a}{I_{200}} \qquad \text{(III)}$$

This equation refers to the crystalline cellulose (2 0 0) peak intensity at 22° juxtaposed with the intensity of the amorphous cellulose. This value is obtained from the minimum at approximately 18.6°. All values are reported in 2θ.

Scanning electron microscopy (SEM) images were collected on a JEOL IT500 (Peabody, MA) Scanning Electron Microscope at 3 kV. Images were collected

from below the snap point to investigate stem diameter, fiber location, and density inside the stem. Fiber quality was also determined with extracted fibers observed from SEM imaging. Fibers were extracted in accordance with the protocol set by Singhal et al (2023)[54].

2.2 Results and Discussion

2.2.1 Enhancement of growth via Cellulose Nanofibril

Prior to use of cellulose nanofibril for experimentation, structure of cellulose nanofibril was confirmed via Fourier Transform Infrared Spectroscopy, Raman Spectroscopy, and Matrix Polysaccharide Analysis. The results of the Fourier Transform Infrared Spectroscopy and Raman Spectroscopy were reported extensively in X. Biraku's thesis titled 'Investigation of Nanoparticles Incorporation During Plant Growth to Improve Natural Fiber Properties'[70], but are summarized here.

Fourier Transform Infrared Spectroscopy measures vibrational modes within a molecule that are unique to molecules and molecular bonding interactions. The peak at 3200 cm^{-1} corresponds to terminal -O-H bonds present in the structure in nanocellulose. The mid-1000s peaks correspond to alkane interactions that make up the glycosidic bonds in the sugar. Peaks near 1000 cm^{-1} represent -C-O-C ether groups and additional stretching modes for -O-H groups. There are additional alkane peaks in the 'fingerprint' region, representing vibrations that would be too small to definitively detect using our FTIR device. The intensity of the peaks also corresponds to the presence of these molecules in the structure. FTIR spectra confirm the presence of molecular structures found in nanocellulose fibril. This also matched literature spectra[72].

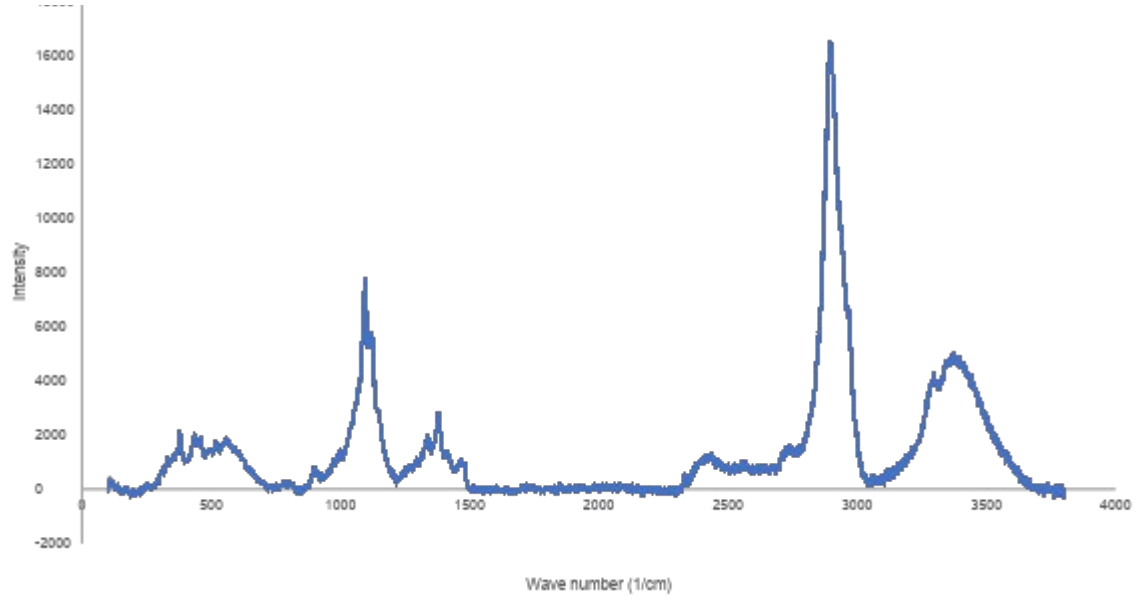


Figure 2-5. Raman spectrum for cellulose nanofibril paste with 90% water.

Raman spectroscopy detects the polarizability of molecular bonding interactions as a method for identifying the structure of the compound. Raman spectroscopy of auto-fluorescent compounds requires the use of lasers that do not detect in the fluorescent region and, as such, a 532 nm detector was used. Comparisons to literature spectra[73] show the presence of a cellulose -C-H peak at 2896 cm^{-1}, similar to the reported value of 2897 cm^{-1}. Peaks at 1381 cm^{-1}, 1093 cm^{-1}, and 382 cm^{-1} correspond to reported cellulose peaks for polarized alcohols, asymmetric vibrational mode in glycosidic -C-O-C bond (coupled with the symmetric vibration peak at 1124 cm^{-1}), and the cyclohexane vibrational mode is reported as well. The Raman and IR active functional groups are shown in the subsequent figure.

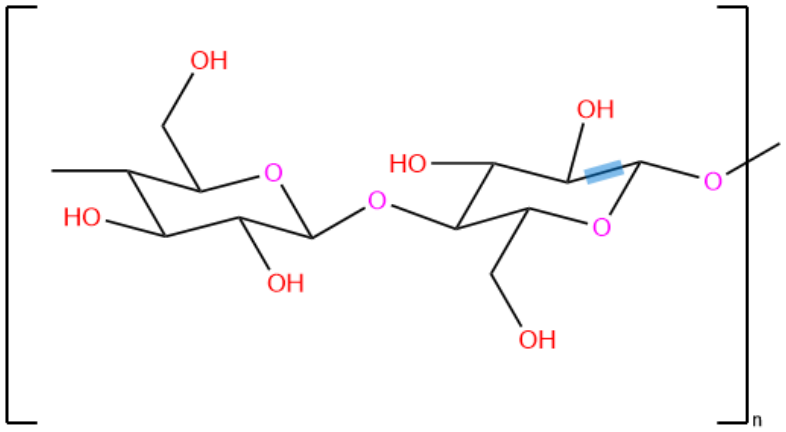


Figure 2-6. Structure of Cellulose with functional groups indicated.

Table 2-1. Cellulose functional groups and their expected peak values in FTIR and Raman spectroscopy.

Bonding type	**FTIR Wavenumber**	**Raman Wavenumber**
Terminal alcohol	3200 cm^{-1}	1381 cm^{-1}
Glycosidic ether	1000 cm^{-1}	1093 cm^{-1}
Cyclohexane vibration	fingerprint	382 cm^{-1}
Alkane (CH-CH)/Cellulosic peaks	mid-1000s	2896 cm^{-}

Matrix polysaccharide analysis is the process by which sugars in an amount of material are analyzed to determine the overall make-up of the polysaccharides in a body of plant-based material. Not only are we able to determine the amount of cellulose present in a mass of cellulose nanofibril, we are also able to determine the crystallinity of that population. This becomes

exceptionally important when determining the completeness of the cellulose nanoparticle extraction process from non-commercial sources. The results of this analysis are shown in consecutive tables and figures.

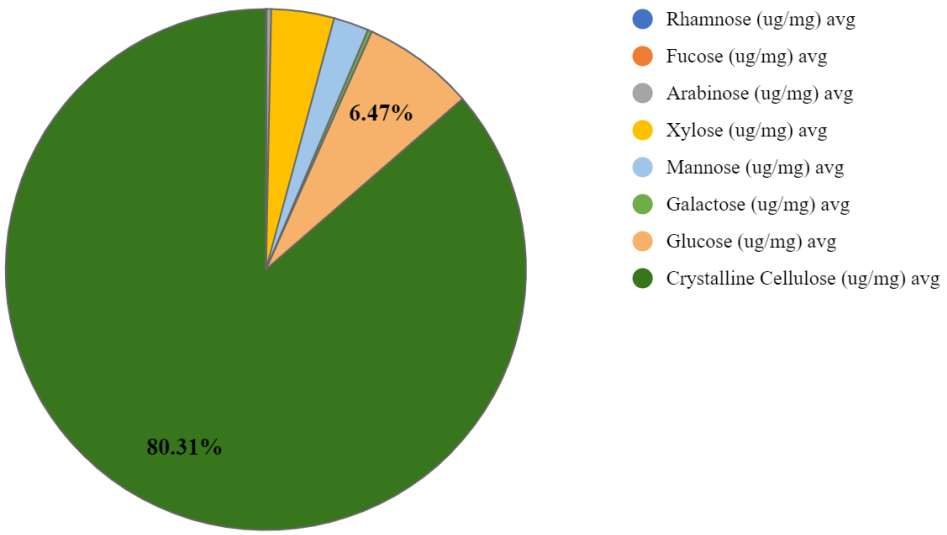


Figure 2-7. Matrix Polysaccharide Analysis of an amount of cellulose nanofibril paste.

Table 2-2. Detailed view of saccharides present in an amount of wood pulp based cellulose nanofibril.

	Rhamnose	Fucose	Arabinose	Xylose	Mannose	Galactose	Glucose	Crystalline Cellulose	Total
Average (% weight of AIR):	0.03%	0.01%	0.26%	3.63%	2.03%	0.24%	6.47%	80.31%	92.98%
Standard Deviation	0.001%	0.000%	0.002%	0.301%	0.120%	0.010%	0.367%	3.089%	

Raman spectroscopy and FTIR spectroscopy confirm a likelihood of the substance of choice being a saccharide. Confirmation with Matrix Polysaccharide Analysis is necessary when the source of the polymer is unknown, particularly to ensure that there is not an overabundant presence of lignin in the sample. In lieu of X-Ray Diffraction, or 2D Nuclear Magnetic Resonance, the reported crystalline cellulose value from the analysis can be used to confirm the crystallinity of the sample.

That value, plus the amount of glucose, confirms a cellulose nanofibril paste that is at least 86% cellulose by weight.

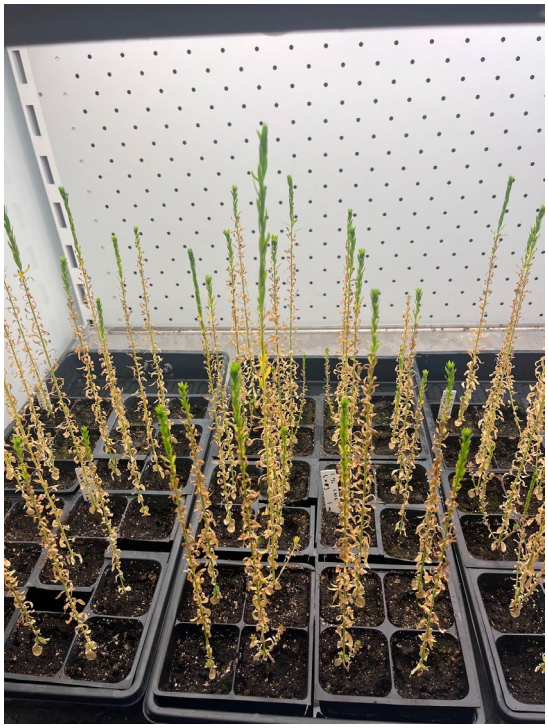


Figure 2-8. Flax plants grown in biochambers and treated with cellulose nanofibril.

Flax plants grown with cellulose nanofibril were separated from their roots, with secondary stems removed. The subsequent roots and shoots were weighed and their weights obtained. A visual representation of a flax plant and the calculable metrics from the exterior of the flax plant are shown in **Figure 2-9.**

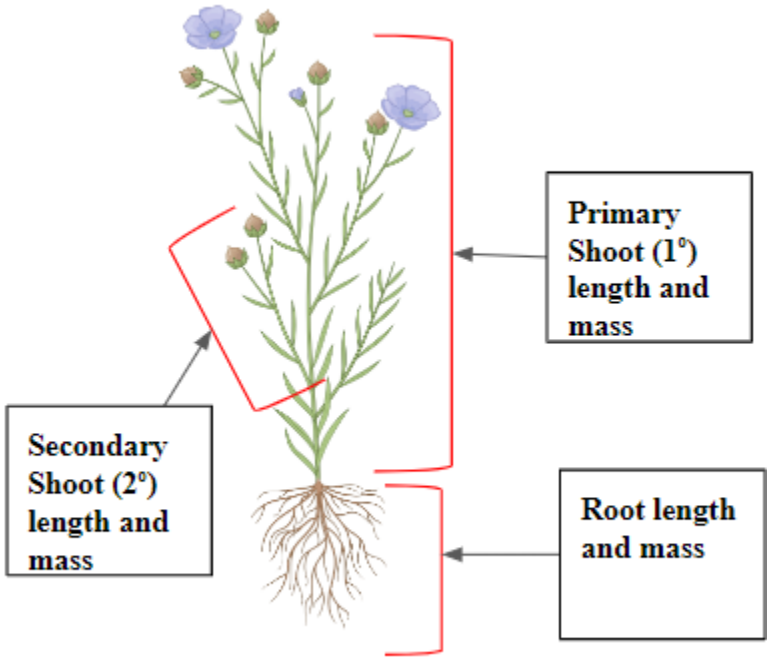


Figure 2-9. Flax plant with labelled parts for measuring.

Flax plants treated with nanocellulose exhibited no substantial increase in the length of the root system (from root node to longest root tip). With an average root length of 22.6 cm, the multiweek treatment group may exhibit a moderately significant decrease in the mean root length as compared to the control population (26.5 cm). This is reported in the subsequent **Figure 2-10.**

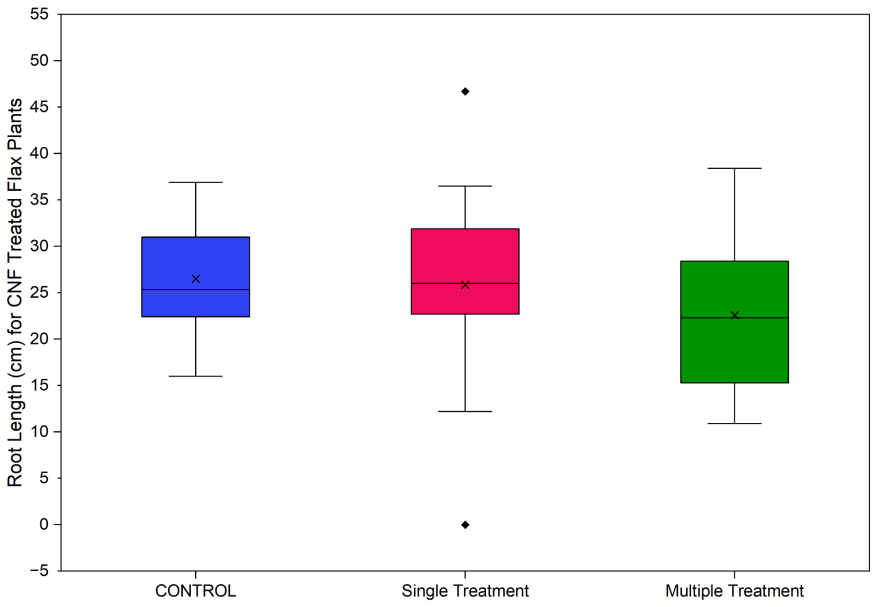


Figure 2-10. Root length for control and CNF treated flax plants.

Shoot length of flax plants were also investigated. After separating the plants from their roots at the root node, a ruler was used to measure the length of the primary stem from root to tip. The secondary shoot, also separated at the base of its nodule, was measured from base to tip.

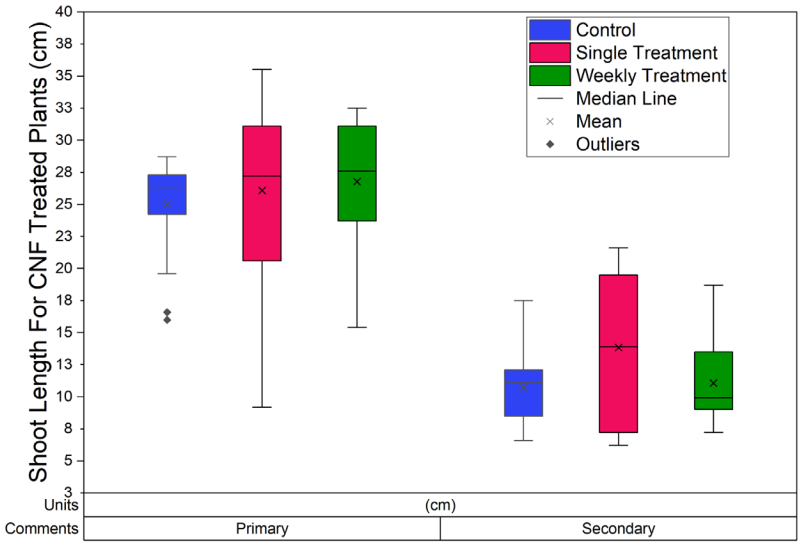


Figure 2-11. Shoot length for fibrillated nanocellulose treated flax plants.

Plants treated with cellulose nanofibril exhibit shoot lengths that are, on average, 1-1.8cm longer than the control when considering the length of the primary stem. In the case of secondary stems—branches, in essence—single treatment stems were 3 cm longer and weekly treatment stems were approximately the same length as the control stems. Variations in length were not *statistically significant* at the 95% Confidence Interval, with single treatment stems only exhibiting a moderate increase in the length of their secondary stems when compared to the control. Variability in the data, as depicted by a large standard deviation, affects the confidence in differences between two data sets. By using a T-Test, we can assign a probability value (p-value) that the means of any given data sets will be different from each other. The size of this probability value can be used to quantify the significance in these differences, ranging from $p>0.05$ (no significance) to $p<0.05$ (moderate [$0.05>p>0.02$], significant [$0.02>p>0.002$], and very significant [$0.002>p$]). The equation to determine statistical significance, the T-Test, is shown in the following equation:

$$T = (\overline{x_1} - \overline{x_2})\left(\frac{\sigma_1^2}{n_1} + \frac{\sigma_2^2}{n_2}\right)^{-\frac{1}{2}} \qquad \text{(IV)}$$

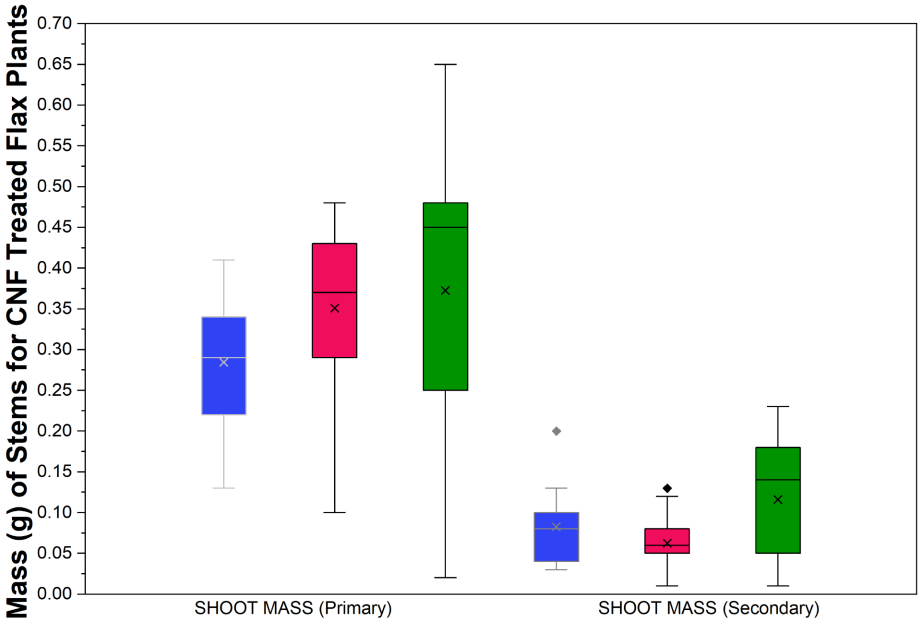


Figure 2-12. Mass of CNF treated flax shoots.

Treated plants exhibited significant differences in plant mass when compared to control flax plants grown under similar conditions. The fresh weight of these flax plants is reported for this study. Single treatment plants exhibited masses, on average, that were 0.09 g larger than control flax plants in primary shoots. Secondary shoots, which are much smaller in size in general, were 0.036 grams larger in the single treatment group than the control. Primary shoots were significant at the 95% CI, however variation in standard deviation was large. In the case of the multiple treatment condition, plants were 0.07 grams larger than the control (lighter than the single treatment group by 0.02 grams on average) and secondary stems were reported at an average of 0.06 grams. The control stem values were significant at the 95% confidence interval.

2.2.2 Enhancement of growth via Cellulose Nanocrystal

Prior to treatment, cellulose nanocrystal was characterized to confirm structure and crystallinity. Fourier Transform Infrared Spectroscopy data is shown below in **Figure 2-13.**

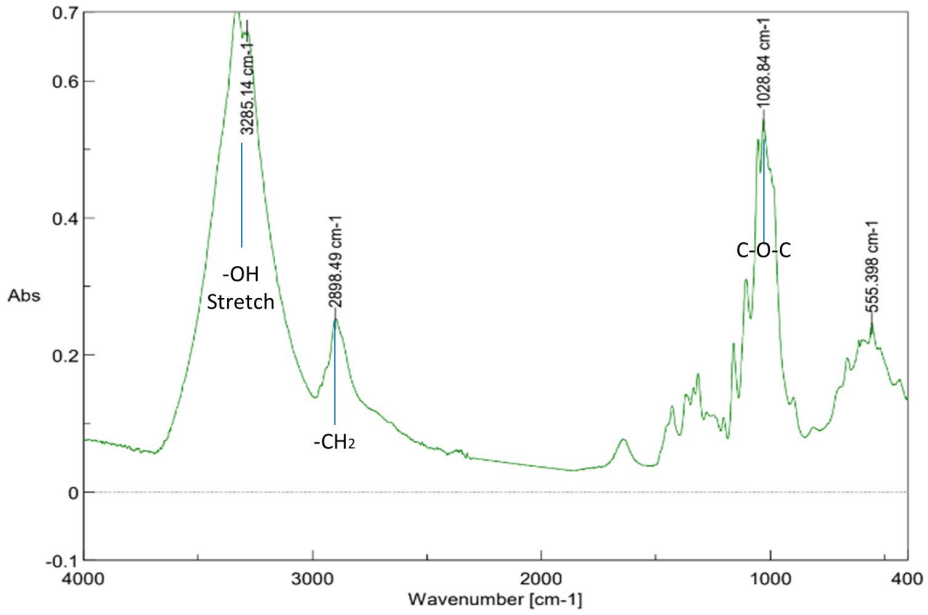


Figure 2-13. FTIR Spectrum of cellulose nanocrystal obtained from Nanografi (Ankara, Turkiye).

FTIR spectrum confirms the presence of characteristics peaks associated with crystalline nanocellulose[72]. The large peak at 3285.14 cm^{-1} corresponds to the -OH stretching peaks found at the terminus of cellulose chains. An O-H bending peak is not prominent, and instead we find a CH_2 peak alongside the O-H stretch at 2898.49 cm^{-1} and a C-O-C glycosidic linkage peak at 1028.84 cm^{-1}. Despite synthesis of the cellulose nanocrystals via acid hydrolysis using sulfuric acid, there is nothing in the FTIR spectra to suggest a strong indication that cellulose sulfate was synthesized in the process, as characteristic peaks for this product are largely missing.[74]

Scanning electron microscopy confirmed the presence of single micron crystal clusters, indicating that single crystals were in the nanometer range for samples of cellulose nanocrystals observed. These images are shown in **Figure 2-14**.

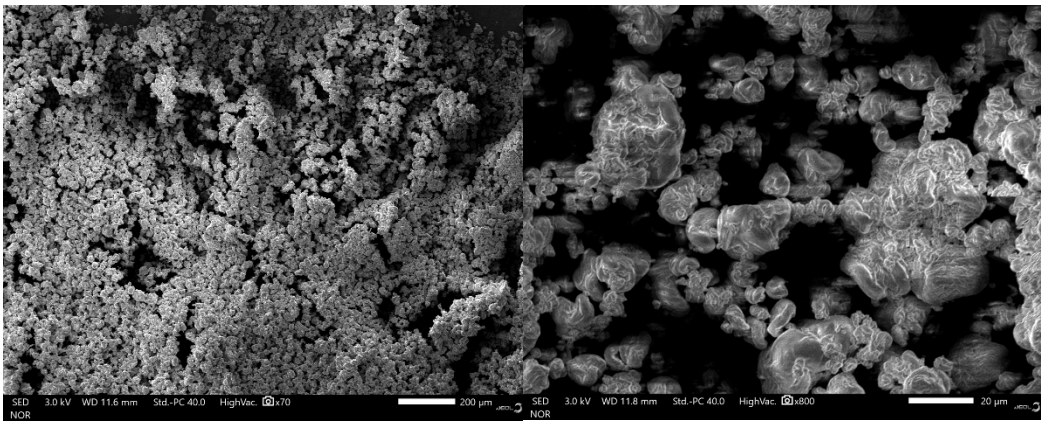


Figure 2-14 A.) SEM image of a sample of cellulose nanocrystal from Nanografi at 200 µm. B.) SEM image of a sample of cellulose nanocrystal from Nanografi captured at 20 µm..

X-ray diffraction was used to confirm the crystallinity index for the cellulose nanocrystal. This data is shown in **Figure 2-15.**

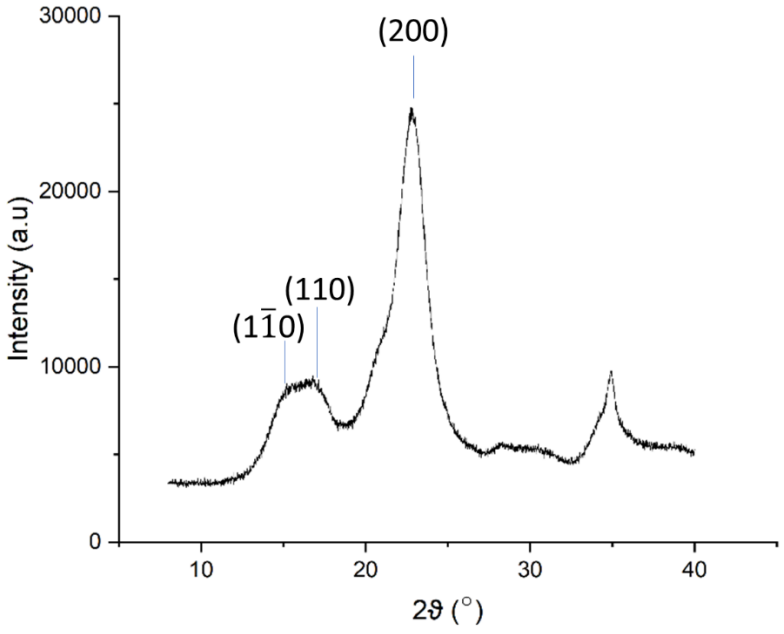


Figure 2-15. X-ray diffraction data from a sample of cellulose nanocrystal (Nanografi, Ankara, Turkiye).

X-ray diffraction confirmed a crystallinity index of 74%, which is well within the range of synthesized cellulose nanocrystal sourced from wood pulp, which extends from the mid-60% to as high as 90%.[75]

Following the three-month growth period, mass and height data were collected from each treated group of flax specimens. The control group features no additional treatment other than what is necessary to grow the flax in controlled growth chambers. Two iterations of controls were conducted to account for two different seed lines that were used over the course of the experiment. In the case of the 1 w/v% treatment condition, only one iteration was investigated, with no additional experimentation being conducted at that weight percentage for an additional seed line. Octuple feeding refers to the number of total treatments (eight) over the course of the first eight weeks of growth, with the dodecyl treatment referring to twelve total treatments over the twelve weeks of growth. All treated plants were treated at least on one occasion—at planting.

The number of replicates (n) was dependent on the number of available seeds and their germination rate. In iteration 1, 22 seeds were planted per experimental condition, and over the course of the entire experiment, featured a total germination rate of 92%. In iteration 2, 30 seeds were planted per experimental condition, leading to a germination rate of 96%. The total number of replicates and germination rate for each treatment condition is shown in Table 2-3 below.

Table 2-3. Evaluation of the germination rate for each treatment condition

Name	**Control**	**Control (2nd Iterate)**	**1 w/v%**	**2.5 w/v%**	**2.5 w/v% (2nd Iterate)**	**1 w/v% (Octuple feeding)**	**2.5 w/v% (Octuple feeding)**	**2.5 w/v% (Dodecyl feeding)**
Germination Rate	90%	100%	90%	95%	93%	95%	90%	97%
Experimental Replicates (n)	20	30	20	21	28	21	20	29

The height of flax plants under each of the treatment conditions was obtained after root biomass and branches were removed from the primary apical meristem. The results from this process are shown below in **Figure 2-16.**

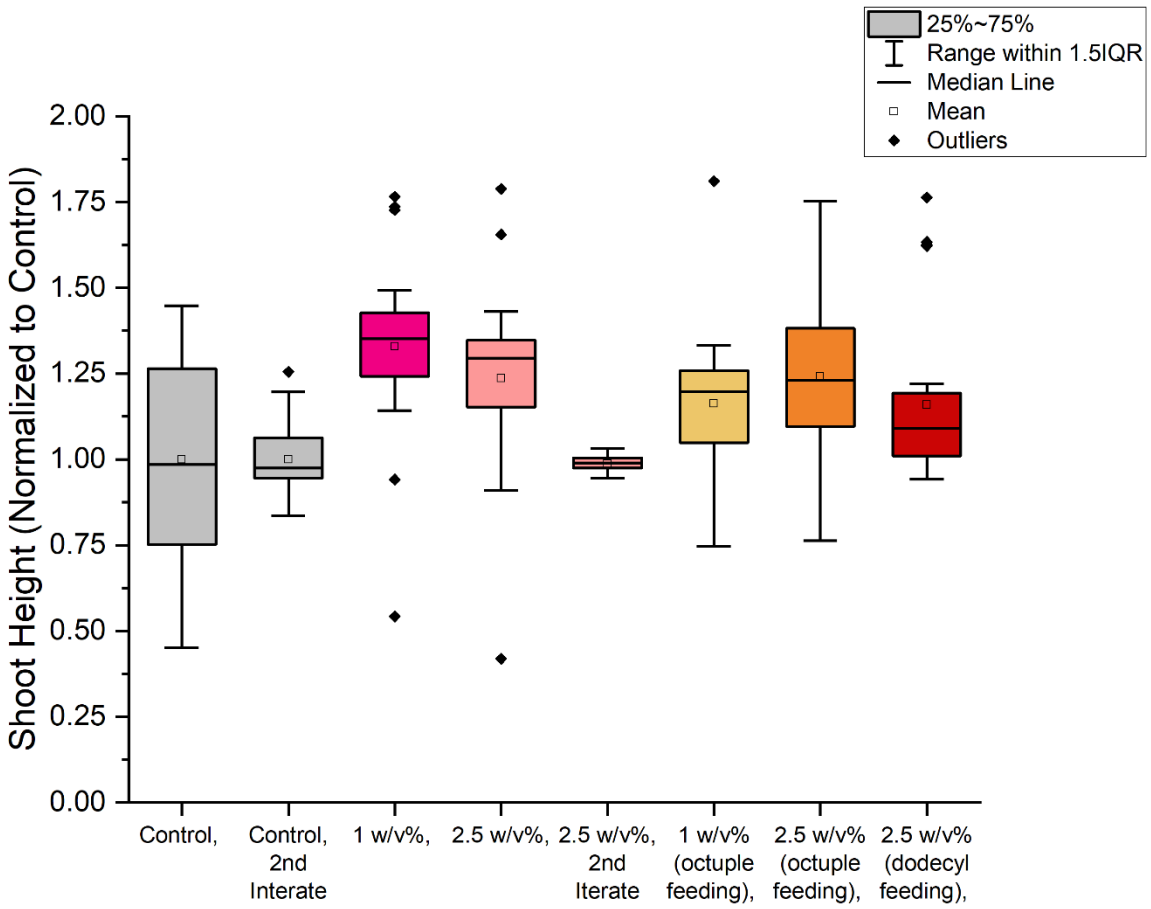


Figure 2-16. Shoot height of flax plants treated with cellulose nanocrystal. All heights were normalized to the control. Different treatment conditions are grouped by color, with similar treatment conditions across differing iterations being depicted by the same color.

Shoot height varied depending on treatment condition and sample set. Sample iteration 1 featured shoot heights larger than the control by 16% at the smallest and 33% at the largest. While the 2nd iteration of the experiment demonstrated smaller differences, the single 2.5 w/v% treatment group was 9% of the control, with the dodecyl feeding being 16% larger than the 2nd control iteration. Shoots were weighed fresh and then dried. The dried weights were collected to ensure standard comparison across treatment groups without the influence of transpiration or evaporation over the processing period. These weights are shown below in **Figure 2-17.**

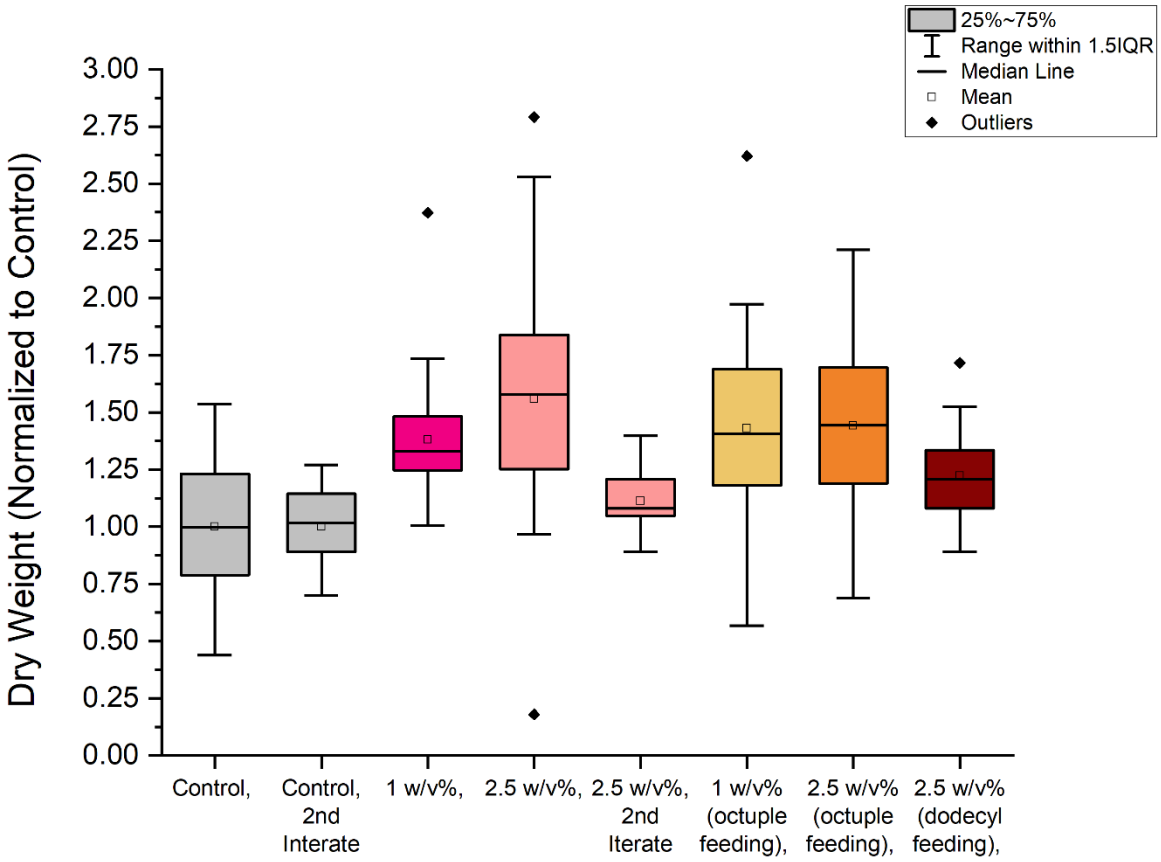


Figure 2-17. Dried weights for primary flax shoots treated with cellulose nanocrystal, normalized to the control.

Flax plants treated with CNC demonstrated dry weights of between 11% to 55% larger than the control. Variability in the data sets exist, with outliers being reported in four out of six treated groups. Additional iterations of experiments reduced variability when observing standard deviation. Despite the differences in the shoot height, all treatment conditions across both iterations demonstrated larger dry weights as compared to their respective controls. The mean plant linear density that is the mass of the plant divided by its respective height, is shown below in Table 2-4.

Table 2-4. Comparisons of plant linear density across various treatment conditions.

Name	Control	Control (2^{nd} Iterate)	1 w/v%	2.5 w/v%	2.5 w/v% (2^{nd} Iterate)	1 w/v% (Octuple feeding)	2.5 w/v% (Octuple feeding)	2.5 w/v% (Dodecyl feeding)
Plant Linear Density (mg/cm)	4.30	4.64	4.5	4.52	5.24	4.95	4.71	4.93

Treatments of nanocellulose significantly increased ($p_{2.5\ w/v\%}= 0.000033$, $p_{2.5\ w/v,\ dodecyl}= 0.028$) the plant matter index in the second iteration of the experiment.

2.2.2.1 Enhancement of Stem Morphology

Flax stems were sectioned to prepare for morphological observations. Cross-sections were obtained above the root node and below the leaf node in the lower third of the flax stem. From here, information on the cross-sectional area, phloem area, and crystallinity index of the stems were obtained. Cross-sectional area is displayed below in **Figure 2-18**.

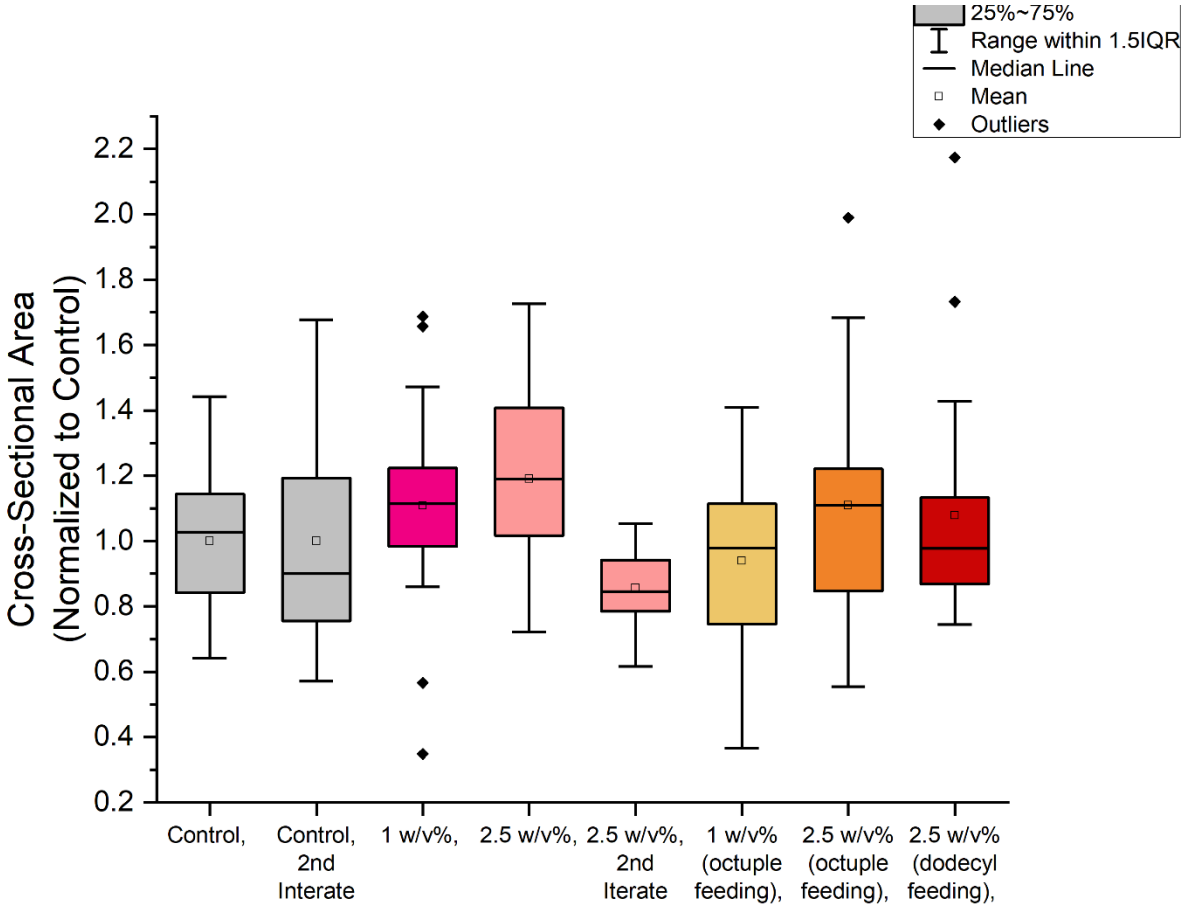


Figure 2-18. Cross-sectional area of treated flax stems normalized to control populations.

Initial iterations of cellulose nanocrystal treatments demonstrate an increase in stem cross-sectional area between 8% and 18% larger than the control. When the area of the hollow space/pith area is taken to account, the area of the cross-section occupied by plant matter decreases from as little as 4% to as large as 12% when compared to the control population.

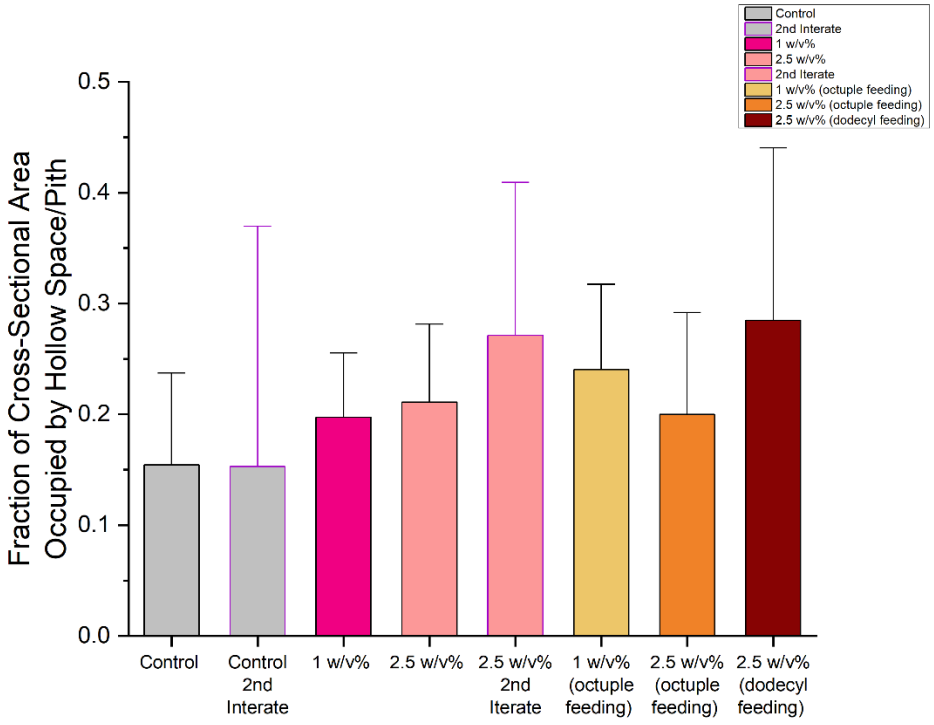


Figure 2-19. Fraction of cross-section occupied by hollow space/pith.

Table 2-5. Area density for treated flax plants based on the area occupied by plant matter-- excludes hollow space/pith area.

Name	**Control**	**Control (2^{nd} Iterate)**	**1 w/v%**	**2.5 w/v%**	**2.5 w/v% (2^{nd} Iterate)**	**1 w/v% (Octuple feeding)**	**2.5 w/v% (Octuple feeding)**	**2.5 w/v% (Dodecyl feeding)**
Plant Matter Area Density (mg/mm^2)	181.8	209.8	269.2	262.1	302.4	322.2	278.0	280.9

Despite variations in the cross-sectional area and the size of the hollow space/pith area, the mass per square millimeter increases significantly ($p_{1\ w/v\%} = 0.051$, $p_{2.5\ w/v\%} = 0.012$, $p_{2.5\ w/v\%,\ 2nd\ iterate} =$

5.1[10^{-7}], $p_{1\ w/v,\ octuple}$= 0.00033, $p_{2.5\ w/v\%,\ octuple}$= 0.019, $p_{2.5\ w/v,\ dodecyl}$= 0.00020) with application of cellulose nanocrystal. This indicates that, in addition to increases in the pith, other aspects of the plant morphology are altered with the addition of cellulose nanocrystal in the growth environment. By likening the phloem and xylem to elliptical rings, we were able to approximate the area of the phloem and xylem. These are shown below in **Figure 2-20.**

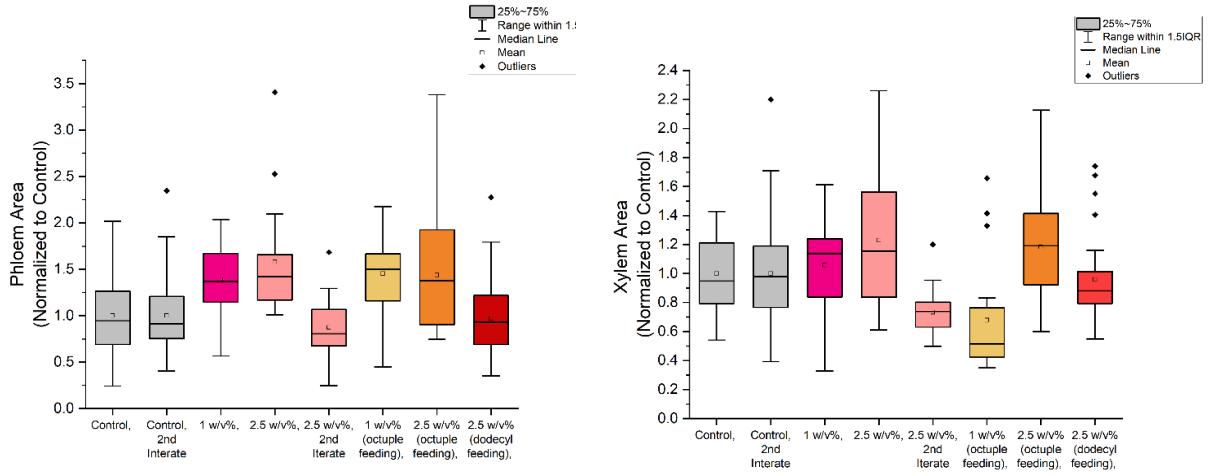


Figure 2-20. a) Phloem and b) xylem area normalized to the control population.

Phloem area is consistent with trends in the cross-sectional area. In iteration 1, the percentage of phloem relative to the amount of plant matter in the cross-section increased significantly with treatments of nanocellulose; iteration 2 features increases that were not significant at the 95% Confidence Interval ($p_{1\ w/v\%}$= 0.013, $p_{2.5\ w/v\%}$= 0.056, $p_{2.5\ w/v\%,\ 2nd\ iterate}$= 0.095, $p_{1\ w/v,\ octuple}$= 2.6 [10^{-5}], $p_{2.5\ w/v\%,\ octuple}$= 0.020, $p_{2.5\ w/v,\ dodecyl}$= 0.67). These values are shown below in **Table 2-6**, with the totality of the data shown in **Figure 2-21.**

Variability in the bast fiber area is consistent with variability observed in cross-sectional area. This variability could be due to physical differences in environmental conditions, including proximity to light, external environmental conditions, root system and water access. Between treatment

conditions, differences in the seed age, quality, and seeding time (winter, spring, or summer) can account for experimental distinctions in the two experimental iterations.

Table 2-6. Percentage of plant matter occupied (excluded hollow space/pith) cross-section occupied by bast fibers.

Name	Control	Control (2nd Iterate)	1 w/v%	2.5 w/v%	2.5 w/v% (2nd Iterate)	1 w/v% (Octuple feeding)	2.5 w/v% (Octuple feeding)	2.5 w/v% (Dodecyl feeding)
Percentage of Plant Matter Occupied by Phloem	19%	27%	25%	29%	31%	32%	26%	27%

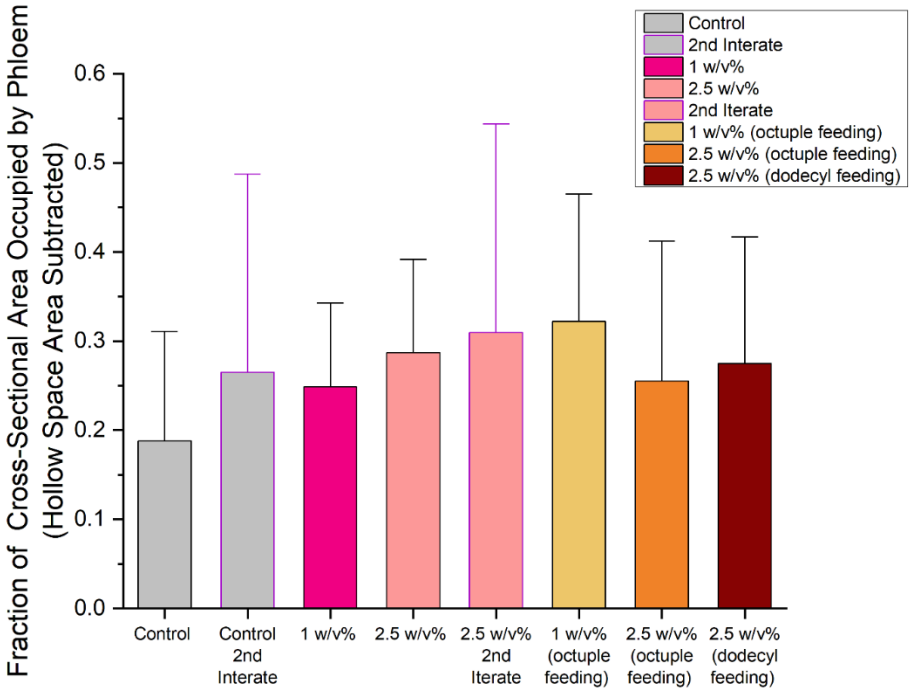


Figure 2-21. Fraction of the plant matter occupied cross-sectional area (excluding hollow space/pith) that is occupied by bast fibers.

2.2.3 Experimental Process Improvement and Comparisons between CNF and CNC

Initial experiments on cellulose nanofibril proved successful in affecting external parts of the plant properties, however difficulties remained with proving reproducibility in the experimental data. Many of these difficulties lie as a result of the cellulose nanofibril itself. The CNF, a paste, was hydrated about 90% with water. Due to the origin of the CNF, consistency was not exhibited throughout the sample. This means a given amount of cellulose nanofibril delivered to the plant could contain less or more than 10% CNF, and determining exact amounts would have proven tedious for the sample numbers tested. In addition to inherent variability in this non-engineered material, the water content of the CNF paste left it impervious to mold and degradation. After investigation, it was discovered that the CNF paste was being used well past its shelf life and, in order to maintain experimental integrity, transitioning to a different material system was necessary. The cellulose nanocrystal obtained was well-characterized, kept in dry conditions away from water. Creating a sonicated suspension with known cellulose nanocrystal amount allowed for a more direct and better controlled experiment. In addition to these changes, changes in the origin of the flax seed, decreases in the amount of flax plants grown per pot from 2 to 1, and an increase in the knowledge base for growing flax plants improved the baseline heights of treated flax plants. These experimental improvements are depicted in **Table 2-7**, where we look at the shoot length between experimental conditions.

Table 2-7. Differences in baseline flax shoot length between CNF treated and CNC treated plants.

Characteristics	**Control (CNF)**	**Control (CNC)**	**0.23g Single (CNF)**	**2.5 w/v% Single (CNC)**	**0.23g Weekly (CNF)**	**2.5 w/v% Octuple (CNC)**

Shoot Length	25.0 ± 3.4 cm	30.8 ± 9.1 cm	26.1 ± 6.5 cm	38.1 ± 8.82 cm	26.8 ± 4.7 cm	38.3 ± 7.9 cm

In addition to the baseline increase in growth (5 cm) between control treatments, additional growth is observed in CNC treated plants as compared to CNF treated flax plants. These plants exhibit 7 cm additional growth in shoot length over the 5 cm baseline increase attributed to improved experimental parameters. This increase highlights how the morphological differences in the structures of cellulose nanofibril and cellulose nanocrystal provide differing effects in flax plants.

2.2.4 Hypothesis on the Enhancement of Growth

Plant growth is regulated by hormones that reside in the plants organ system. These hormones respond to stimuli induced by the presence or absence of sunlight, water, and nutrients, but can even be regulated with the presence of environmental factors such as wind. The presence of carbohydrates in the soil can lead to carbohydrate modulated upregulation of the gene that codes for plant growth[76].

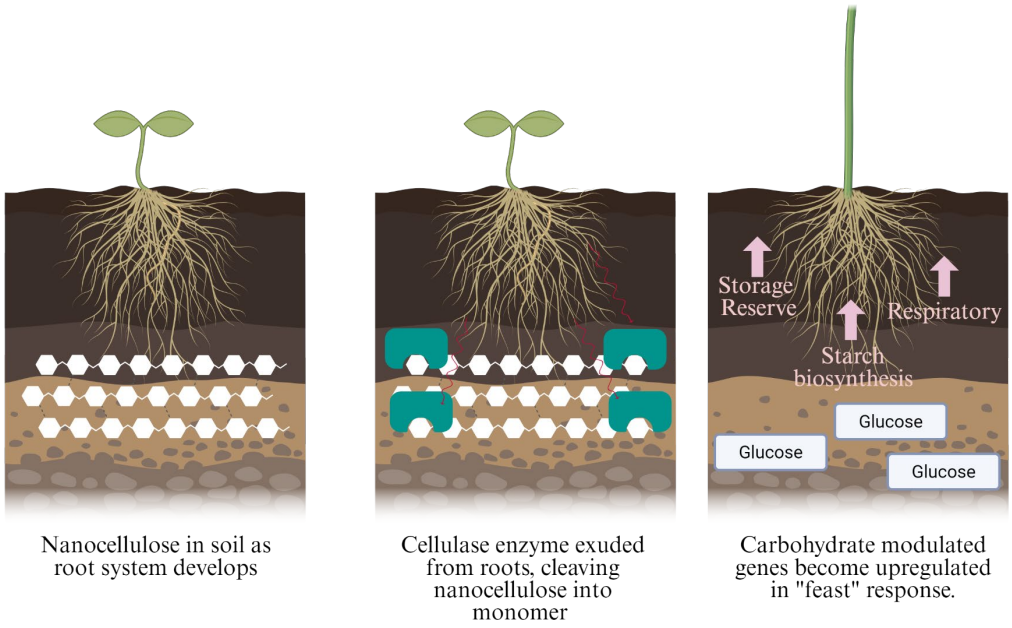


Figure 2-22. Enzyme cleaving mechanism for nanocellulose enhanced upregulation of growth.

Enzymes found either exuded by microbes in the soil, or exuded from the flax root cap, make their way to the cellulose nanoparticles located near the emerging roots. From there, cellulose nanocrystal is broken down into smaller and smaller repeat units until, finally, free glucose is available. It is this carbohydrate unit that promotes the upregulation of growth. The chemical mechanism is depicted in the figure below.

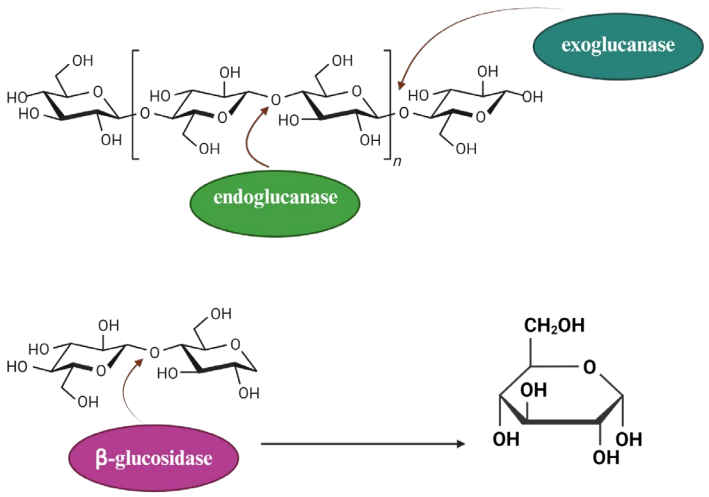


Figure 2-23. The enzymatic cleavage of polymeric cellulose to glucose, the monomer unit.

Additional polymer chain lengths in the case of cellulose nanofibril may provide an explanation as to why cellulose nanocrystal provide larger and more consistent changes in growth between the control and treated populations. While the process of cleaving interior bonds, in the case of endoglucanase, is not rate-limited by the amount of substrate[77], it is the case that longer polymer chains do require more instances of enzymatic cleavage to reach the monomer stage. Due to the insolubility of nanocellulose in water, nanocellulose remains present at the site of the root to allow for continuous upregulation. Water, however, is important in the second step of enzyme catalysis, thus creating a positive relationship with regards to the presence of water. Finally, carbohydrates at large amounts may induce a downregulation of certain genes[76] and at excessive amounts may even induce stress responses in the plant[78]. These effects may explain diminishing effects seen in prolonged exposure of flax plants to cellulose nanoparticles.

2.3 Conclusion

In this chapter, we have observed how cellulose nanoparticles induce changes in height, mass, and morphology of flax plants. In experiments in which soil-grown flax plants were exposed to cellulose nanofibril (CNF) preparations, flax plants experience significant increases in the mass of mature flax plants in both single and weekly treatment conditions over the course of their three months growth cycle. However, significant changes in the roots and secondary shoots were not observed, and thus did not become the subject of subsequent studies. When soil-grown flax plants were supplemented cellulose nanocrystal (CNC) preparations, significant changes in the height and weight were observed across widely varying treatment conditions. These conditions included a high and low weight percent, a treatment only once at germination, a treatment condition where CNC was delivered once a week for eight weeks (octuple) and one condition where CNC was delivered once a week for 12 weeks (dodecyl). Mass increased significantly for each of these treatment conditions at the 95% CI. With CNC, we were able to investigate the size increases in cross-sectional area, and how the plant matter area density and linear density are impacted by treatment condition. While the hollow space/pith area increased for treated plants, the ratio of their mass to cross-sectional area (excluding this hollow space) also increased. This indicates that the area of plant matter in the plant is increasing irrespective of the hollow space area. The fraction of cross-sectional area of treated plants is, at best, larger than that of the corresponding control plant or, at worst, the same as the control. CNC outperforms CNF when comparing lengths and masses of treated stems. This may be explained by morphological differences in the two cellulose nanoparticles, particularly the size in nanometers and the polymer chain length. For our hypothesis, which is driven by enzymatic cleavage of the cellulose nanoparticle by enzymes found in soil, shorter size and chain length would facilize this process by requiring fewer enzymes and energy. Next steps of this chapter are to confirm whether improvements in growth correspond to

improvements of mechanical properties of fibers extracted from the phloem region of CNC treated flax stems.

Chapter 3 Modification of Mechanical Properties in Nanocellulose Treated Flax Stems and Fibers

3.1 Materials and Methods

3.1.1 Preparation of Flax Stems for Mechanical Testing

After drying and post-processing of treated and control flax plants, 5 cm cuttings were obtained from above the root node and below the snap point using garden shears, targeting the thickest internode location for each individual plant. The ends of the plant were lightly sanded and, using an Olympus GX51 Inverted microscope, cross-sectional area measurements were obtained for each stem. The plant cuttings were dipped in Gorilla Glue epoxy up to 1 cm deep in order to obtain a tacky surface for tension measurements.



Figure 3-1. Stem samples created for tensile testing.

The epoxied stems cured at room temperature before testing on TA XT Plus Texture Analyzer (New Castle, DE) with a 5 kg load cell and an extension rate of 1 mm/min. From the force-displacement curves generated from the test, maximum strength and tensile modulus were obtained.

3.1.2 Preparation of Flax Fibers for Mechanical Testing

Flax stems grown and treated in growth chambers were oven dried at 80 ºC until all water had evaporated from the plant—this process took around six hours for the flax plants in these experiments. Using enzyme retting conditions defined by Singhal et. al[54], plants were retted for 24 hours in an acidic buffer solution with 2% pectinase enzyme. They were subsequently dried at room temperature, then broken and hackled by hand, to obtain unidirectional fibers for each treatment condition.

Fibers were mounted in paper frames as defined by ASTM C1557-20[79], and as in accordance with procedure developed by Steven Mamolo and Dr. Amy Langhorst[80]. Fibers were adhered, using double-sided carbon tape, to a paper frame with a 25 mm gauge length. Following mounting, a small drop of JB Weld 33301 Total Repair - Accelerated Instant Cure Super Glue was added to fix the fiber to the tape and frame.

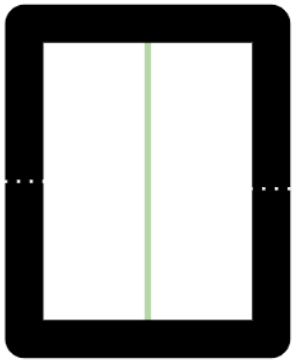


Figure 3-2 Diagram depicting single fiber tensile testing.

Frames were mounted onto an Instron 68SC-1 (1 kN load cell). The paper frame was cut, and samples were tensed at an extension rate of 0.01 mm/s until fibers failed.

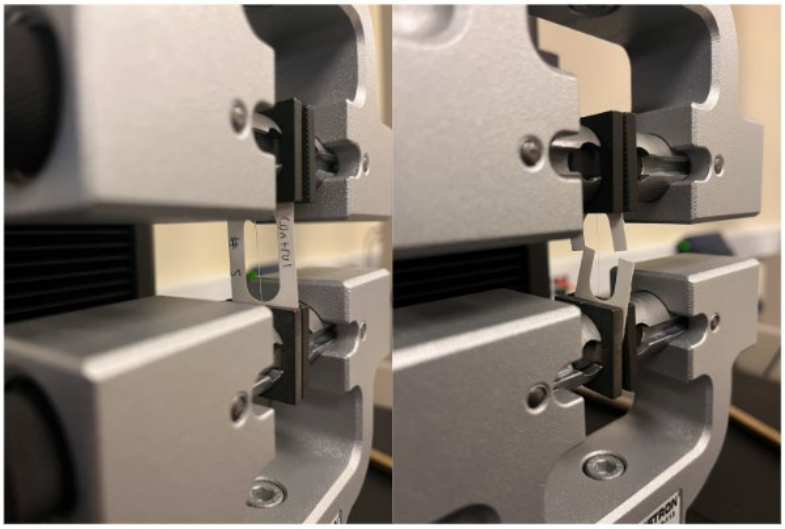


Figure 3-3. Flax fiber before and after single fiber tensile testing.

Before and after fibers were tested, their cross-sectional area was obtained using an Olympus GX51 Inverted microscope.

3.1.3 Statistical Modeling[81] for Fiber Mechanical Behavior

Weibull distribution is the statistical method for characterizing variability in a fiber's mechanical properties. The shape parameter and scale parameter characterize the model, which has been used in hemp fiber models to assess the presence of fiber defects, as the assumption in Weibull analyses is that the initiated failure mode leads to the critical and complete failure.[81]

The two parameter Weibull model is defined by the following **equation**[82]:

$$P(L,\sigma) = 1 - e^{[-\frac{L}{\delta_0}(\frac{\sigma}{\sigma_0})^m]} \qquad \text{(V)}$$

$P(L,\sigma)$ is the probability function for failure of a single fiber with length L under an applied stress which approaches but does not exceed σ. σ_0 is the scale parameter—characteristic failure stress—and m is the shape parameter as defined previously. δ_0 is the reference characteristic length of the fiber. The shape parameter gives the uniformity and reliability of the fibers, which can be used to

draw comparisons between test groups.[82] For fiber bundles, the equation used to determine the model parameters is given from the tensile force-strain curve, *F*-ε. We assume that δ_0 is equal to L, due to the construction of the test length. With this adjustment, we can rearrange the above equation by:

1. Subtracting both sides of the equation from 1.
2. Naturalizing both sides of the equation to remove the terms in the exponential.
3. Naturalizing again to bring *m* out of the exponential.

This process leaves us with **Equation 6**[83], which is shown below:

$$\ln\left(-\ln\left(1-P(\sigma,L)\right)\right) = m\ln\left(\frac{\sigma}{1\ GPa}\right) - m\ln\left(\frac{\sigma_0}{1\ GPa}\right) \qquad \text{(VI)}$$

This linearization can be used to determine the shape parameters for the Weibull analysis. *m* is given by the slope of a line of best fit to **Equation 6.** To calculate σ_0, we will divide the negative intercept of the line given by (V) by the Weibull modulus, *m,* and exponentiate it.[83]

In order to begin this process, fibers are tested to their failure and then ranked in order of their stress, represented by *i.* The lowest value is given *i*=1, and every subsequent value is assigned a number up to the number of tested samples *N*. These values can be used to calculate the failure probability, *P*, given by the following function:

$$P(\sigma,L) = \frac{i-0.5}{N} \qquad \text{(VII)}$$

Finally, this gives us a method with calculable values for determining the *m* and σ_0 by determining the stress of the fiber at failure.

The Griffith model[84], which has typically been used to describe brittle fracture in elastic solids, can also be applied to fibers. Previous explorations using Griffith Theory for natural fibers have centered around hemp fibers[81]. Similarities in the structure of hemp and flax fibers may indicate that the Griffith model may be an excellent choice to further understand the reliance of fiber

diameter (d_f) on the variation in tensile strength (σ_f) and Young's modulus (E). The equations to support the Griffith model are presented in **Equations 8 and 9**[81].

$$\sigma_f\left(d_f\right) = A + \frac{B}{d_f} \qquad \text{(VIII)}$$

$$E\left(d_f\right) = A + \frac{B}{d_f} \qquad \text{(IX)}$$

By plotting tensile strength and Young's modulus as a function of the inverse fiber diameter, we will be able to define the Griffith parameters, A and B. However, the model itself—not the parameters—is what informs us on the reliance of each parameter on the fiber diameter.

3.2 Results and Discussion

3.2.1 Mechanical Behavior of Flax Stems

With large strength disparities existing between fibers on the market and flax fibers, stiffness ruled application of flax fiber composites are of particular interest. With this existing knowledge, we

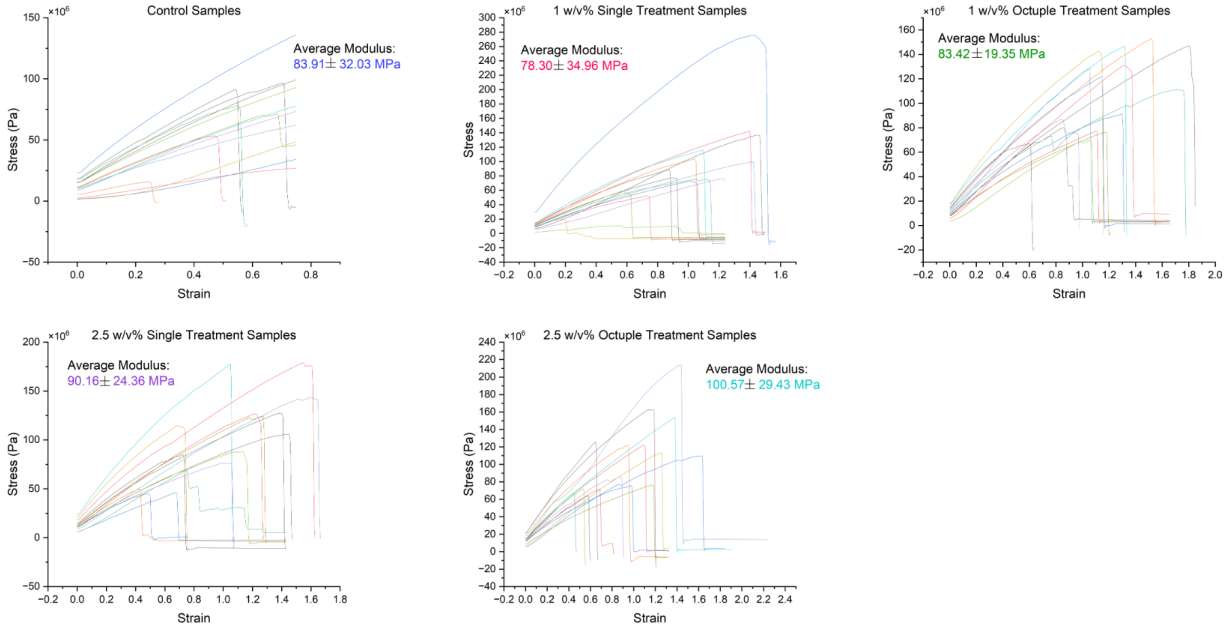


Figure 3-4. Tensile modulus for treated flax stems.

can also predict other industrial applications of flax fiber composites. These can be described as crushed-stem composite materials, which can be used as filler, but can also have cosmetic applications. Crushed-stem composite materials can have both strength and stiffness applications and, as such, both data sets are presented.

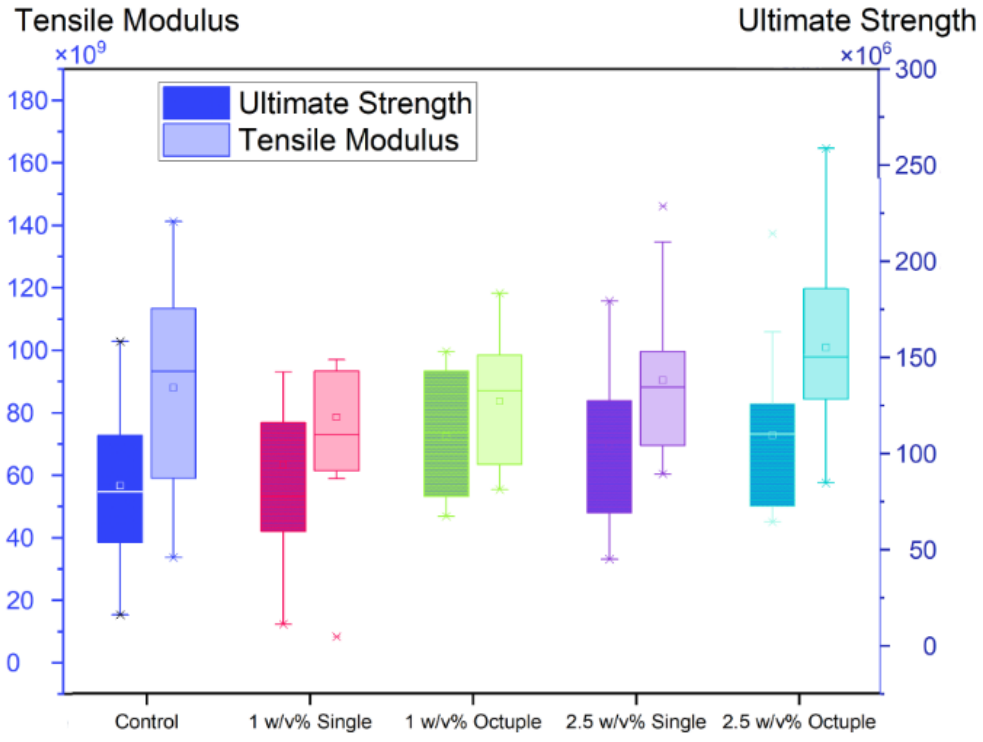


Figure 3-5. Ultimate strength and tensile modulus values for CNC treated flax stems.

Tensile modulus values were low, comparatively, for automotive applications. Due to the nature of the test and the morphology of a flax stem, the individual strength of the phloem fibers does not dictate the failure mode. Similar to how a composite material contains unidirectional fiber and matrix materials, a plant stem is a multicomponent composite with fibers (cellulose), xylem (lignin), and sugars such as hemicellulose and pectin which act as the matrix material. As such, strength and modulus values on tested stems may only indicate the strength of the fiber-xylem-

matrix relationship. While this may be an indication of growing a better plant, tested values were not statistically significant at the 95% confidence interval, as explained on Page 32.

3.2.2 Mechanical Behavior of Flax Fibers

Using an Instron with a 1 kN load cell, tensile testing was performed on mounted single fibers from each test condition. Eleven total samples were tested for each group, with varying degrees of success. Unsuccessful samples can be categorized as those that failed at the grip, samples with epoxy-fiber interactions during sample preparation, or samples that failed to yield under stress before the software automatically completed testing (thus removing all load from the sample). Eight samples were analyzed for the control sample set and the single treatment sample set, while ten samples were analyzed for the weekly treatment sample set. Cross-sectional areas were calculated by selecting five pairs of representative points along the fiber's major and minor axes after failure, then by using the area of an ellipse formula described in Equation $\text{Area}_{\text{ellipse}} = \pi AB$ (I) to determine an ellipsoidal area for each point. These points are then averaged to ascertain the cross-sectional area used in calculations for stress.

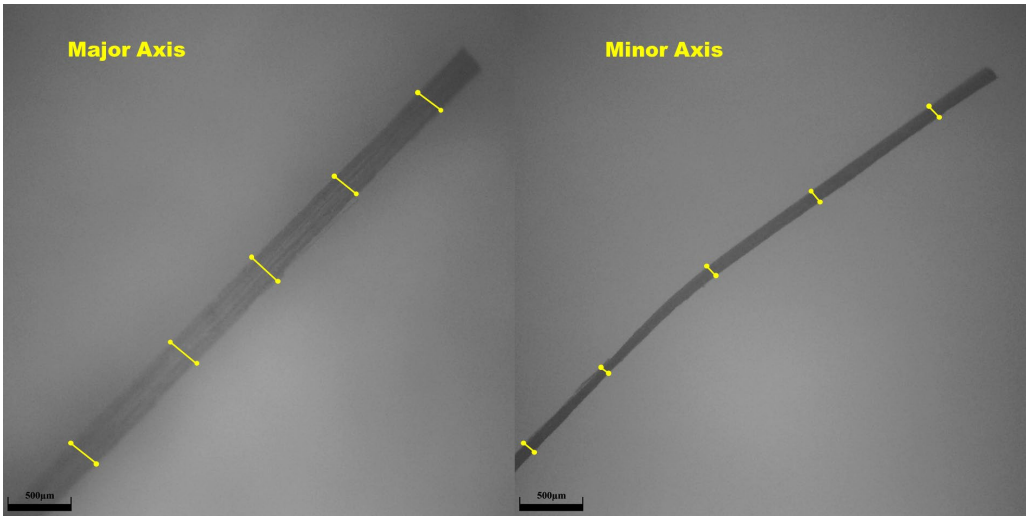


Figure 3-6. Representative points for calculating cross-sectional area of a flax fiber. These points are taken using ImageJ imaging software and then halved to determine radius.

Stress-strain curves were developed for all treatment groups. Young's modulus was recorded from the slope of the given by the stress-strain curve until failure.

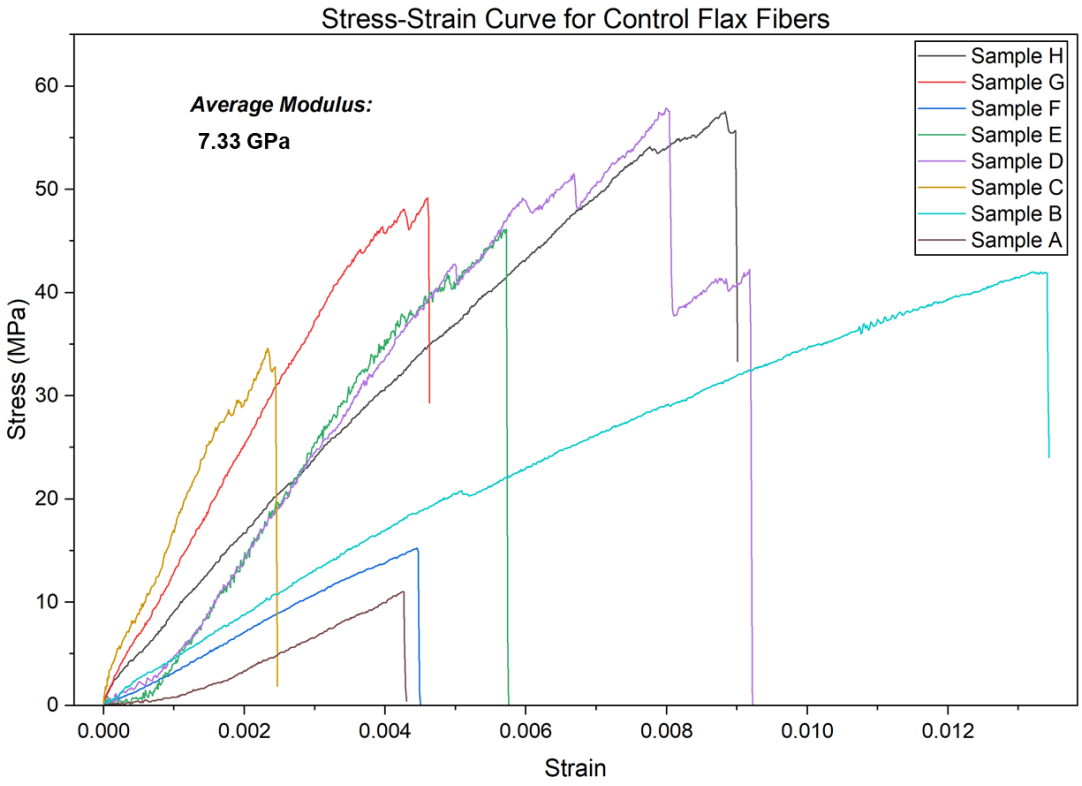


Figure 3-7. Stress-Strain Curve for Control Flax Fibers.

Control flax fibers demonstrated an average modulus of 7.33±4.14 GPa. Because a flax technical fiber is made up of many elementary fibers, the stress-strain curve reflects areas of the technical fiber where an elementary fiber carrying some load had ruptured.

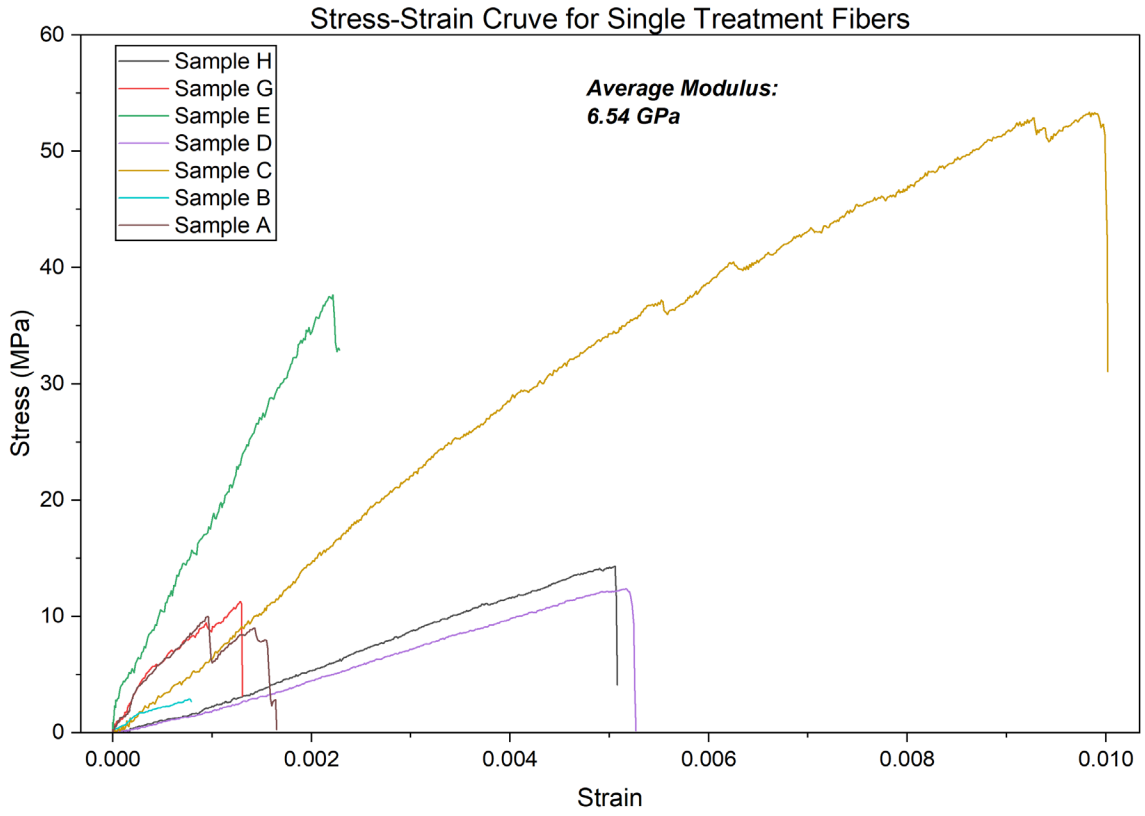


Figure 3-8. Stress-Strain Curve for Single Treatment Flax Fibers.

Single treatment flax fibers exhibited the lowest average modulus of the treatment groups, with an average modulus of 6.56±4.88 GPa. One tested sample in this group was excluded from analysis due to the presence of epoxy on the fiber which contributed to abnormally high fracture stress and modulus values. These values do not differ significantly from the control samples, which suggests that Young's modulus is not significantly impacted by treatments of cellulose nanocrystal.

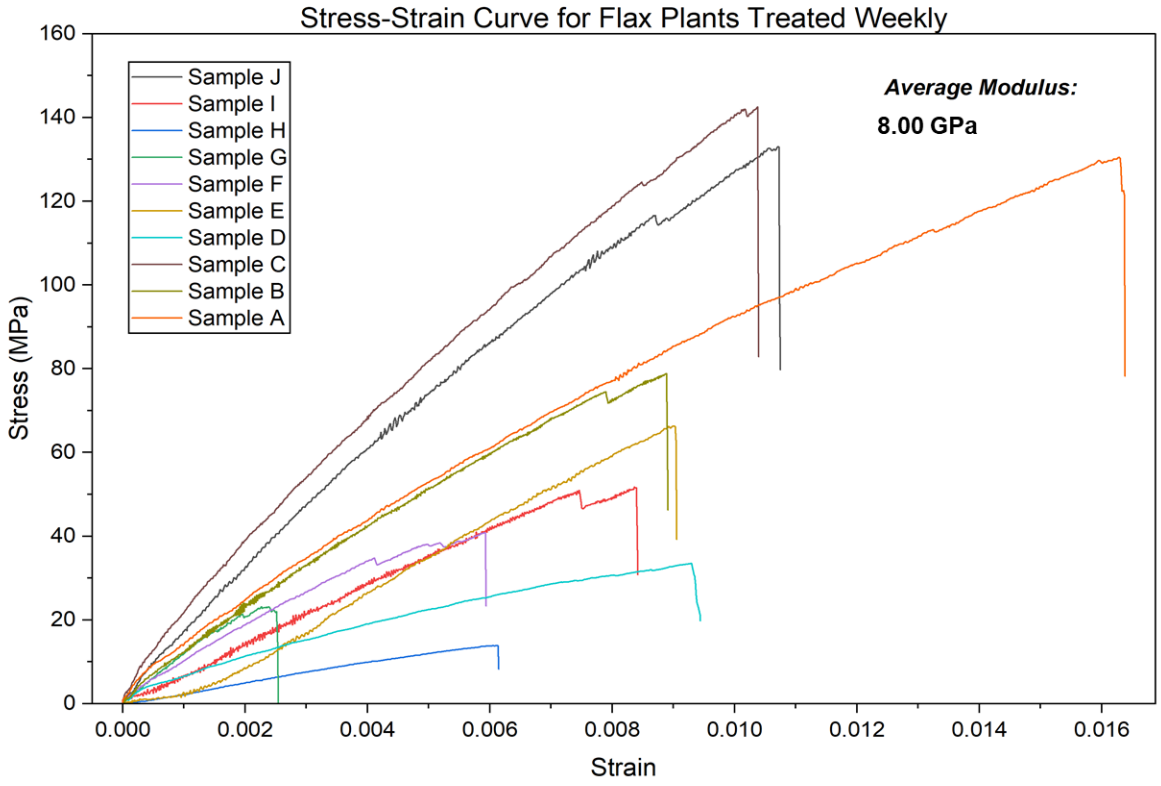


Figure 3-9. Stress-Strain Curve for Weekly Treatment Flax Fibers.

The weekly treatment group exhibited an average modulus of 8.00±3.46 GPa. While larger than both the control and single treatment samples by approximately 1 GPa, these differences were not enough to constitute significance at the 95% confidence interval. Statistical differences are hindered by large amounts of variation in the data set with low sample replicate number. Further experiments will make use of written programs to increase the number of points gathered to determine the cross-sectional area from 5 to approaching infinity. Fracture cross-sectional area, in some cases, differed drastically from areas recorded across representative points in the sample.

Weibull probability analysis returns predictive information on the reliability and variability of our parameter of interest, in this case failure stress, for the tested fibers. Using a Weibull analysis, we

were able to obtain the shape parameter/modulus m and scale parameter σ_0 for all treatment groups. This is shown below in **Table 3-1**.

Table 3-1. Weibull shape and scale parameters for tested fiber treatments.

	Shape Parameter (*m*)	**Scale Parameter (σ_0)**
Control	1.83	45.91 MPa
Single Treatment	1.076	15.24 MPa
Weekly Treatment	1.55	74.00 MPa

The shape parameter, which is similar in the three treatment conditions, defines the wideness of the distribution model. The low value shows the inherent variability of the flax fibers, which allows for a wide range of stresses at which a flax fiber can break. The decrease in shape parameter for the treated fiber groups demonstrates a slightly higher propensity for variability than the control group. To use the Weibull model to determine differences between the treatment groups, we must look at the scale parameter, which represents the value at which 63.2% of fibers will break[81]. Weekly treatment fibers, which also exhibited a higher stiffness, have a higher scale parameter than the single treatment fibers. This is a higher threshold value for fiber failure than what is exhibited in the single treatment group.

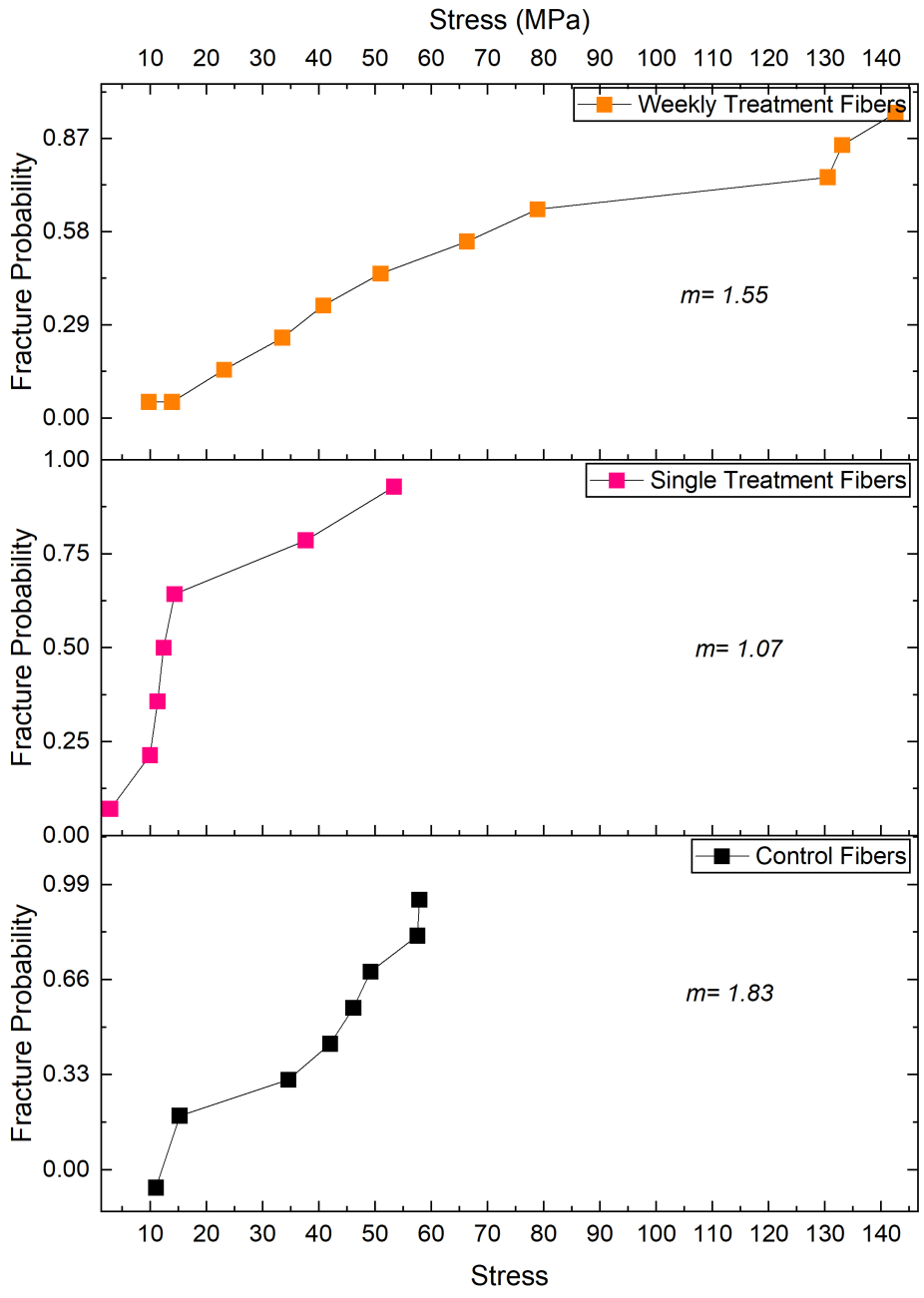


Figure 3-10. Weibull model analysis for all treated stem showing fracture probability versus stress.

In all cases, higher stresses increase the likelihood of sample failure. In control stems, we see a vast steepening of the fracture probability as fibers approach and exceed 50 MPa of stress. This is opposed to single treatment fibers, which have a steep slope at low loads—10 MPa or less—before

the slope declines at increasing loads. Weekly treatment fibers demonstrate consistent fiber fracture probability for a long range of stresses, with a slope increase at 128 MPa. This occurs well after the characteristic stress is reached. The number of samples tested is remarkably low for what is expected for a Weibull probability analysis. Weibull analysis is typically used when N≥100 samples, but can be reliable in cases where N≥50. Therefore, Weibull can offer a great prediction into the fiber reliability, but the model itself may not be reliable for this case until at least 40 more samples are tested. This is the subject of interest for future work, as outlined in Appendix B: Growth of CNC Treated Flax Plants on Small-Farm Scale.

A Griffith model can be used to help assuage this variability by assigning an equation to the relationship between fiber diameter and fracture stress or Young's modulus. Before assigning a model, the Griffith's parameters *A* and *B* were calculated for all treatment conditions.

Table 3-2. Griffith's Parameters for flax fibers treated with nanocellulose.

	A_{stress}	B_{stress}	$A_{modulus}$	$B_{modulus}$
Control	34.16 MPa	0.934 MPa·mm	2.24 GPa	0.944 GPa·mm
Single Treatment	11.95 MPa	1.75 MPa·mm	1.21 GPa	1.13 GPa·mm
Weekly Treatment	6.72 MPa	14.57 MPa·mm	7.51 GPa	0.112 GPa·mm

The model's parameters give an insight into the relationship of the fiber diameter to the stress and modulus.

It is important here to remember that while a linear fit is used to determine the Griffith's parameters, it may not be the best way to categorize the mechanical behavior of the fibers relative to their diameter. Additional regression models must be used to determine the best fit[81]. Typically,

a regression model is added until the largest R^2 value is reached however, due to low sample number and non-engineering of the material, some of the regression models of best fit may not be the most accurate to describe the data. As such, polynomial regressions were avoided.

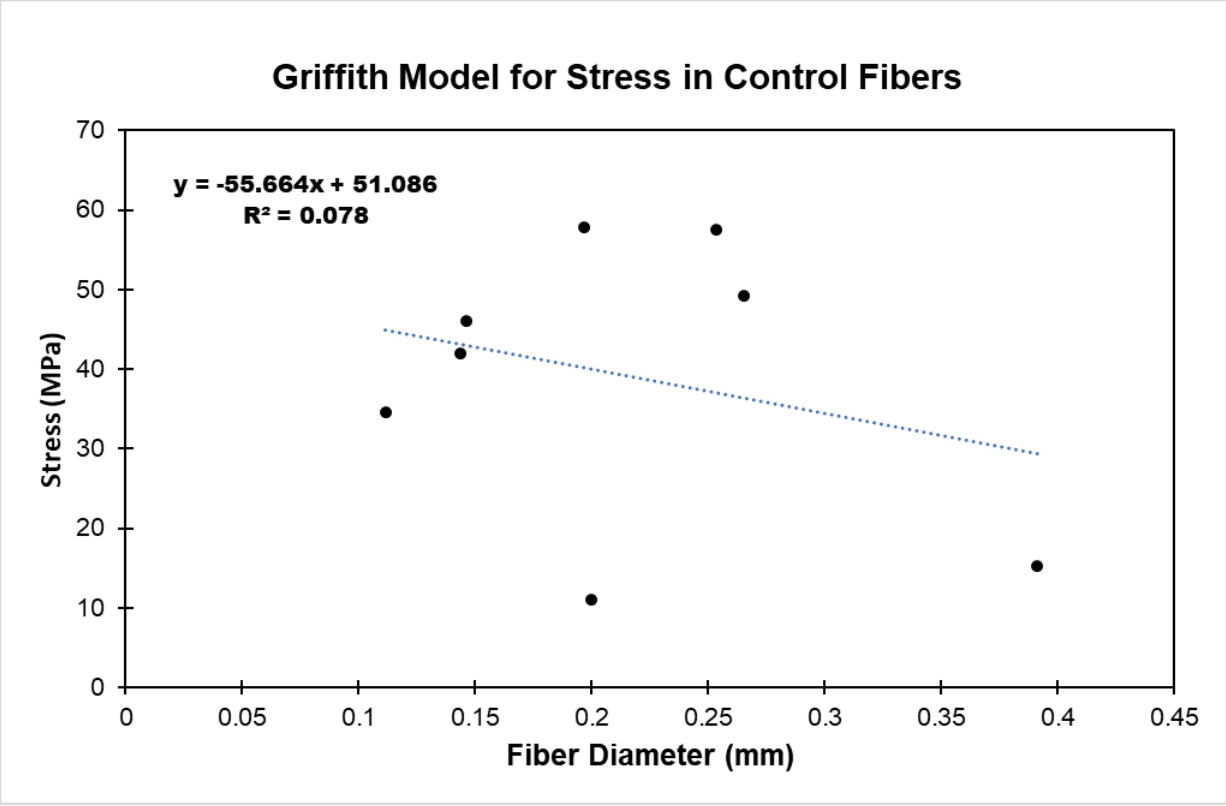


Figure 3-11. Calculated regression model of strength at break for control flax fibers.

Several models were used to determine a fit with the highest R^2 value for categorizing the dependence of fiber diameter on tested mechanical properties in control fibers. Stress seemed to have very little reliance on the fiber diameter, based on regression models, for the control fibers. While we know this not to be the case—particularly because stress is calculated with $\frac{d}{2}$ as one of the multiplicands—the model makes it clear that additional factors may contribute to the non-uniformity of the data set. This may due to fiber defects, such as pores and kink bands, or the rupturing of elementary fibers.

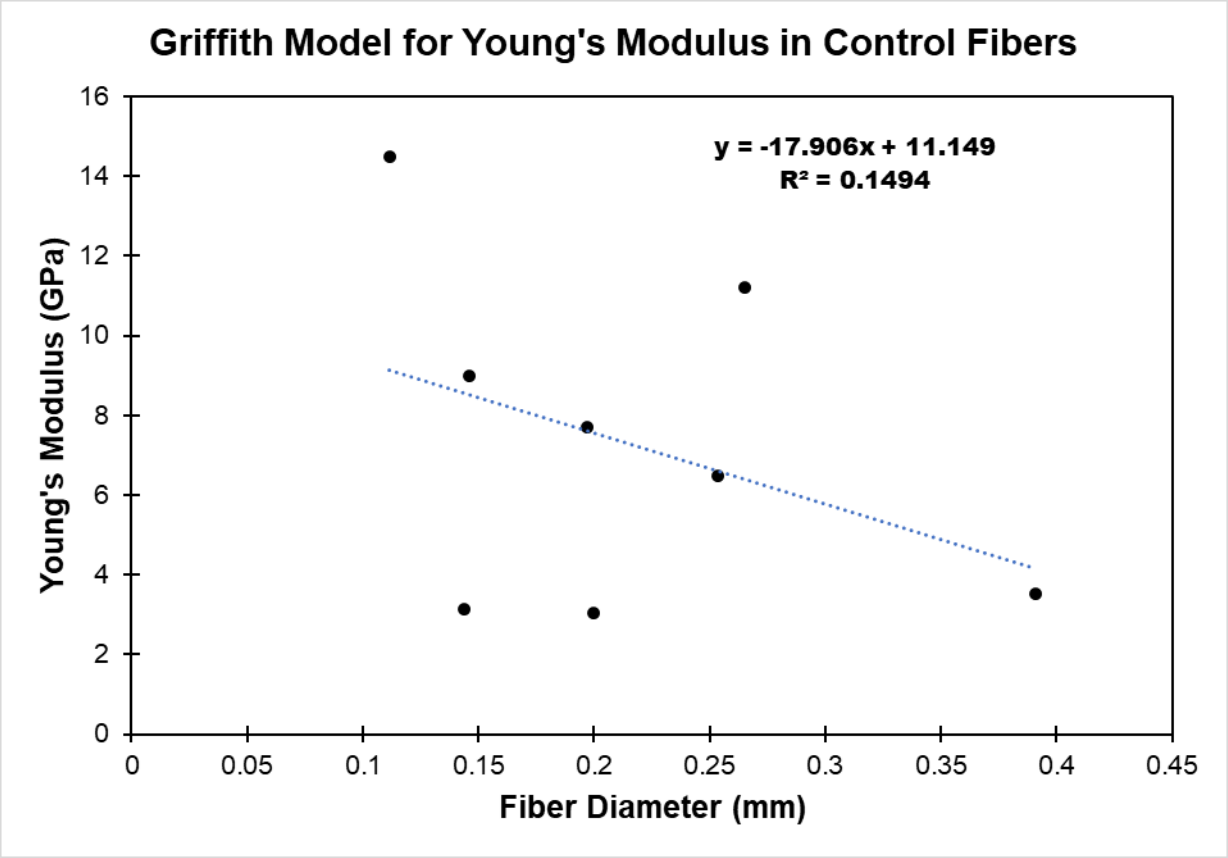


Figure 3-12. Regression model of Young's modulus as a function of fiber diameter in control flax plants.

Young's modulus, also directly related to a fiber's diameter, appears to have a slightly more linear nature to the data points. However, in the absence of additional understanding, well developed trendlines struggle to be made. Instead, what we can derive is there may not be an established trend between fiber diameter and Young's modulus, due to inherent variability in the fiber that effect the modulus.

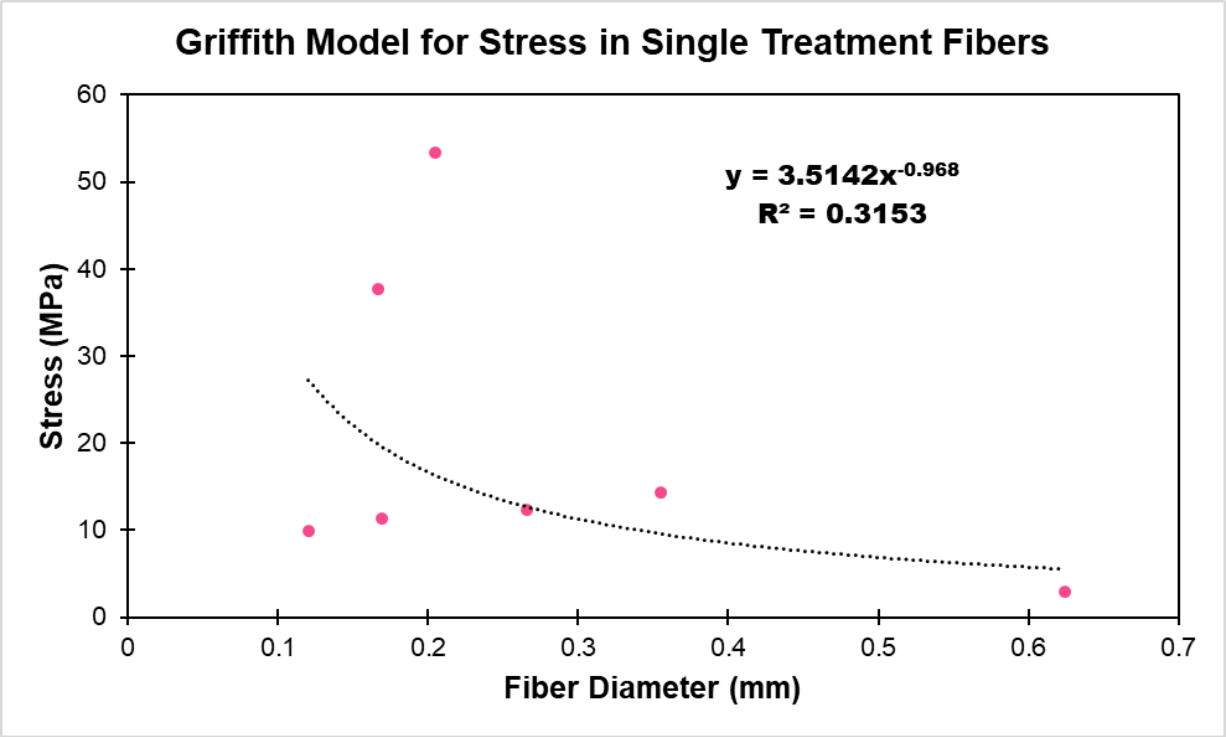


Figure 3-13. Regression model of strength as a function of fiber diameter in single treatment flax fibers.

For single treatment fibers, a negative exponential fit is was used to analyze this dataset. We would expect, as fiber diameter enlarges, that stress would decrease[85]. That case is confirmed for fibers treated once at germination. It also suggests that small fibers of similar diameter may vary much more vastly in their stress than fibers of larger diameter. Larger variation in thinner fibers can be related to previously mentioned fiber damage (kink bands, pores) and to scutching damage which would present most impactfully on thinner fibers, as thinner fibers have fewer elementary fibers which can share load. In **Figure 3-13**, we can see the results of this, which appear alternate to the trendline. Smaller data points have less max stress than their near neighbors.

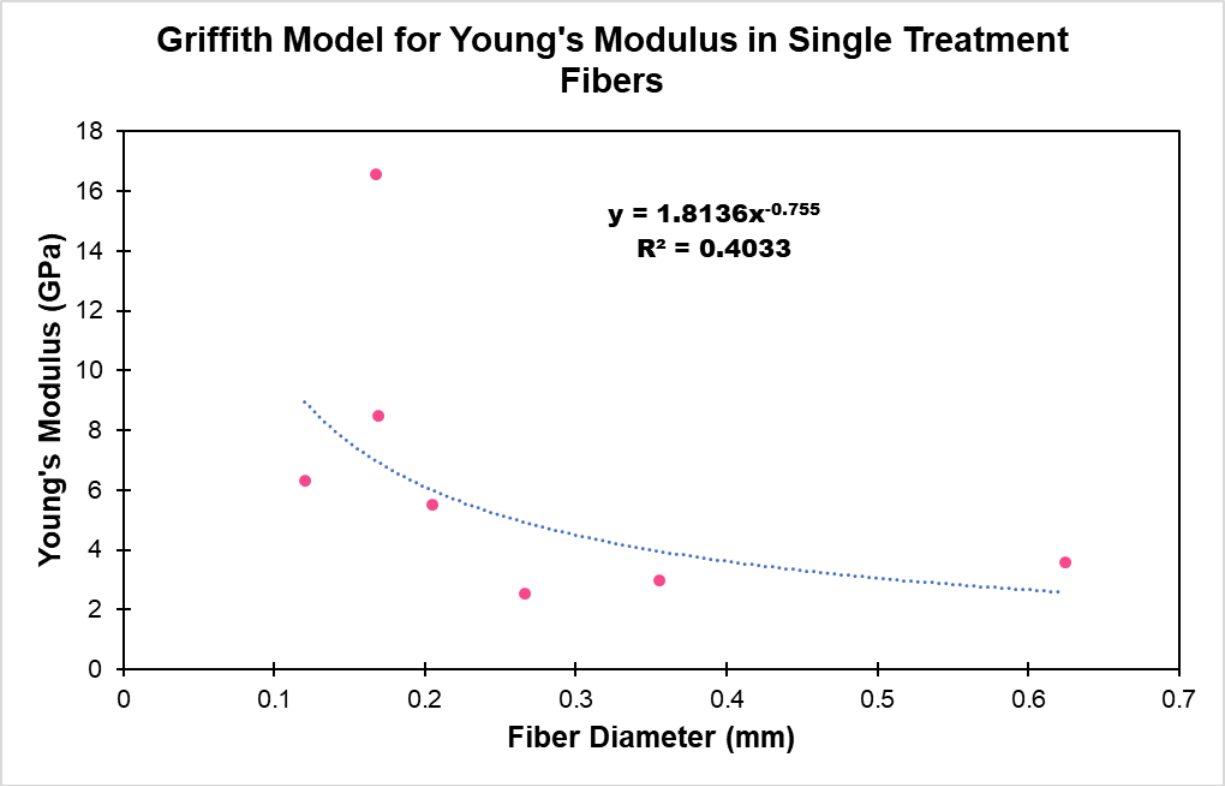


Figure 3-14. Regression model of Young's modulus as a function of fiber diameter in single treatment fibers.

Young's modulus, like stress, should have an inverse-relationship with fiber diameter[85]. While still expressing attributes of irregularity, the trendline fit to this dataset has a 40% accuracy. Additional data points may strengthen the fit in areas where data is limited, such as between 0.4 and 0.6 mm, and below 0.1 mm in fiber diameter.

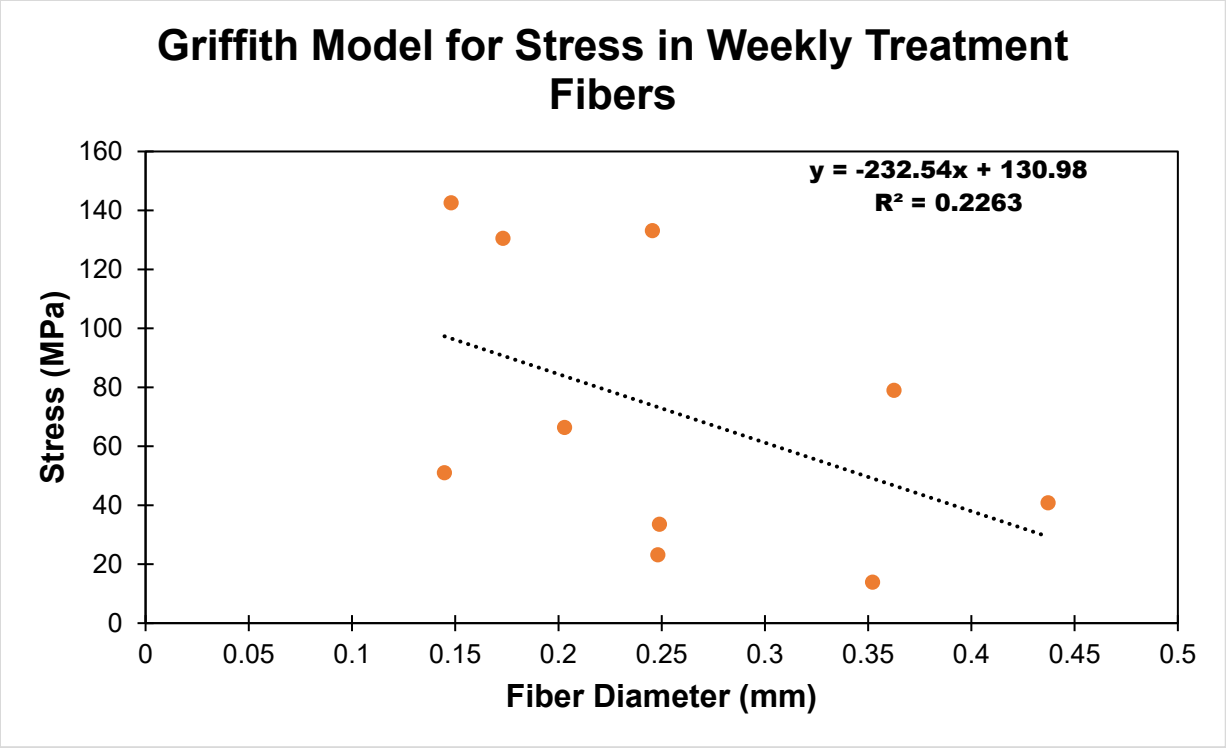


Figure 3-15. Regression model for strength as a function of diameter in weekly treatment fibers.

Weekly treatment fibers do have a fit of 23% accuracy which holds with expected trends for the relationship between stress and fiber diameter. Not a single tested point exists on the trendline, and for fiber of the same diameter, of which there are many, there are a vast range of potential fracture stresses. For the fibers at 0.25mm, fracture stress ranges from 20 MPa to 140 MPa. This corresponds to a fracture probability of 10% or 90% depending on the sample selected. This points to large differences in the sample integrity, which could be investigated with advanced imaging techniques—x-ray tomography and electron microscopy to name a few. Cases have shown wood pulp fibers show no obvious trends were observed between fiber diameter and Young's modulus[86] meaning fiber origin and variability may impact this relation.

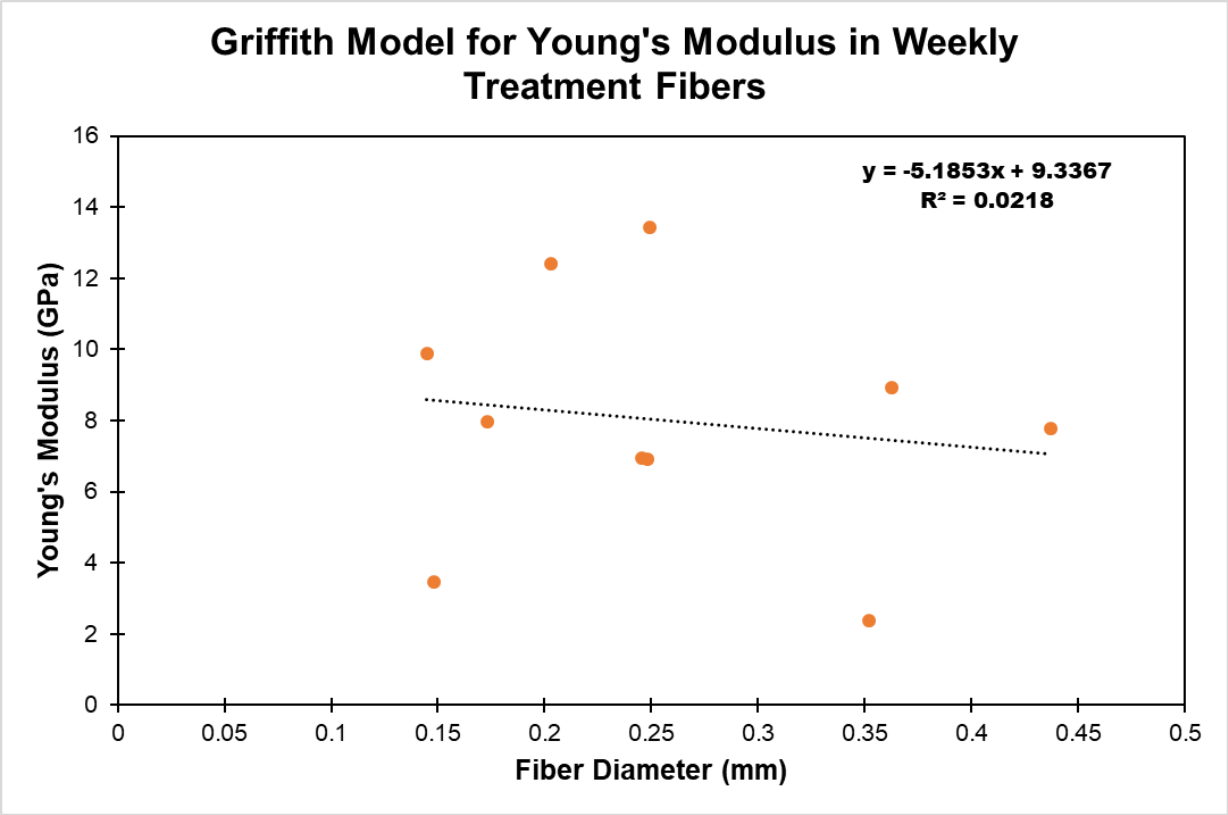


Figure 3-16. Regression model for Young's modulus as a function of diameter in weekly treatment fibers.

With higher replicate values and the introduction of this additional vantage, a simulation and corresponding model could be created to predict fiber yield strength, ultimate strength, and modulus depending on the treatment condition and the fiber diameter. Advanced models would be able include the number of elementary fibers in tested technical fiber bundles. These innovations would help inform composite making by offering predictive information into composite properties and inherent variability in an amount of flax fibers.

3.3 Conclusion

Stems for treated flax plants have marginal, but not significant, increases in their Young's modulus as compared to control flax stems. When extracting fibers from the treated plant groups, retted stems in the single treatment group had more facile hackling, leading to finer fibers as compared

to the subsequent treatment groups. Weekly treatment fibers had Young's modulus values of 1 GPa, at largest, larger than both the control and single fiber treatment groups.

At present, the number of samples in each treatment group limits the reliability of analysis methods, both Weibull and Griffith, to robustly define fiber variability and relationship between the fiber diameter and mechanical properties. With inherently high variability in natural fibers, at a minimum, 50 samples should be tested to ascertain data. Limitations in testing come from limitations in fiber availability and quality fiber due to the number of treated plants in previous studies. Where in field trials thousands of plants may be planted and harvested, in growth chamber that number is limited to on the order of tens, with manual extracting processes less robust than what is available at lab scale. In Appendix B: Growth of CNC Treated Flax Plants on Small-Farm Scale, we will remedy this problem, by obtaining fibers from 1300 plants treated with cellulose nanocrystal in field, from there we will be able to build enough data to determine the underlying variability in data and reliance on fiber diameter.

Chapter 4 Techno-Economic Analysis of Nanocellulose Enrichment of Flax Fibers

4.1 Preface

Flax is one of the world's earliest domesticated crops, which has continued to this century with a fiber flax production of 0.71 million tonnes in the year 2023[53]. This represents a decrease as compared to previous years. While 90% of the world's flax comes from Europe, 75% of which is from France[87], the United States grows flax on 148,000 acres[88]. Flax grown in the United States, primarily in North Dakota and Montana, is for seed production in consumption and oil. Linseed oil, a consumable, has alternate uses in products where petrochemicals may be used.

Fiber flax production in the United States has not bloomed in the same way it has in Europe. In 2003, USDA researchers introduced the idea that flax can be grown as a secondary winter crop for farms in the Southeastern United States[89]. Despite the interest this question poses, economic barriers persist from the introduction of flax into the United States exports. Currently the United States exports grains and seeds as the largest

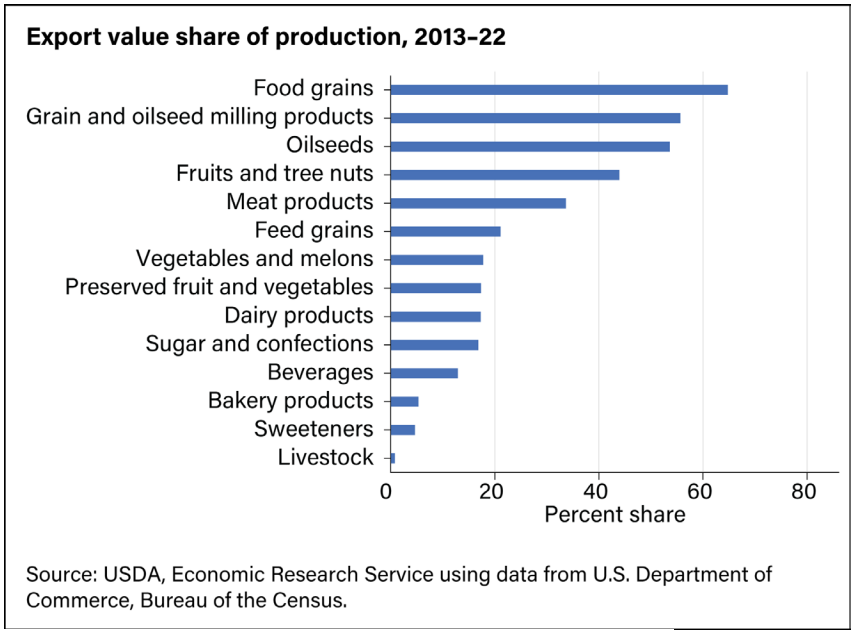


Figure 4-1. Share of US export value as reported by the USDA.

percent share of the market[90]. Southern states that produce large amounts of export products may not be able to sacrifice the income promised by growth of grains with the possibility of income that comes with the growth of flax. Cotton, which the US leads the world in exporting, is another crop that exists heavy along the landscape of the southern United States[91]. Small-scale production of fiber flax in the United States has been largely limited to small farms, fiber sheds, and projects. Coast Fibers (formerly FiberEvolution), PA Flax Project, and AmeriFlax are the largest known flax farms in the United States. PA Flax grows flax on 32 acres[92], whereas cotton is being grown on as much as 1.4 million acres according to the National Cotton Council's planting survey. Incentivizing flax growth in the United States must tie both to an export possibility, a large market, and a financial viability for farms to undertake the task.

Our research in flax fibers for FRC in structural components fits two of these marks. With the use of flax products *outside* of seed, particularly in the automotive industry which motivates many domestic interests, we can motivate farms to observe a possible market—in addition to or besides linen—for them to sell their product. In the same vein, we want to motivate flax farms to apply the technology that we have developed, with cellulose nanocrystal addition in soil, to their fertilizing system. In order to do this, an economic model must be developed to inform farmers of potential gains in this field.

In 2020, The Global CO_2 Initiative built a model for the outdoor, indoor, and hydroponic growth of flax, and the techno-economic cost of managing a farm operating these conditions. From this model, we understand key features of flax farms and products, as well as profits, which may help subsequent farmers understand their undertaking. To further push the boundaries initiated by this

model, we introduce the application of CNC to the field, and the synthesis of CNC from flax chives and short fibers, to this model in order to encourage a sustainable and circular synthesis of enhanced flax fibers from growth to production. A schematic detailing the steps flax farms would apply during this product are detailed in **Figure 4-2**.

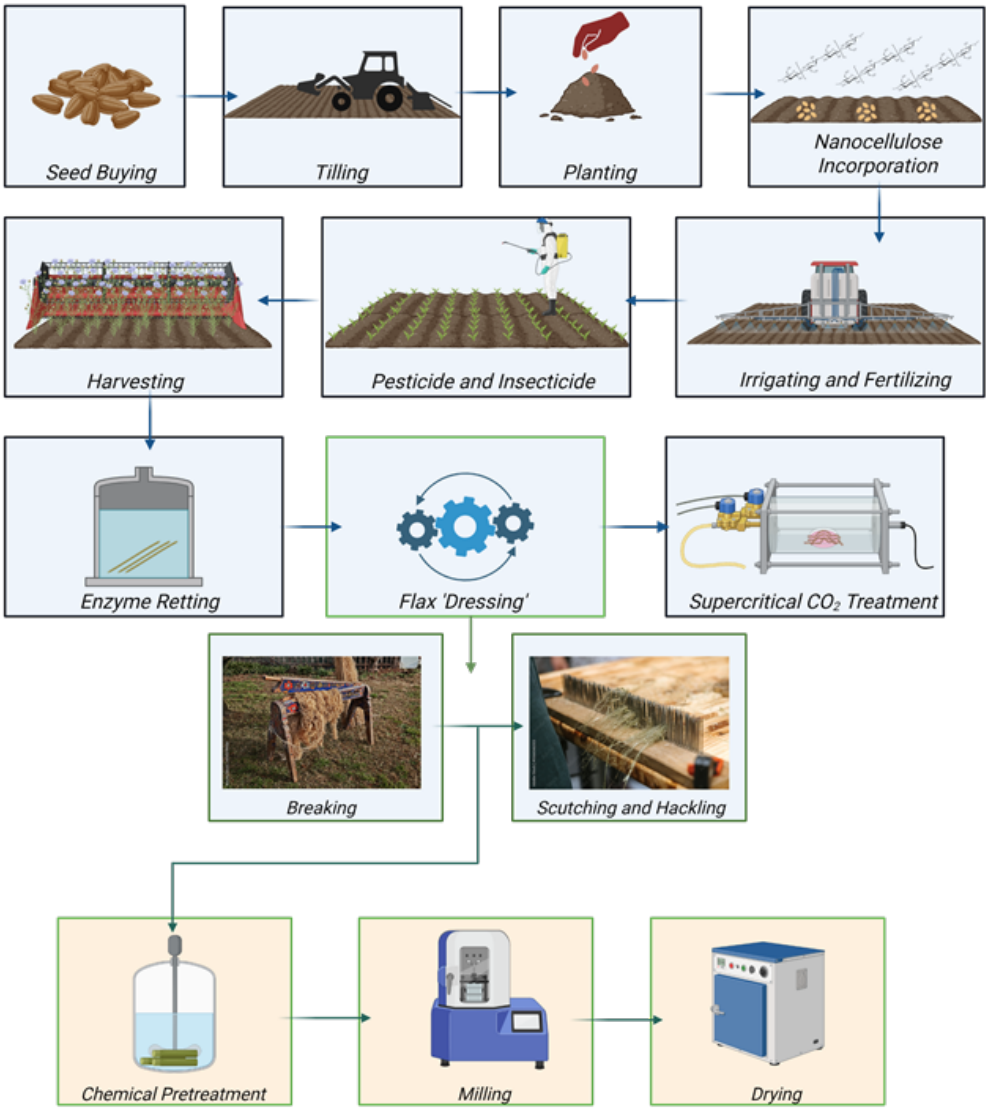


Figure 4-2. Flax circular synthesis flow chart from growth to synthesis of flax-based cellulose nanocrystal.

This chapter details the process for coming that synthesis of cellulose nanocrystal from flax is a possibility, before continuing to analyzing the cost for farms to produce flax, as well as cellulose

nanocrystal modified flax, and whether or not the further synthesis of cellulose nanocrystal is an economically viable addition to the production line.

4.2 Exploratory Synthesis of Cellulose Nanoparticles

Plant biomass can be used to feed back into the growth improvements exhibited in flax by cellulose nanoparticles. An important part of understanding the economic cost-benefit of cellulose nanoparticle feeding is to understand requirements regarding the synthesis of cellulose nanoparticles. Cellulose nanoparticles (crystal and fibril), from plant matter, is derived by cleaving cellulose from sheets to chains, and then further snipping large chains to nanosizes. This can be done by the use of grinders and homogenizers, or by alkali treatment and acid hydrolysis. As Chapter 2 discusses, cellulose nanocrystal demonstrated the largest effect, and thus will serve as the basis for this technoeconomic analysis.

While the process for synthesizing CNC at farm-scale would be different in terms of energy expenditure and machinery, it is helpful to reference the necessary items—scale is an important consideration of this process. To reference, cellulose nanocrystal is typically synthesized from wood pulp—lignocellulosic biomass-- the most abundant plant biomass on earth[93]. While only 70% cellulose (compared to cotton at 97% cellulose)[45], the abundance of woody biomass makes it a cheap and accessible starting material for obtaining cellulose nanocrystal. Using a JEOL IT500 (Peabody, MA) Scanning Electron Microscope at 3 kV, we can observe the crystal cluster morphology for cellulose nanocrystal synthesized from wood pulp (Nanografi, Ankara, Turkiye).

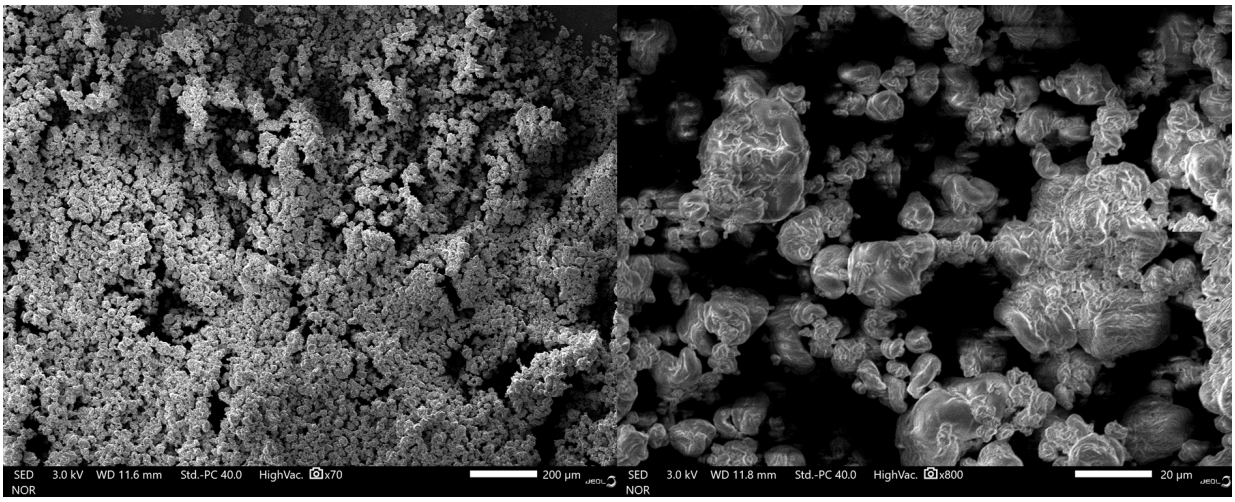


Figure 4-3. Cellulose nanocrystal observed under scanning electron microscope at a.) 200 microns and b.) 20 microns.

To create a financial situation advantageous to flax farms, a circular synthesis mode needs to be successful. As such, Chapter 4.2 explores the possibility of synthesizing a flax based nanocellulose at laboratory scale.

4.2.1 Materials and Methods[22]

7.35 g of dried flax was ground and added to a jar. To a separate jar 10.11 g of dried softwood was ground and added. Grinding was done in a commercial grinder with an amount of liquid nitrogen added to the chamber. 1 L of a 5% NaOH solution was made, and the biomass was fully submerged in the solution. As both the flax and softwood biomass exhibited different hydrophilicity, it was necessary to alter the amount added to each jar. To the jar containing the ground flax biomass, 350 mL added; 250 mL was added to jar with softwood. To ensure the reaction proceeded, the biomass was stirred for four hours. When the biomass resembled more of a pulp, it was filtered with large amounts of DI water, then dried in oven at 80 °C for 24 hours.

A 1:2 ratio of high molarity sulfuric acid to DI water was created, and 300 mL of the solution was added to the dried plant biomass. This biomass, which were dried in their experimental containers, were heated at 40 °C and stirred continuously for two hours. The temperature of the mixture should be monitored using a thermocouple to ensure proper heating. Following heating, the biomass was transferred to new, separate centrifuge vials and washed several times with water adjusted to pH 7 while centrifuging the suspension at 350 RPM for several rounds. CNC was dried in oven at 80 °C, with care not to over dry.

Scanning electron microscopy was used to determine morphology and size of nanocrystal clusters. A JASCO Fourier Transform Infrared Spectrometer (Oklahoma City, OKC, USA) was used to identify characteristic peaks to determine whether nanocellulose was successfully recovered. Flax and softwood derived materials were compared to Nanografi nanocellulose crystals as a control.

4.2.2 Results and Discussion

Softwood derived cellulose nanocrystals tended to stay enmeshed with each other, reflecting heavily the macrostructure of the wood from which it was derived.

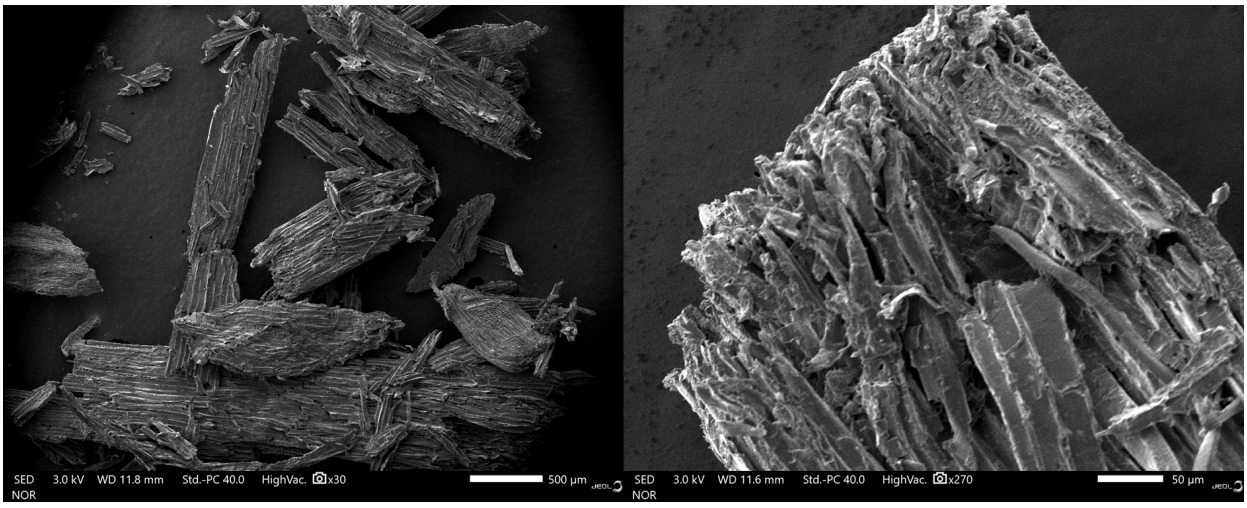


Figure 4-4. Scanning electron micrographs of Softwood-derived synthesized cellulose nanocrystals.

Size of the crystals makes it difficult to determine whether or not they are of nanoscale. It could be concluded that, at the very least, these micrographs indicate the likelihood that a microcrystalline product was synthesized.

To confirm that the product is cellulosic in nature, FTIR was conducted.

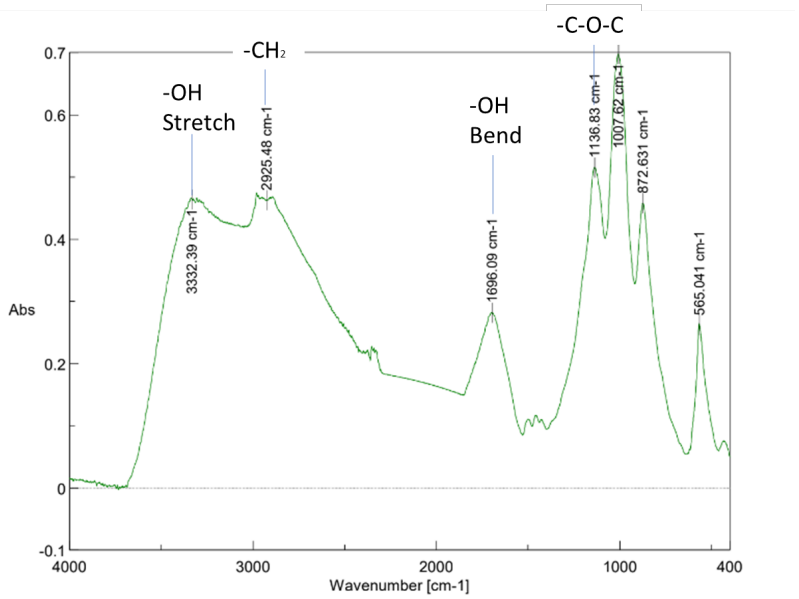


Figure 4-5. Fourier Transform Infrared Spectrograph of Softwood-derived synthesize cellulose nanocrystal.

Figure 2-13 gives us an expected spectrograph for cellulose nanocrystal. OH peaks, CH_2 peaks, and glycosidic bonding peaks confirm that cellulose is present in the molecule. Additional peaks may correspond to -C=O (1007 cm^{-1}) and cylcohexanes (827 cm^{-1}). Carbonates would be present as a reactive intermediate. The FTIR suggests that, while cellulose is present in the spectrum, there may also be the presence of reactive intermediates indicating an incomplete reaction.

In the case of flax derived nanocellulose, scanning electron microscopy micrographs confirm rod-like structures similar to what is reported in the literature for cellulose nanofibrils. SEM, though able to identify micro-size clusters, cannot confirm the presence of nanosized clusters.

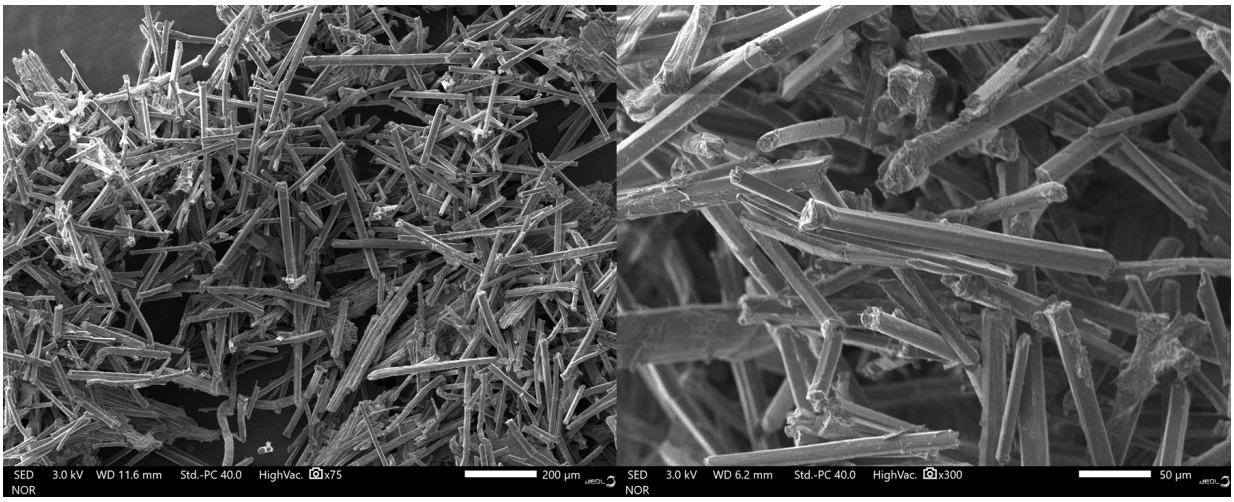


Figure 4-6. Scanning electron micrographs of flax-based cellulose nanocrystals.

Cellulose microfibrils would be the most likely characterization of the resulting product based on the size of the fibrillated clusters. Fourier Transform Infrared Spectroscopy can no better confirm the presence of cellulose than SEM.

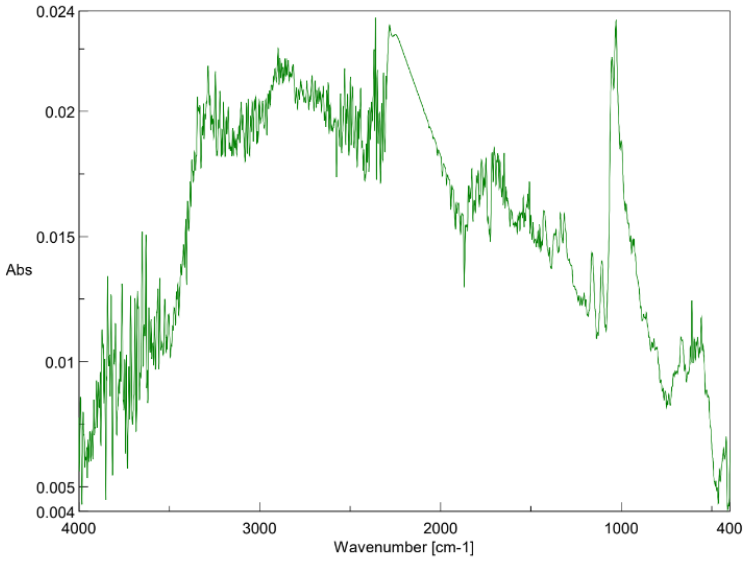


Figure 4-7. Fourier Transform Infrared Spectroscopy for flax-based cellulose nanoparticles.

The indiscernible FTIR spectrograph alters the possibility of properly characterizing the present molecules in the powder. This result could be due to over-drying, which lead to charring of the powder. Improper washing and incomplete retting processes can lead to the presence of multiple compounds such as pectin and waxes, lignin, and hemicelluloses which can vastly affect the clarity of the FTIR spectra. Additional characterization methods are necessary to confirm whether the present compound is, in fact, cellulose nanoparticulate. Confirming complete retting and starting with fiber as opposed to whole stem can better improve the outcome of flax-based cellulose.

These laboratory-scale experiments confirm that small scale cellulosic material can be derived with a combination of alkali treatment, acid treatment, and mechanical agitation. Though this process, which would be a batch process, can be done at small scales, yields of nanocellulose would be vastly improved when dealing with cellulose biomass at farm scale. Economics of scale depend on the cost of batch processing equipment, chemicals, and the potential added cost of placing cellulose nanomaterial on seed. It would be viable, nevertheless, to synthesize nanocellulose from waste flax.

4.3 Results and Methodology for Techno-Economic Analysis

The techno-economic analysis conducted in this chapter builds off of previous research conducted by Grant Faber and the Global CO_2 initiative at the University of Michigan on the economics of flax grown outdoors and via hydroponic growth. Data was updated from their 2020 analysis to reflect values present as of 2025 and 2026. This work is partial, reflecting a localized subset of nanocellulose treatments and conditions based entirely on research conducted in Chapter 2, with the intention to expand as research progresses.

With knowledge of the current process for treatment of flax with nanocellulose, a cost analysis model in which nanocellulose is purchased and a cost analysis model in which nanocellulose was synthesized, circularly, was conducted at a production value of 20,000 bushels/year. This assumed conditions established in Chapter 2, with approximately 0.023 g of cellulose nanocrystal per plant, and 25.7 kg of flax seed per bushel.

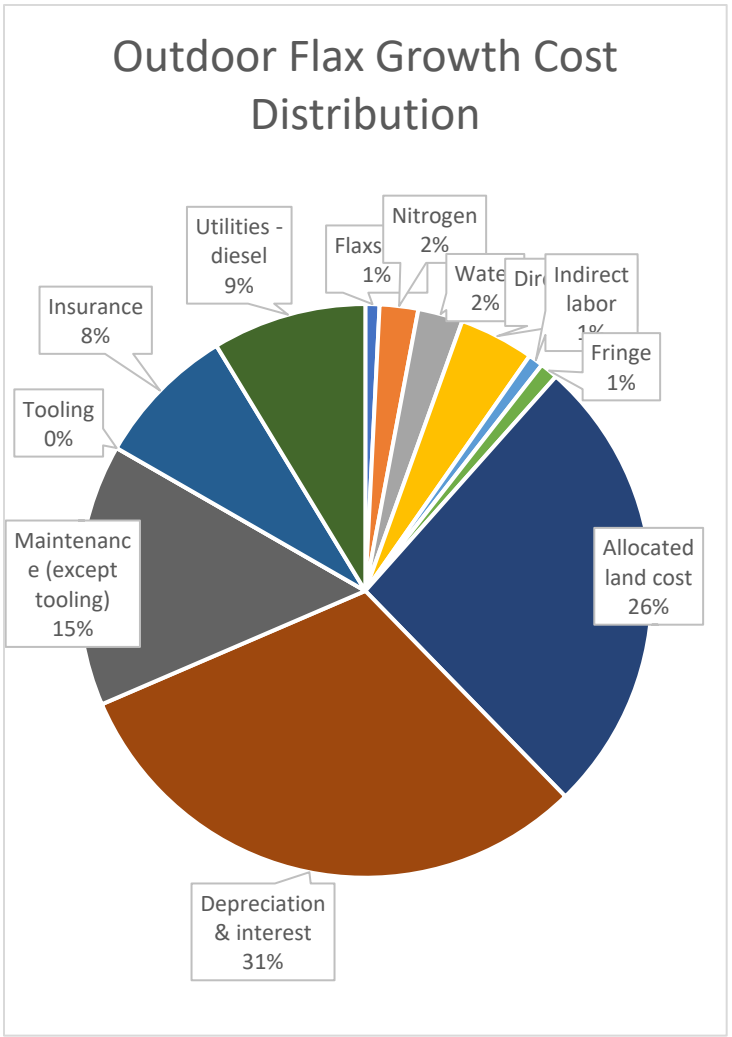


Figure 4-8. Baseline economics of a flax producing farm.

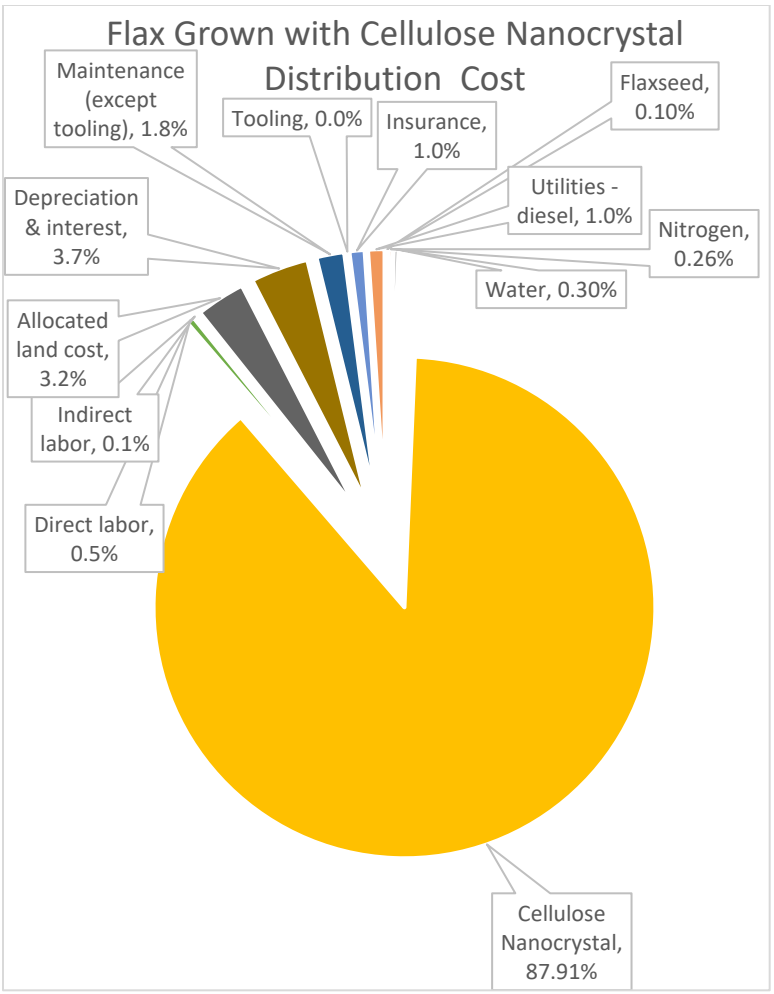


Figure 4-9. Modified economics of a flax producing farm treating plants with crystalline nanocellulose.

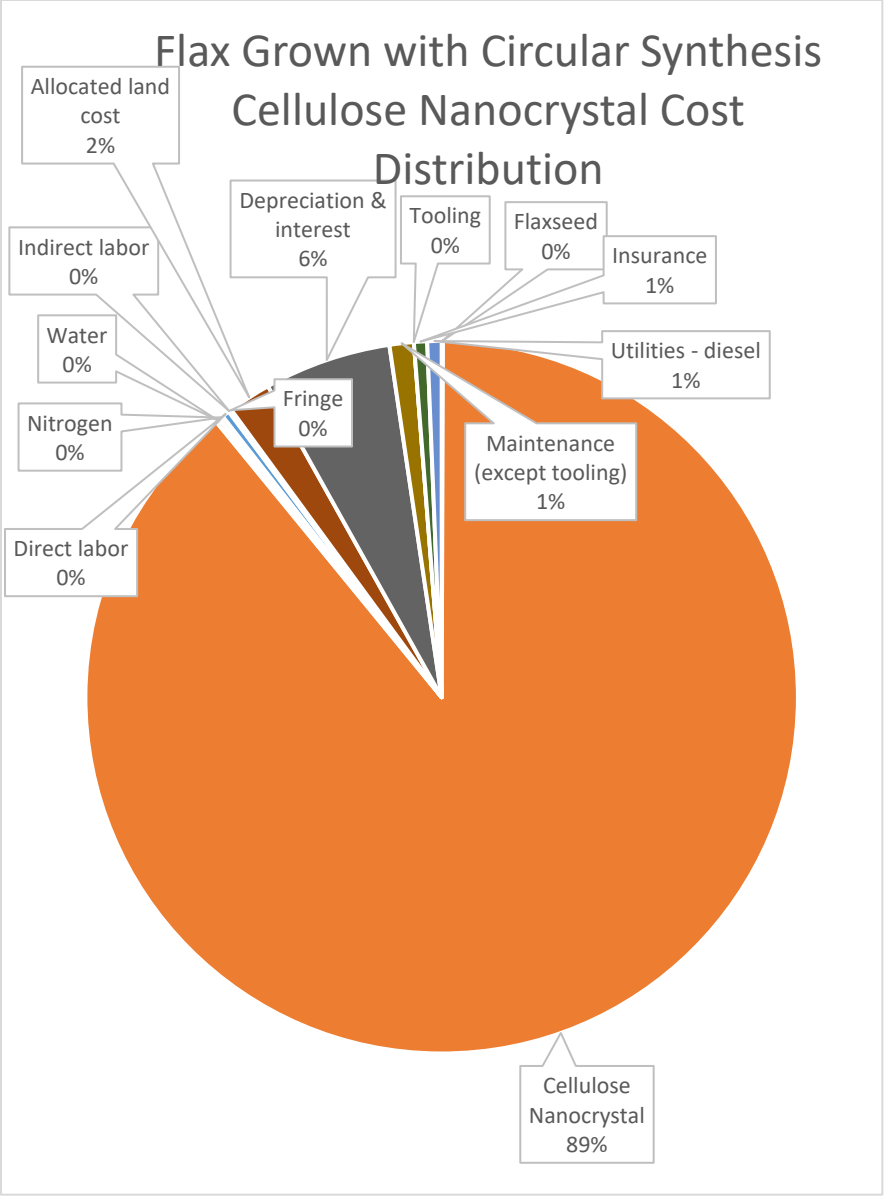


Figure 4-10. Baseline economics of a flax producing farm regenerating crystalline nanocellulose, with which they treat their flax plants.

The predominant cost in this distribution mode is the cost of crystalline nanocellulose addition. At a cost of $750/kg cellulose nanocrystal, the cost of adding nanocellulose to field can incur rapidly at a production volume of 20,000 bushels per year. Similarly, the processing requirements necessary to obtain 20.000 bushels per year of flax and generate cellulose nanocrystal from that waste is large, as defined by **Figure 4-10.** The cost distribution step in the case of synthesized

cellulose nanocrystal is large due to the economics of obtaining necessary equipment—a fixed cost—as well as the variable cost of purchasing chemical treatment materials (sodium hydroxide and sulfuric acid) which vary with production value. This creates a scenario where the treatment of flax waste by chemical pre-treatment to prepare for further refining is the most financially arduous step, this is observed in **Figure 4-11.** At an estimate of 1 L of chemical per 1 kg of biomass, the cost skyrockets at scale.

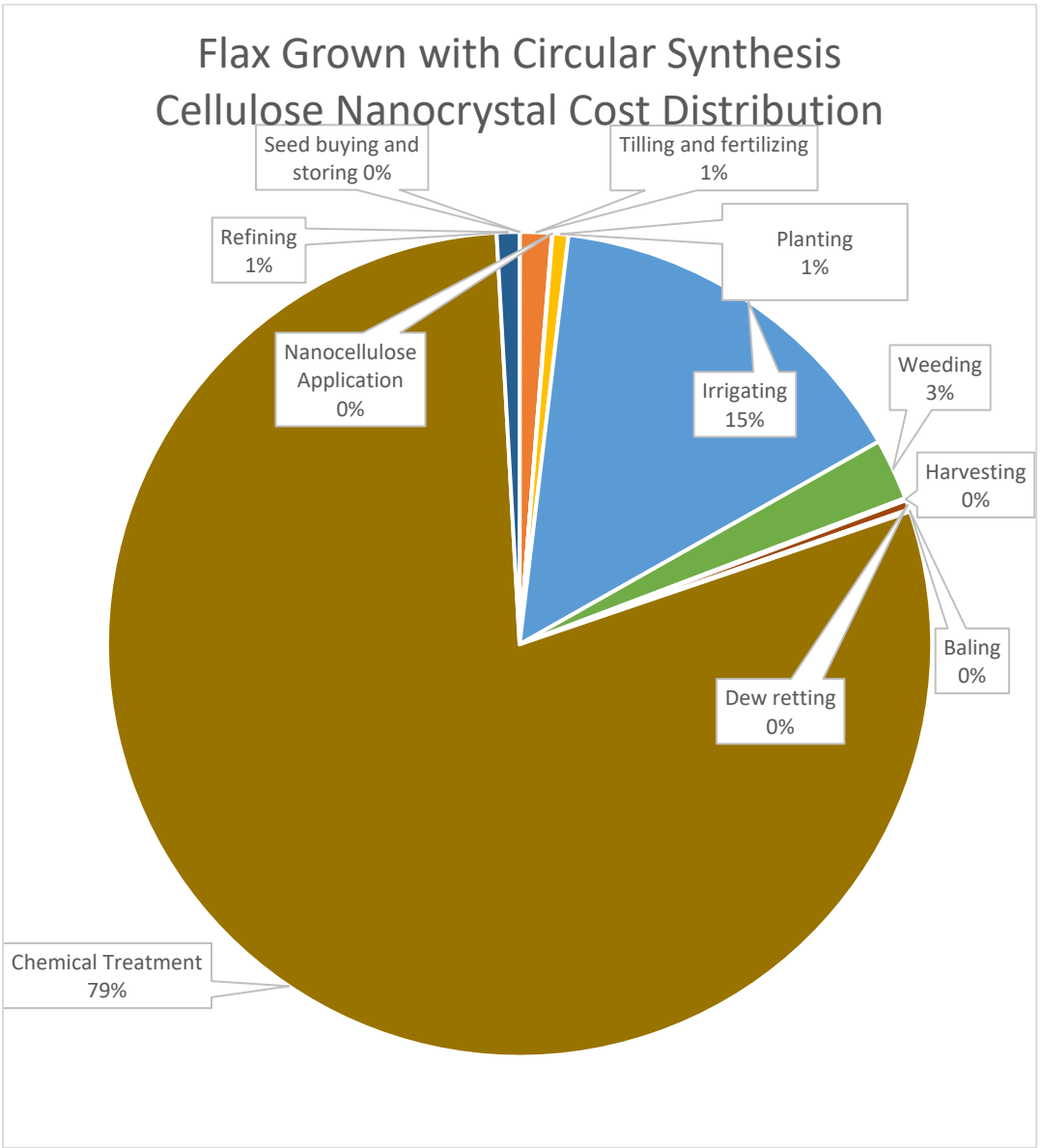


Figure 4-11. Economics of cellulose nanocrystal treatment of flax by process step.

The cost of nanocellulose notwithstanding, the cost distribution of nanocellulose application is similar to the cost of planting or tilling and fertilizing. In the case of synthesized cellulose nanocrystal, obtaining the purest form of the material incurs six times the cost of the second most expensive step, irrigating. Purity is obtained using a combination of mechanical grinding using a disc refiner, and alkali and acid treatment steps. Due to high yields—around 70%, conservatively[94]—and flax waste estimated in the range of 25%[95], we can predict that 2025 kg/year of nanocellulose will be needed to continue operation on a farm set to yield 20,000 bushels per year. For a farm that will produce 3500 kg of cellulose nanocrystal per year (calculated by obtaining 25% of the value of kg/year of flax produced) this leaves the opportunity to sell 1475.94 kg of cellulose nanocrystal at the market price ($750/kg) and earn $1,106,210.57 in profit off of the sales of cellulose nanocrystal. More sophisticated models are needed to disseminate the cost of capital equipment over the life cycle of the flax farm, this will drastically reduce the first-year costs associated with the addition of cellulose nanocrystal to field growth.

When comparing man-hours, cellulose nanocrystal treated nanocellulose experiences fewer additional man-hours as compared to standardly grown outdoor flax, this is observed in **Figure 4-12, Figure 4-13**, and **Figure 4-11**.

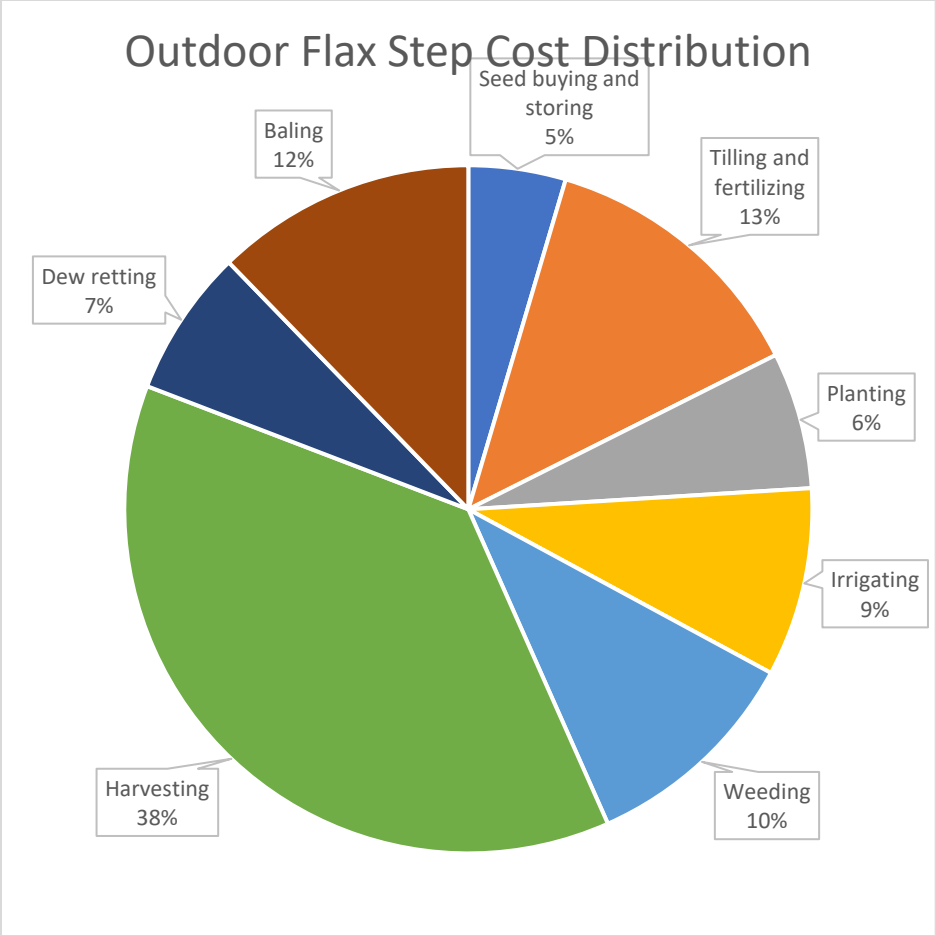


Figure 4-12. Cost of flax production per step.

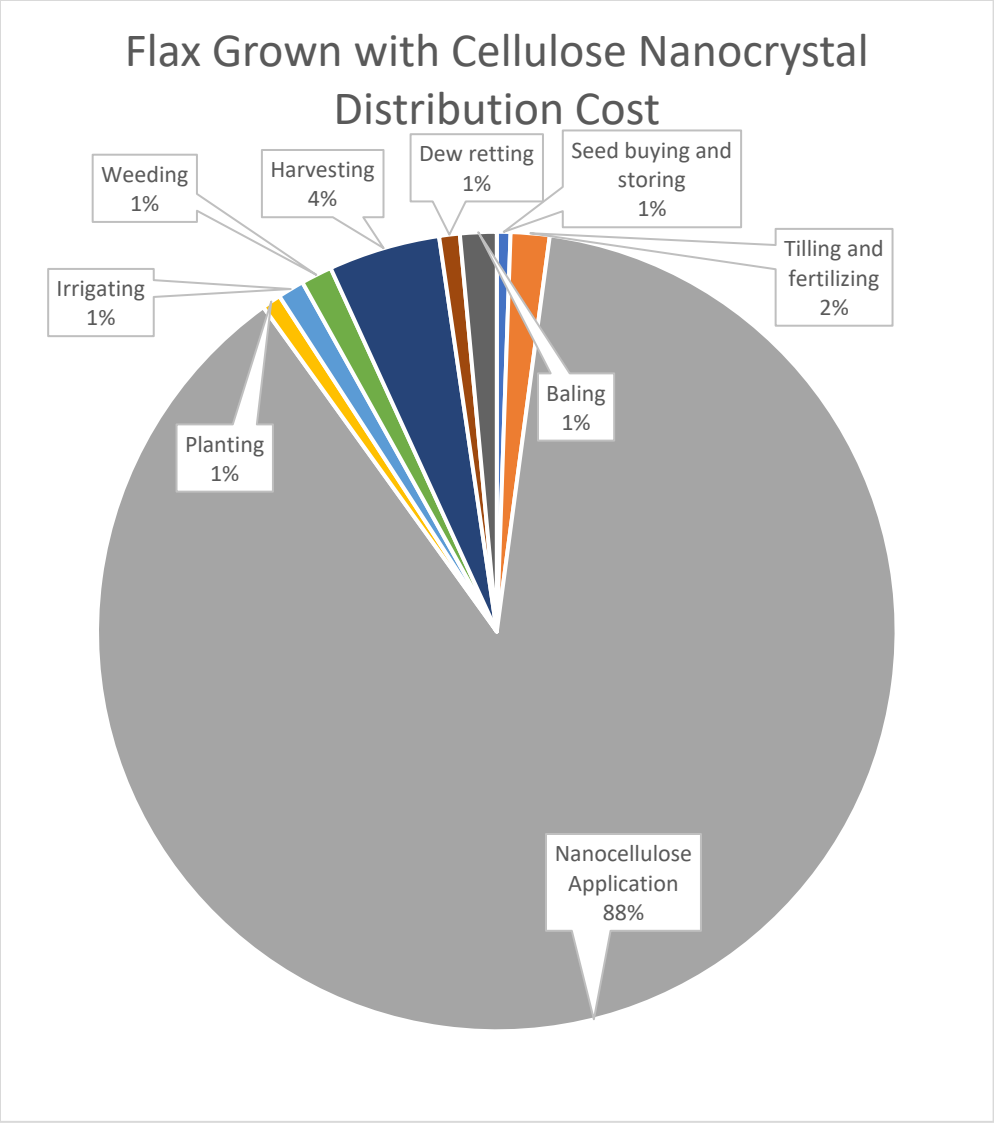


Figure 4-13. Cost of cellulose nanocrystal modified flax production by step.

Outside of the upstart cost of nanocellulose treatment, the application of nanocellulose provides little additional cost. The *costing*, that is purchasing and acquiring, of cellulose nanocrystal proves to be the most cost incurring step. This is because flax farms tend not to have the necessary equipment to purify and obtain cellulose nanocrystal from their flax waste. Purchasing a pasteurizer for chemical treatments, or a disc refiner for mechanical grinding, may put a farm $10,000s behind its production goals after year one. Similarly, the chemical or routine cost of

maintenance pay continually exhaust a farm's resources. Many farms, dairy or wood pulp producing, obtain the necessary equipment to synthesize cellulose nanocrystal for no/lesser start up value than what is exhibited in these models. Additional information is needed to evaluate the financial cost incentive for this symbiotic relationship.

It is important to note that this data was collected without the possibility, due to constraints, to compare the incremental gains as it relates to additional fiber yield per cost of processing. Cellulose nanocrystal experiments exhibited yields that were, on average, 7 cm or larger as compared to the control. Cellulose nanofibril experiments were, on average, 5 cm larger than control plants. Cellulose nanofibril synthesis proves more facile because of the lack of rigor in assembly of crystalline structures—which acid hydrolysis provides. As such, CNF production would prove financially advantageous, though also providing less growth than the CNC treated flax plants. Determining the cost-benefit analysis between a CNC and CNF treated flax farm producing at 20,000 bushels/year, and the incremental fiber yield gained per cm of growth, would educate flax farms on gains obtained by treatment with cellulose nanoparticles.

Furthermore, in the scope of this thesis, analysis of the economics of flax growth is rudimentary. What is needed is a robust analysis of fertilizer technology, start-up cost of a circular economy built around self-sustaining cellulose nanoparticles, and the incremental gains of synthesizing nanocrystal versus nanofibril. As that develops, additional interest should be spent on alternate production values, as well as minimum production values to self-sustain a farm selling both its CNC and flax products at market value. Lastly, long-term operational costs regarding cellulose

nanocrystal production must be investigated to understand how farms may reduce their cost and maximize growth, yield, and profit with the addition of cellulose nanocrystal.

Chapter 5 Pultruded Composites Using Recycled Carbon Fiber and Green Polyurethane

5.1 Introduction

Continuous fiber reinforced composites (FRCs) are used in applications across aerospace, automotive, construction, defense, energy, and high-performance athletics due to their excellent tensile strength and stiffness, low density, and high chemical and thermal stability[96]. Pultrusion is a continuous manufacturing process for rapidly producing constant cross-section FRCs. Unlike extrusion, which pushes material through a die, pultrusion is adapted for continuous fiber parts by pulling fibers through the die in tension after having been exposed to resin. There are two main methods for introducing the fibers and resin during the pultrusion process shown in **Figure 5-2** resin bath and injection box. The resin bath method shown in **Figure 5-2a** which is not suitable for resins with a short pot life, features an open-air bath of resin which the fibers pass through. The injection box method shown in **Figure 5-2b**, which is commonly used with fast-curing resins, delivers resin to carbon fibers in a closed environment directly before entering the heated die. Guide plates and pre-formers are used to ensure fiber alignment and distribution, while a cut off saw works in time with the pullers to automate the process and bring cured parts to the desired size[97]. Pultrusion is capable of producing parts with high fiber loading – typically ranging between 50-75% fiber by volume – primarily by keeping the fibers in tension to ensure unidirectionality and utilizing high pressure to squeeze out excess resin or air[98,99]. Material selection and additional process parameters such as pulling speed and curing temperature(s) contribute to the fiber volume fraction, surface finish, mechanical and chemical properties, and cost of the produced part.

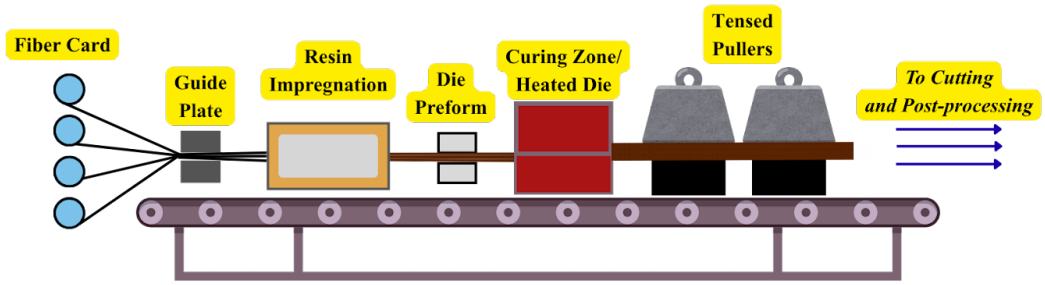


Figure 5-1. Model of a standard pultrustion line for polyurethane resins.

With computational modeling, we are able to estimate and interpret how the curing kinetics of resin systems can be affected by changes in the process parameters for pultrusion[100]. The effects of the heating zone cross-section, temperature(s), pressure, and pulling speed on the final mechanical performance can be understood in part before performing wasteful trials on a physical pultrusion system. However, this digital optimization is reliant on understanding the material properties of both the fiber and resin systems and their interactions together.

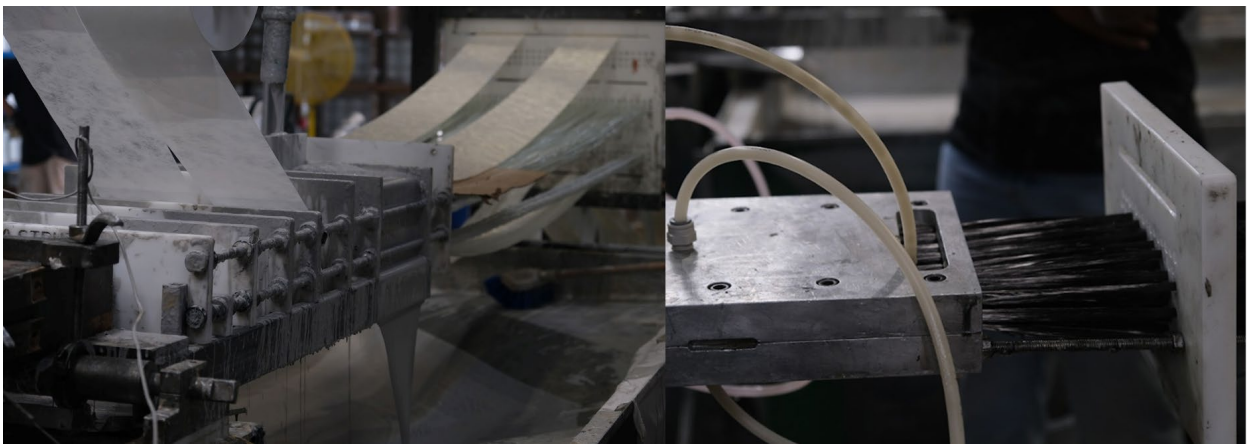


Figure 5-2. Resin bath and resin injection boxes on pultrusion lines.

The production of FRC by pultrusion commonly features glass fiber as the reinforcement material. Carbon fibers are an ideal alternative for the creation of lightweight components due to their high specific mechanical properties, chemical stability, and low thermal expansion. Carbon fibers are

long chains of polymeric carbon materials synthesized from an oxidation-pyrolysis process. Carbon fiber synthesized from polyacrylonitrile (PAN) dominates the market. Synthesis of polyacrylonitrile, however, first requires synthesis of the precursor monomer from propylene – a hydrocarbon known as a combustion byproduct. As such, PAN carbon fiber incurs an environmental cost as a result of its preparation. Successful application of a low-cost PAN carbon fiber from green synthesis or recyclable precursors which performs comparably to state-of-the-art materials would satisfy an important niche for the automotive sector and other industries.

Much interest has been centered around the use or preparation of recycled carbon fiber (rCF). There are three primary recycling methods: mechanical, thermal, and chemical[101,102]. Mechanical fiber recovery, such as crushing and shredding, produces fibers which suffer from surface defects – reducing tensile strength by up to 50% – and are short in length, limiting their applications to resin reinforcement in processes such as injection or compression molding[103]. Thermal recycling methods, such as pyrolysis, utilize high temperatures in an inert environment to decompose cured resin – typically resulting in tensile strength retention of around 80-90%. Finally, chemical methods use strong acids, molten salts, or other solvents to dissolve the polymer matrix with minimal damage to the carbon fibers – allowing for tensile strength retention as high as 99% of that of the virgin carbon fibers. In addition, some chemical recycling methods have shown the remarkable ability to improve the tensile modulus when compared to unrecycled fibers[104,105]. When considering recycling methods suitable for pultrusion, it is essential to use fibers long enough to be spooled on a bobbin to allow for continuous production. Although recycled fibers reduce the amount of carbon fiber waste that can end up in landfills or undergoing pyrolysis at end

of life, it does not alter the synthesis landscape itself; namely, recycled carbon fibers still rely on an oil-based synthesis process and thus are not fully green.

As alternative synthesis pathways for oil-based resins have emerged, a similar effort has been made to find new technologies that allow for the synthesis of carbon fibers from sustainable sources. One such method is the synthesis of carbon fibers from recycled textile materials. Although many textiles – such as nylon, polyester, and aramid – are made from petroleum-based materials, textiles can also be produced from natural plant or animal sources. Common examples of naturally-sourced textiles include: linen from flax, denim from cotton, silk from silkworms, and wool from sheep[106].

Approximately 92 million tons of textile waste is created every year, with nearly 78 million tons entering into landfills or incineration[107]. Textile waste can be divided into pre-consumer and post-consumer. Pre-consumer waste is free of the dyes or processing contaminants which make it more difficult to convert to other materials[108]. More broadly, of the 166 million tonnes of fiber produced every year, 65% of these fibers are synthetic in origin. The synthetic fiber, acrylic, is synthesized from the same source material as PAN carbon fiber[109]. Acrylic and other carbonaceous source textile waste could prove to be an effective, green synthesis method for PAN carbon fibers.

Resin systems for pultrusion are numerous and varied due to the flexibility of the pultrusion process. Typically, resins are preferred which exhibit fast curing speeds at moderate temperatures. Polyester is one of the most widely used resin systems for pultrusion, representing around 75% of the global pultruded composite market[97]. Polyester resin systems allow for resin bath infiltration

due to its moderate pot life and relative insensitivity to atmospheric water; however, polyester poses significant immediate and long-term environmental and health concerns. During curing, polyester resin systems emit an unfavorable odor due to the emission of vaporized styrene[110]. Styrene is a known carcinogen, particularly when in contact with eyes, skin, or inhaled. Long-term exposure, both as a byproduct of pultrusion or as a result of thermal degradation of polyester-matrix composites, could cause severe health complications[111]. Furthermore, the leading method of polyester recycling is pyrolysis, which releases hydrocarbons such as styrene and benzene into the atmosphere. Additional methods such as material transformation (composites to foams, etc.) and chemical recovery (synthesis of butyric acid and benzophenone) perpetuate the presence of styrene or other carcinogens in the environment[112].

Polyurethanes, which can be either thermosetting or thermoplastic, offer an alternative to the problems introduced by polyester. Polyurethane is durable and versatile, and demonstrates good fatigue characteristics and damage resistance[113]. One of the most favorable aspects of polyurethane is that its synthesis can occur from green and recycled materials. While the most popular and well-documented synthesis methods originate from petrochemical sources, polyurethane can be synthesized from vegetable oil, biomass, or even recovered/reclaimed petroleum materials.16 At end of life, polyurethane resins can be successfully recycled by hydrolysis, glycolysis, and other chemical lysis processes[114]. The byproduct of these processes often results in a polyol which can be reused in polyurethane synthesis and functionalized amine groups[114]. Selection of a low-cost, high quality polyurethane from sustainable sources could be essential for the next generation of composite materials for high performance applications in aerospace, automotive, and beyond.

In this work, we present the characterization process and results for recycled carbon fibers and recycled, bio-based polyurethane as individual constituents and in two highly loaded (60 and 74 vol% carbon fiber) FRCs which were produced via pultrusion. These data inform our understanding of the compatibility of sustainable material systems and the effect of the pultrusion process on their mechanical performance, providing a baseline for computational modeling and future optimization of green pultrusion processes.

5.2 Materials and Methods

5.2.1 Interfacial Property Analysis of BASF© Polyurethane and CrossLinks© Carbon Fiber

Recycled, PAN-based carbon fibers were obtained from CrossLinks with a nominal fiber diameter of 6.9 microns and 164k fibers per tow. Fibers were received both as a unidirectional tow and a plain weave mat. The tensile strength and stiffness of the carbon fiber were obtained via single fiber tensile testing according to ISO 11566. Paper frames with 25.4 mm gauge length were laser-cut from card-stock paper. A single carbon fiber was held in place across the paper frame using double-sided carbon tape, and then permanently affixed to it using EPON Resin 862 epoxy with EPIKURE Curing Agent 3230. This system was loaded onto an Instron 68SC-1 with a 1 kN load cell. Once loaded, the sides of the paper frame were cut, and each carbon fiber was extended at a rate of 1 mm/min. The ultimate tensile strength and tensile modulus of elasticity were determined by preparing and analyzing stress-strain curves from the resulting load-displacement data. When determining modulus, a linear regression was performed across the strain range of 0.1 to 0.5% to mitigate the effect of noise. A truncated region was used for two specimens that did not reach 0.5% strain.

A recycled, bio-based, two-part polyurethane system was obtained from BASF for use as the FRC matrix material. The tensile strength and modulus of elasticity were determined via dogbone tensile testing according to ASTM D638. Prior to mixing, 1-part BASF Elastocoat 74850R Resin and 1.37 parts of BASF Elastocoat 74850T Isocyanate were weighed and degassed in a vacuum chamber until bubbling had ceased. The individual components were then removed from the vacuum chamber and mixed by hand until a smooth consistency and uniform color was observed. Constrained by the short pot life of the system, the mixture was degassed until extreme bubbling was minimized and then transferred to a Type I dogbone mold. In an oven pre-heated to 120 °C, the polyurethane dogbones were cured for one hour. Following curing, each dogbone sample was tested in an Instron 3345 Universal Testing machine. Sandpaper was used to internally line the grips in order to avoid slippage during testing. Proper alignment of the dogbones within the apparatus was ensured by measuring and marking the centerpoint prior to insertion, then visually aligning this with the middlepoint of the grips. Following alignment verification, the test was carried out with a crosshead displacement of 1 mm/min. Each trial was run until specimen failure occurred.

5.2.2 Interfacial Property Analysis of the Composite System

To understand the wettability of the fiber-polyurethane system, contact angle measurements using static sessile drop method[115] were performed on both a tow and mat of recycled carbon fibers. A control value was derived from the addition of a droplet of glycerol onto the carbon fiber mat, with experimental values conducted with uncured polyurethane resin on the carbon fiber tow. All measurements were analyzed using ImageJ software (NIH, LOCI, University of Wisconsin).

Effective load transfer for a fibrous composite is governed by the quality of the interfacial bond between its constituents[116]. Poor mechanical or chemical bonding can severely diminish the expected structural performance of a FRC when compared to its ideal rule of mixtures prediction. Thus, single fiber pull-out testing was performed to determine the interfacial shear strength between the rCF-polyurethane system. First, silicone mold negatives were prepared, each featuring a 6 mm cubic void and a slit which was cut roughly 3 mm down one sidewall of each mold. A single carbon fiber was placed between each slit so that it protruded into the cubic void – taking care not to damage the embedded end of the fiber. The fiber was pulled from the free end while being observed in an Olympus DSX510 optical microscope, targeting an embedded length of 90-120 microns. If the embedded length is too high, the fiber may exhibit tensile failure before pull-out; conversely, an embedded length which is too low requires consideration of end effects, which are assumed to be negligible for LeDf10, where Le is the embedded length and Df is the fiber diameter.23 Once the embedded length was set, the cubic voids were filled with the mixed polyurethane system, which was degassed to the extent allowable given the short pot life. Samples were cured at 120 °C for 1 hour, and then carefully removed from the silicone molds. In order to enable adequate gripping during testing, a tab of Scotch tape was affixed to the free end of each fiber with Loctite superglue – leaving approximately 8-12 mm of bare fiber between the embedded end and tabbed free end. Finally, the samples were tested on a Instron 68SC-1 with a 1 kN load cell and a crosshead displacement of 1 mm/min. The interfacial shear strength, τ, can be calculated by the following equation:

$$\tau = \frac{F_{max}}{\pi D_f L_e} \qquad \text{(X)}$$

where $F_{max}$is the maximum force before pull-out.

5.2.3 Pultruded Composite Creation at PulFlex, Inc.

Composite panels were manufactured at PulFlex, Inc. on a custom designed pultruder system. CrossLinks Recycled Carbon Fiber bobbins were loaded on a rack, and their tows were fed through one or more guide plates to ensure even fiber distribution in the die. Both 60% and 74% fiber volume fractions (V_f) were targeted during the four days of production. For the 60% fiber volume fraction composites, 41 carbon fiber tows were strung through one guide plate and loaded into a polymer resin injection box and 127 mm x 3.175 mm die. A Magnum Venus Products (MVP) pump delivered 1 parts of BASF Elastocoat 74850R Resin and 1.38 parts of BASF Elastocoat 74850T Isocyanate to the injection box while in operation, while pre-tensioned pullers maintained a pulling rate of 22 in/min. For the 74% fiber volume fraction composites, 50 carbon fiber tows were strung through two guide plates and fed into the same injection box and die. The MVP pump delivered 1 part BASF Elastocoat 74850R Resin and 1.39 parts of BASF Elastocoat 74850T Isocyanate, and tows were pulled at a speed of 21 in/min. For both volume fractions, three pre-heated zones (Zone 1: 132 °C, Zone 2: 177 °C, and Zone 3: 154 °C) cured the polyurethane matrix as the composites were pulled through the die.

5.2.4 Volume Fraction Confirmation of Pultruded Coupons

The fiber volume fraction of each composite panel was validated experimentally via nitric acid digestion. Samples of both the estimated 60% and 74% carbon fiber composites ranging in size from as large as 70.3x10.7x3.2 mm to as small as 19.45x12.41x3.14 mm were loaded, separately, into a round-bottom flask containing 70% nitric acid heated by an oil bath to a temperature between 60°C and 80 °C, with a condenser feeding cold water attached to the lip of the round-bottom. The temperature of the oil bath was monitored using a thermocouple and maintained via hot plate. Nitric acid denatured the polymer matrix and, by thoroughly dissolving the polyurethane, released the carbon fibers from the matrix. Following the reaction completion, the round bottom flask was

removed from the oil bath and cooled to room temperature, after which the carbon fibers were strained through a PTFE filter and washed thoroughly with deionized water. Fibers were dried at 60 °C in a Lindberg Blue M vacuum oven and weighed on a Sartorius Practum electronic balance with a resolution of 0.1 mg. Using a JEOL IT500 Scanning Electron Microscope (SEM) with an accelerating voltage of 15 kV, cross-sectional samples of the composites were imaged to observe the distribution of polyurethane in the composite to further confirm volume fraction and resin infiltration.

5.2.5 Mechanical Testing of Pultruded Coupons

Composite panels manufactured at Pulflex, Inc. were cut to size using a Milltronics CNC lathe (Indianapolis, IN) in accordance with ASTM standards for flexural testing (ASTM D7264), tensile testing (ASTM D3039), and Izod impact testing (ASTM D256). To conduct three-point and four-point bending tests, samples were loaded in the appropriate fixtures on an Instron 3382A (Norwood, Massachusetts) with a 100 kN load cell. Three-point bend samples had average dimensions of 122.7 x 12.83 x 3.14 mm and were tested at a compression rate of 1 mm/min. Four-point bend samples were subject to the same quasi-static loading, and had average dimensions of 122.6 x 12.98 x 3.14 mm. All flexural samples had the standard span-to-thickness ratio of 32:1, and a sample length roughly 20% longer than the span. The composite's flexural stiffness was of primary interest, so samples were not intentionally tested to failure; rather, each test lasted for a maximum of 5 minutes (i.e. a total crosshead displacement of 5 mm). For four-point bending, the crosshead displacement does not equal the maximum displacement (max) of the specimen – which occurs at the mid-point of the span. To account for this, a scaling factor was defined based on beam deflection tables for a simply supported beam with 2 equal loads spaced evenly from the supports, as follows:

$$\frac{\delta_{max}}{\delta} = \frac{\frac{FL}{96EI}(\frac{L^2}{4} - 3L^2)}{\frac{FL}{24EI}(\frac{L^2}{4} - \frac{3}{4}L^2)} = 1.375 \qquad \text{(XI)}$$

where F is the force applied by each upper loading nose, L is the span length, E is the modulus of elasticity, and I is the area moment of inertia. Stress () and strain () were then computed from force-displacement data according to the equations in [Table #], where w is the width and t is the thickness of each specimen. Finally, the flexural modulus was calculated by taking the slope of the stress-strain curve in the strain range between 0.1 and 0.3%. A truncated region was used for two specimens that did not reach 0.3% strain.

Table 5-1. Stress and strain equations for three and four-point bending based on ASTM D7264.

	Three-point Bend	**Four-point Bend**
Stress,	$\frac{3FL}{2wt^2}$	$\frac{3FL}{4wt^2}$
Strain,	$\frac{6\delta t}{L^2}$	$\frac{48\delta t}{11L^2}$

Tensile testing samples with cross-sectional areas averaging at 45.9 ± 0.003 mm2 were extended at a rate of 1 mm/min on an Instron 3382A-100 kN load cell (Norwood, Massachusetts). Aluminum tabs 15 mm in width and 60 mm in length were adhered using high shear epoxy, Epon828 (Houston, Texas), to the ends of the tensile samples to improve surface contact and reduce slipping between the machine grips and the composite.

V-notched pultruded composite specimens were securely mounted in the fixture of a Tinius Olsen Model IT504 pendulum impact tester (Philadelphia, PA) in a vertical cantilever configuration, with the notched region facing the striking direction. The specimen was firmly clamped at one end to prevent movement during testing. Impact loading of 23.43 J was then applied by the compound

pendulum, which struck the specimen above the notch to initiate fracture. The absorbed impact energy was recorded and used to evaluate the notch sensitivity and impact resistance of the pultruded composite specimen.

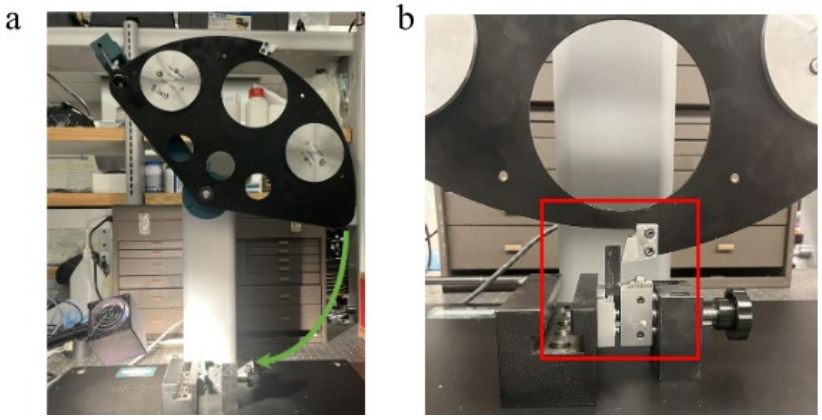


Figure 5-3. Izod impact test experimental setup

Furthermore, the Izod pendulum impact testing for the 60% and 74% v-notched samples were conducted in accordance with ASTM D256-24 Test Method A (cantilever beam test). Specimens measuring approximately 3.17 mm in width and 12.6 mm in depth under the notch were positioned so that the pendulum struck the notched face 22.00 ± 0.05 mm above the clamp, with the notched face oriented toward the pendulum to concentrate stress at the notch root and promote fracture initiation. The pendulum was released from a drop height of 635.73 mm, producing an impact velocity of 3.53 m/s consistent with the 3.50 m/s specified by D256-24. A pendulum capacity of 23.43 J was selected as the lightest available that was expected to fully break each specimen, while still retaining enough energy to maintain consistent striker speed throughout the impact, as required by D256-24. Absorbed break energy was corrected for windage and friction losses, then divided by specimen width to yield impact resistance (J/m), and further divided by depth under the notch to determine the impact strength (kJ/m^2). The failure mode was recorded per D256-24

classifications as Complete Break (C), Hinge Break (H), Partial Break (P), and Non-Break (NB), with non-break failure excluded from data analysis.

5.3 Results and Discussion

Contact angle measurements were conducted to confirm the wettability of the recycled carbon fiber tow with polyurethane. To establish a control baseline expectation for non-wetting, a droplet of glycerol was added to a woven mat of carbon fiber.

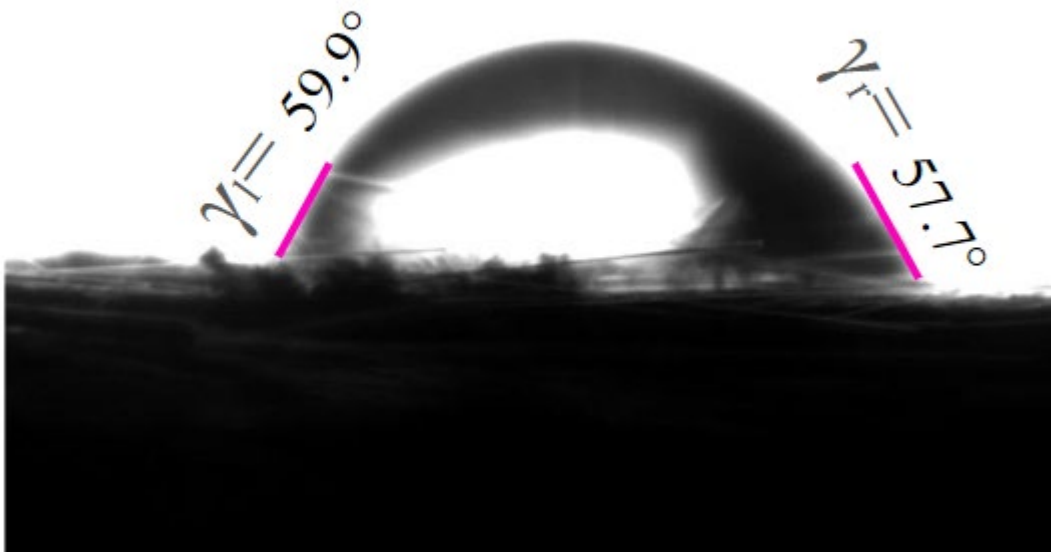


Figure 5-4. Contact angle measurement for a droplet of glycerol on woven carbon fiber.

Contact angles for the control experiment measured at γ_l= 59.9° and γ_r= 57.7° for the tangent angle confirming unideal wetting between the woven carbon fiber and the glycerol droplet. To a tow of carbon fiber, uncured bio-based polyurethane was added. Contact angle measurements were collected at γ_l= 16.1° and γ_r= 19.2° for the respective sides.

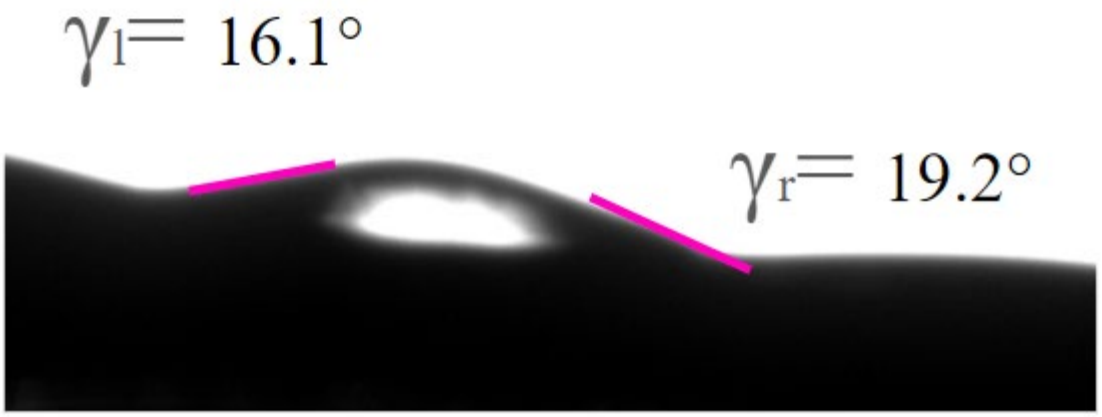


Figure 5-5. Contact angle measurement of a drop of bio-based polyurethane on a carbon fiber tow.

The angle of the tangent line at the droplet contact point is less than that of its component parts. This strongly suggests that a drop of polyurethane resin would be able to wet a carbon fiber tow[117].

Assembling information about the baseline properties of these novel materials is essential to confirming the success of a pultruded composite. Single fiber tensile testing was conducted on CrossLink Carbon Fibers. The cumulative results are shown in the below figure.

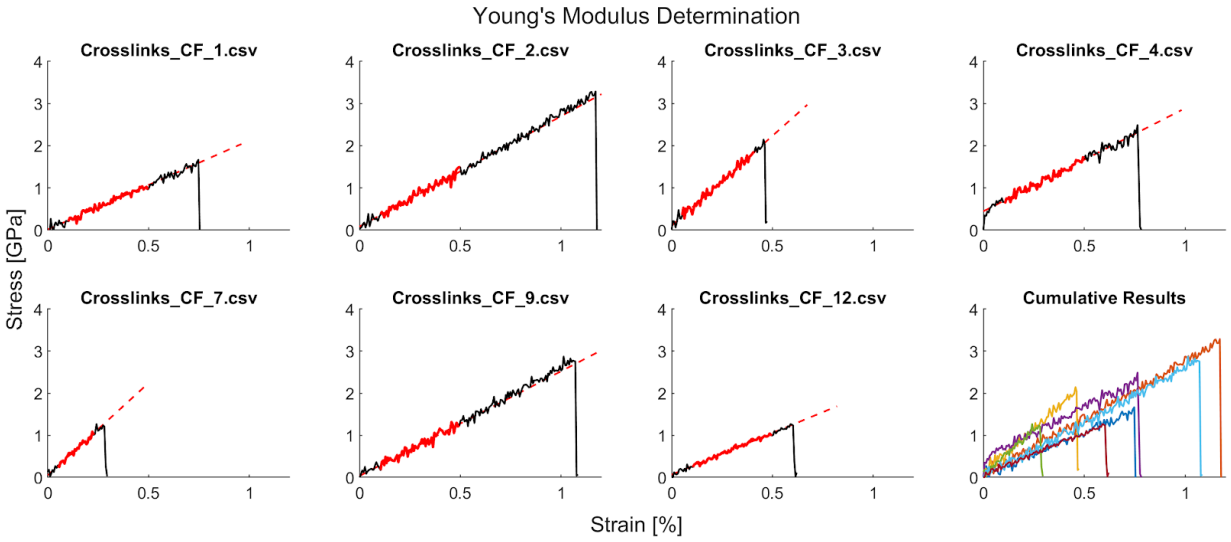


Figure 5-6. Stress-strain curves for single carbon fibers tested on paper frames.

Tensile modulus values were calculated to be 289.9 ± 99.9 GPa with ultimate tensile strength placed at 2.14 ± 0.79 GPa. A wide range of single fiber tensile strength and modulus. This variation can be due, in part, to the nature of the synthesis of these carbon fibers. Waste textiles may have vastly different origins, wear, and may necessitate different breakdown processes which would vastly affect the quality of an individual fiber. Single fiber tensile data places the CrossLinks Recycled Carbon Fiber on the low-end of the expected range for strength and modulus of a recycled carbon fiber[104].

Two polyurethane dogbone samples were tested to obtain tensile information on the matrix. Additional samples were attempted however, difficulties were encountered. The hygroscopicness of the polyurethane at standard temperature and pressure created difficulties in creating samples. A quick cure time of 17 minutes prevented adequate degassing from occurring and, while vacuum cure was possible, the polyurethane tended to cure as trapped air was pulled to the surface. This

led to samples that had pores both large in size and in numeration. To obtain more accurate tensile strength and modulus values, only samples that exhibited consistent clarity were tested.

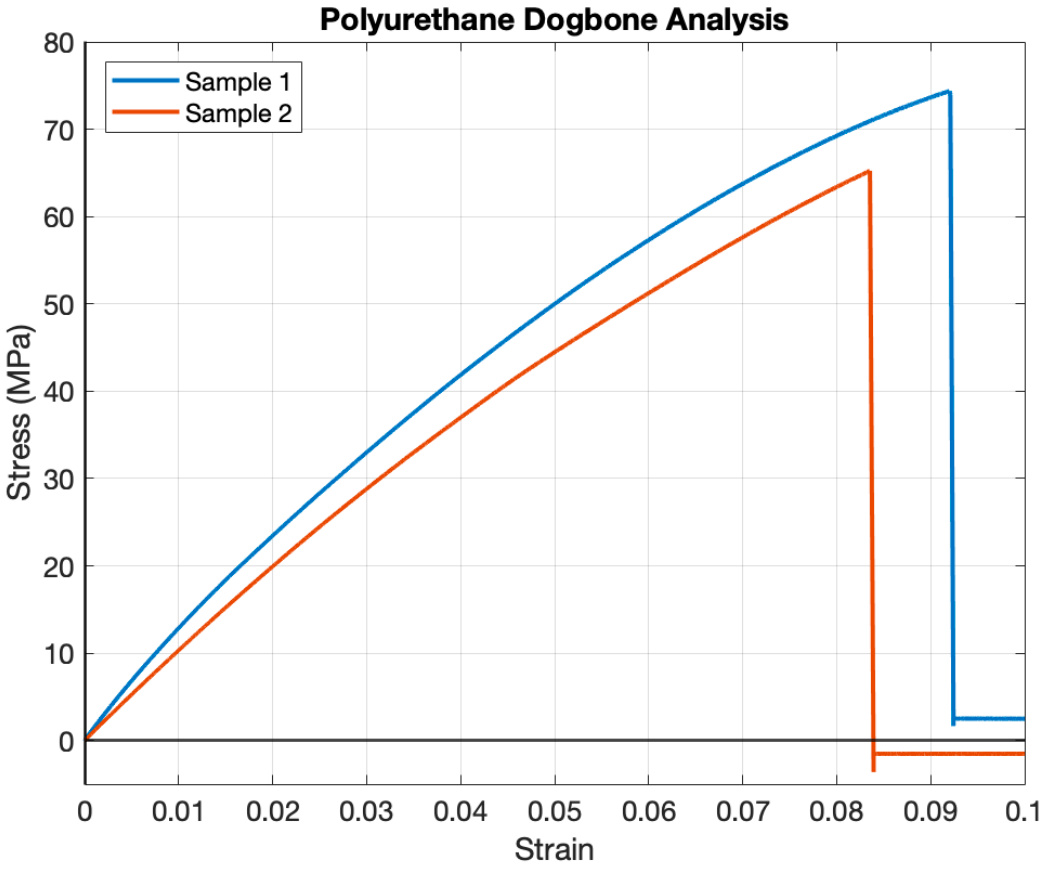


Figure 5-7. Stress-strain curve for polyurethane dogbone samples.

Samples 1 and 2 exhibited brittle failure occurred at displacements of 3.68 mm and 3.34 mm, corresponding to strains of 0.092 and 0.084, respectively. Tensile modulus values were calculated to be 803.59 MPa and 776.67 MPa with ultimate tensile strength calculated as 73.93 MPa and 65.24 MPa, respectively. Polyurethanes, particularly bio-based polyurethanes, have demonstrated a wide range of tensile strength and modulus values, with tensile modulus values reported as low as 1 MPa to as high as 1350 MPa[118]. The BASF polyurethane system is well within the range for bio-based polyurethanes.

Scanning electron microscopy confirmed fibers were indeed embedded in the matrix, and also provided information about the nature of wetting in the composite. Rings of darkness surrounding the carbon fiber indicates a lack of wetting, in places, between the carbon fiber and the polyurethane. Additional information regarding the presence and nature of the sizing on the carbon fiber would be helpful to improve the wetting.

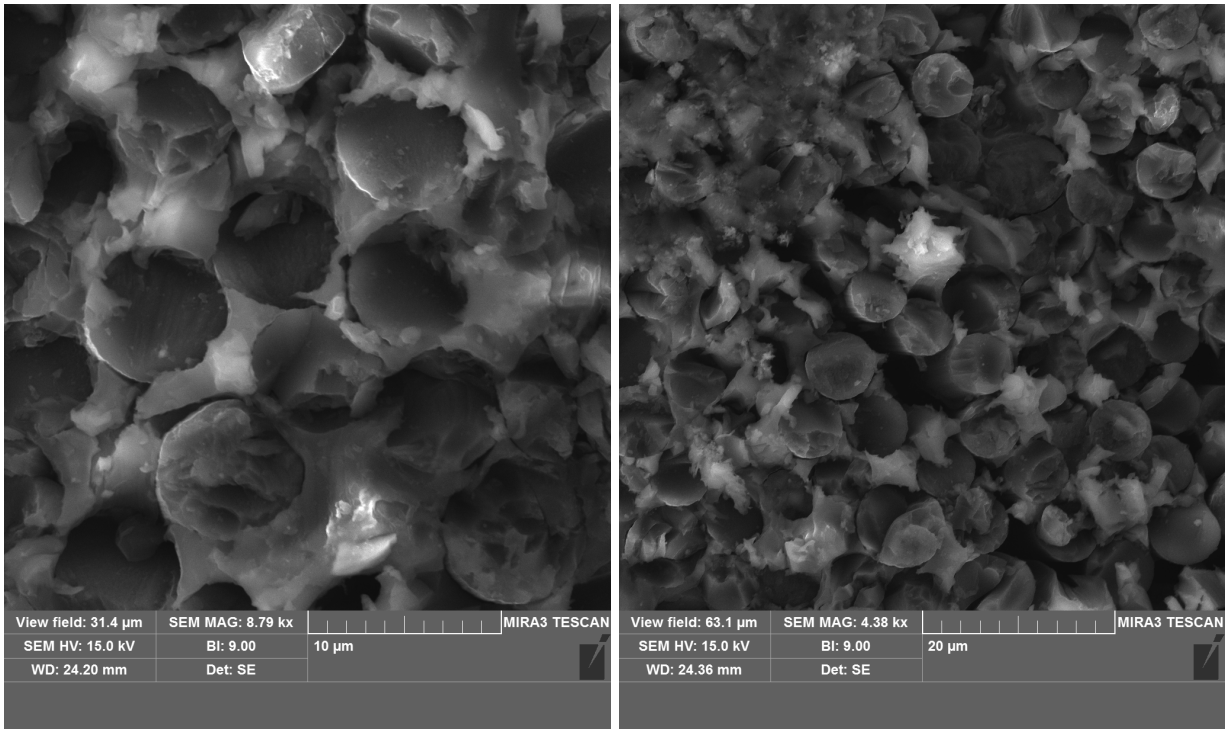


Figure 5-8. Scanning electron microscopy imaging for a cross-section of a 74% volume fraction composite sample.

SEM images can also be used to predict composite volume fraction, which was further investigated. Fraying in carbon fiber tows during the pultrusion process introduced the necessity to confirm fiber volume fraction before analyzing composite properties. The results are shown in the subsequent table.

Table 5-2. Volume fraction measurements for pultruded coupons.

Expected V_f	***Actual*** V_f	***Percent Error***
60%	63%	5.06%
60%	63.6%	5.94%
60%	49.5%	17.6%
$60_{average}$	**58.70%**	**2.17%**
74%	68%	7.67%
74%	75%	1.60%
$74_{average}$	**71.75%**	**3.04%**

As mentioned, fraying of fibers was observed during the pultrusion process. Manufactured tows round around the bobbins exhibited inconsistencies both in fiber size (as observed in the SEM image) and the number of fibers per tow. A volume fraction estimate was made with an expected fiber size in mind, with the additional assumption that all fiber strung through the card wound up in the composite.

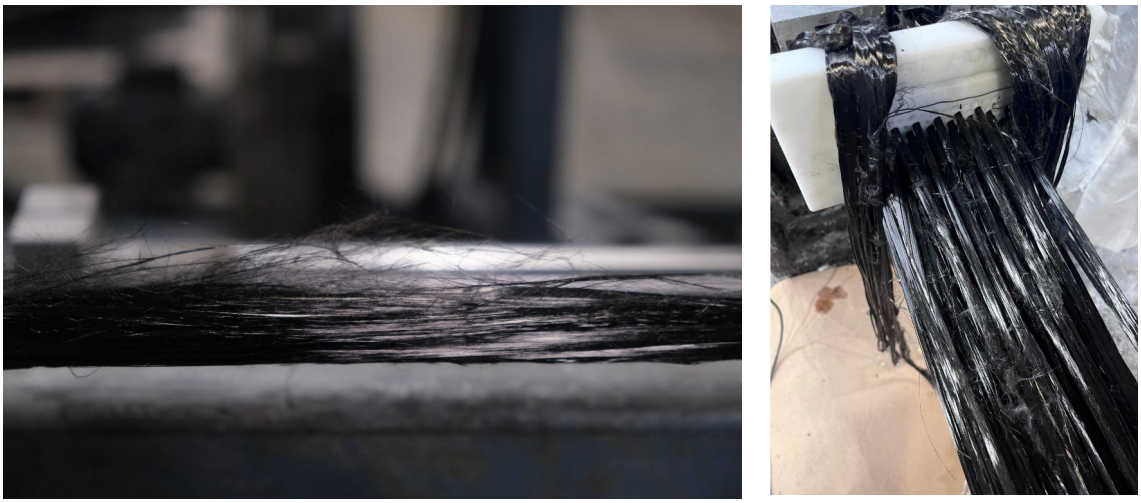


Figure 5-9. Fraying of CrossLink carbon fiber during the pultrusion process.

As the pultrusion process continued, fewer fibers were pulled into the composite as they frayed or caught in the card. This altered the volume fraction of composite coupons pultruded early in the line as opposed to late.

With the knowledge of composite volume fraction, matrix tensile information, and fiber tensile information, we are able to use the Rule of Mixtures to predict the young's modulus of the composite. This is given by the following equation:

$$YM_{composite} = YM_{CF}\left(V_f\right) + YM_{PU}(1 - V_f) \qquad \text{(XII)}$$

Where the BASF polyurethane system showed an average YM_{PU} of 0.790 GPa and CrossLinks YM_{CF} is calculated at 289.9 GPa.

For the estimated 74% volume fraction composite, the tensile strength was found to be 465.5 ± 30.6 GPa and modulus to be 133.9 ± 17.4 GPa

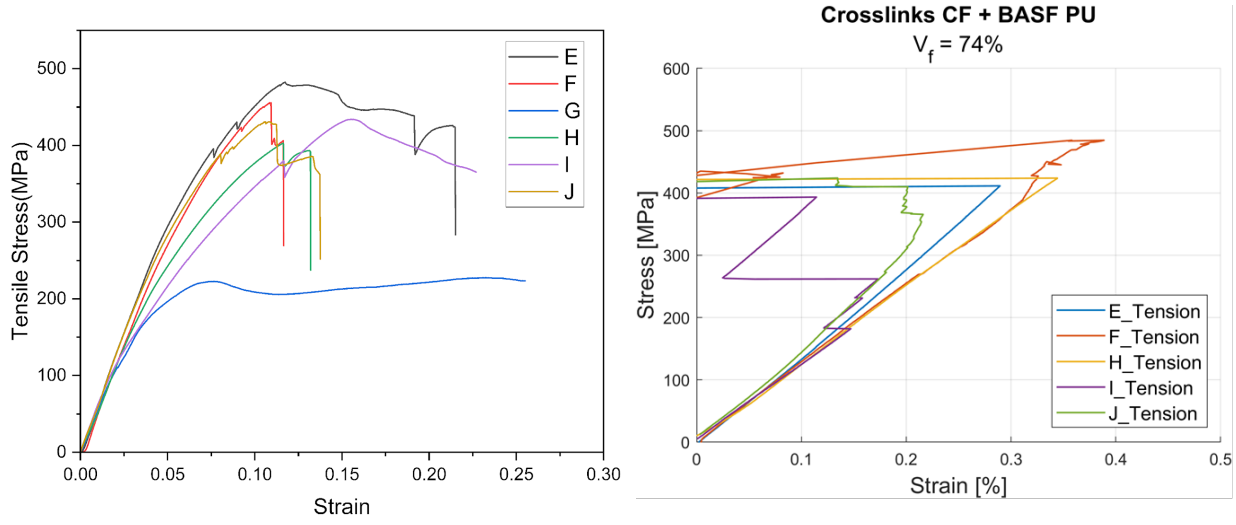


Figure 5-10. Stress-strain tensile data for the 74% volume fraction using an extensometer, and from the cross-head displacement.

Using the rule of mixtures, with the average calculated volume fraction of 71.75%, the theoretical modulus was calculated at 208.23 GPa. The calculated modulus value is 43.45% different from the theoretical value calculated using the average volume fraction.

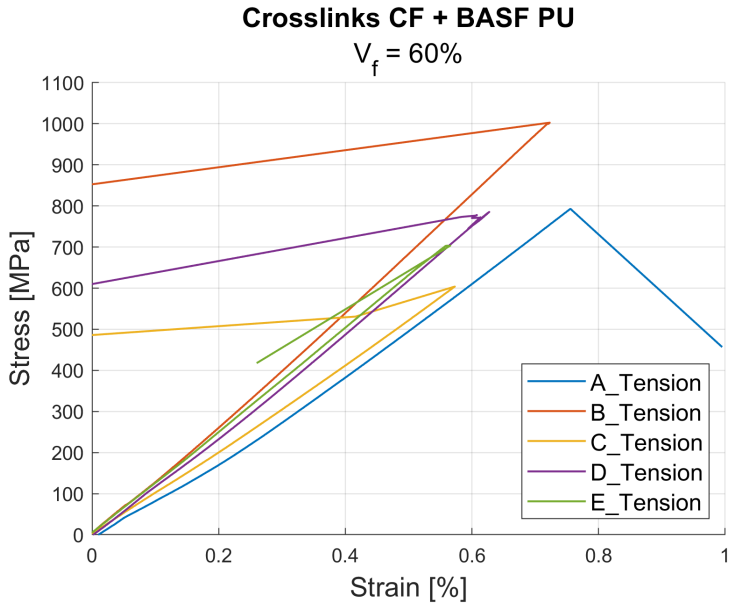


Figure 5-11. Tensile stress-strain curve for the 60% volume fraction using an extensometer.

In the case of the 60% volume fraction composite, tensile modulus was recorded to be 115.1 ± 16.6 GPa, with ultimate tensile strength recorded at 777.7 ± 147.2 GPa. For a calculated volume fraction of 58.70%, the theoretical modulus for the volume fraction was 170.50 GPa. The percent difference between the theoretical and calculated modulus values was 38.80%. Differences between the theoretical and calculated values is due, in part, to variability in the volume fraction which may be vastly different in the tested samples than the experimental samples used to calculate volume fraction. Additionally, non-wetting in the tensile samples may also be a cause for low experimental strength and modulus. Samples that failed along the matrix, as opposed to in tension, contributed to overall lower values.



Figure 5-12. Tensile samples following testing. Failure occurs between the fibers and matrix.

Flexural testing to determine the stiffness of the composites under load were calculated. Samples exhibited greater success in failing with the composite as opposed to with the matrix.

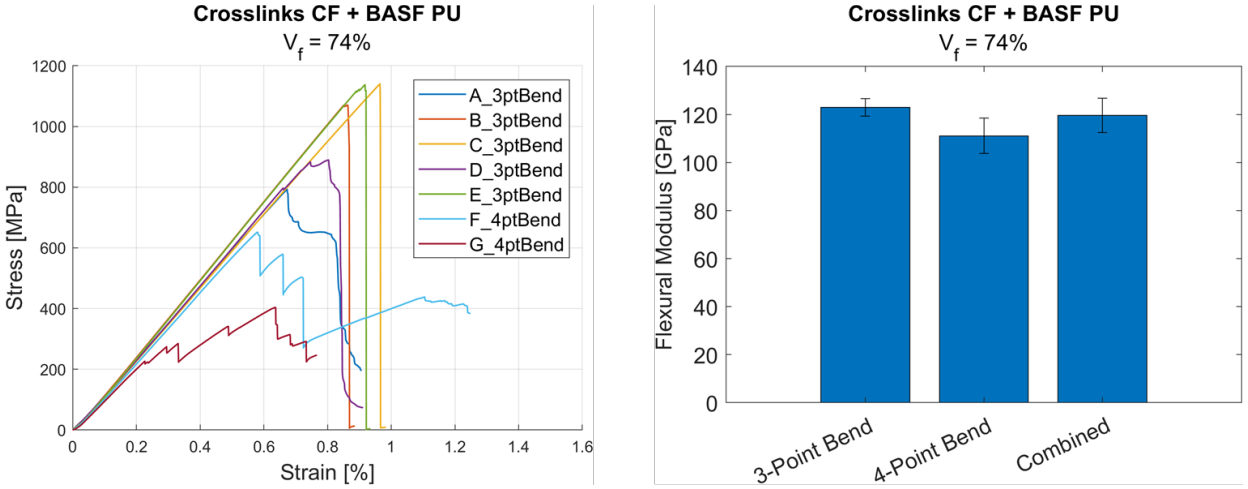


Figure 5-13. Stress-strain curve from flexural testing for the 74% volume fraction composite.

Three, and four-point, bend tests were conducted. Modulus values for the 74% volume fraction composite were reported as 123.0 ± 3.7 GPa for three point, 111.1 ± 7.3 GPa for four point, and a combined modulus of 119.6 ± 7.2 GPa. 60% volume fraction exhibited slightly higher values with three-point modulus values of 122.23 ± 3.2 GPa, four point modulus values of 121.66 ± 9.6 GPa, and a combined modulus of 121.9 ± 7.1 GPa.

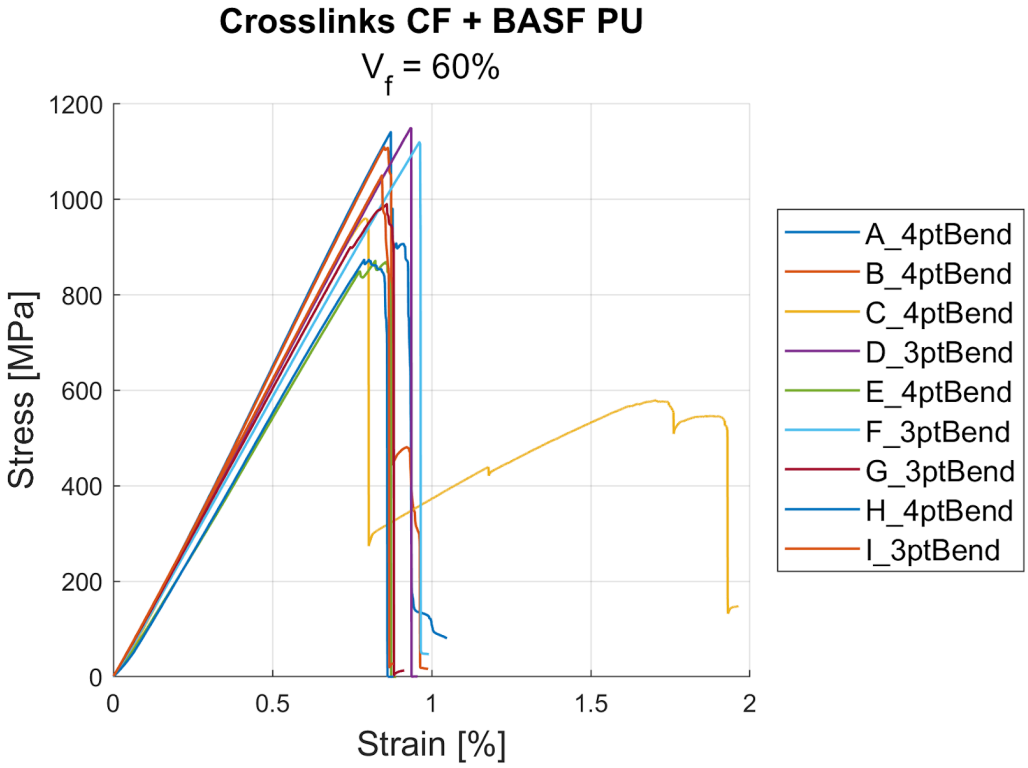


Figure 5-14. Stress-strain curve for flexural testing of the 60% volume fraction composite samples.

60% volume fraction composites may have improved wetting and, due to lower loadings, may experience fewer defects in the composite as a result of processing issues. Flexural modulus shows that composite stiffness may be better than what tensile testing suggests, however fiber wetting and fiber-matrix relationship continues to be an issue for the composite.

Representative post-impact specimens from both fiber volume fractions are shown in **Figure 5-15**. The 60% CF specimen exhibits a complete break failure, in which the sample has fully separated into two pieces at the notch. In contrast, the 74% CF specimen exhibits a hinge break failure, where fracture initiates at the notch but the two halves remain connected by a thin, plastically deformed ligament. These images illustrate the qualitative difference in fracture behavior between the 60% and 74% CF composites that is reflected throughout the impact data discussed below.

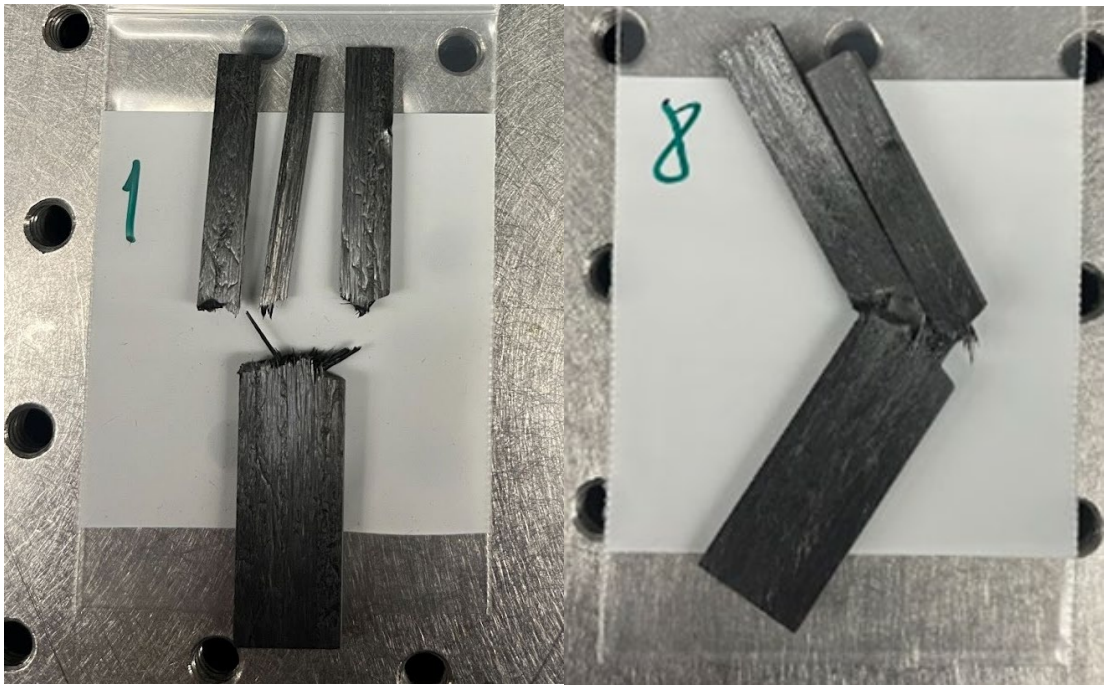


Figure 5-15. Izod impact failure of carbon fiber composite samples: (a) 60% and (b) 74%

The two fiber VF composites exhibited fundamentally different failure behavior under Izod impact loading represented in **Figure 5-16**. The 60% CF composites failed almost exclusively via Complete Break, with 13 of 14 valid specimens (93%) fracturing completely through. In contrast, the 74% CF composites failed predominantly via Hinge Break, with 7 of 9 valid specimens (78%) exhibiting only partial fracture. This inversion in failure mode between the two composites suggests that increasing fiber volume fraction from 60% to 74% meaningfully alters the fracture mechanics of the composite. The higher fiber loading in the 74% CF system likely promotes more constrained crack propagation. Per ASTM D256-24[24], complete break and hinge break specimens are treated differently in computing impact resistance, and this difference in failure mode distribution must be considered when comparing the 60% and 74% CF composites.

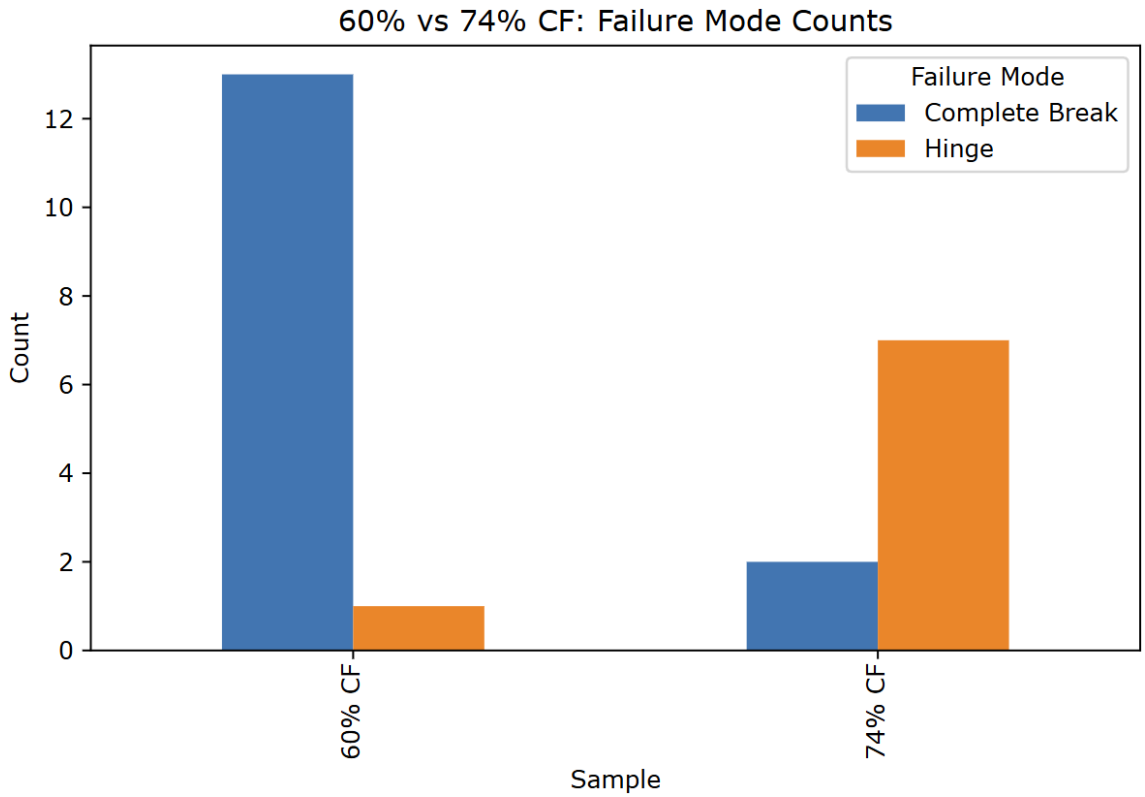


Figure 5-16. Izod impact failure mode counts for 60% and 74% carbon fiber samples.

Mean impact resistance values were similar between the two VF composites, with the 74% CF composites yielding a mean of 2,619 J/m and the 60% CF composites yielding a mean of 2,683 J/m. However, the 60% CF composites exhibited substantially greater variability, with extreme values ranging from 1,350 to 4,000 J/m compared to the narrower 2,450–2,800 J/m interquartile range of the 74% CF composites. The impact strength values followed these trends, with comparable means of approximately 263 kJ/m² and 266 kJ/m² for the 74% and 60% CF composites respectively, but with the 60% CF group again spanning a much wider range of roughly 135 to 400 kJ/m². This greater scatter in the 60% CF group is consistent with its predominantly complete break failure mode, where full specimen fracture is more sensitive to local defects such as voids, whereas the distribution of the 74% CF composites likely reflects a fracture response governed more uniformly due to the dense fiber network.

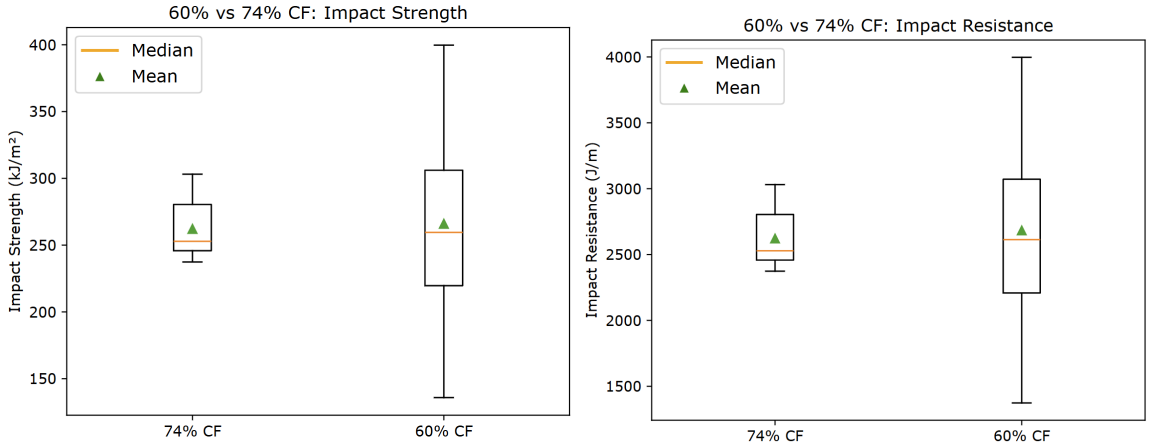


Figure 5-17. (a) 60% and 74% CF impact resistance, (b) 60% and 74% CF impact strength

Figure 5-18 presents the empirical cumulative distribution functions (ECDFs) for impact resistance of both composite systems. The ECDF plots the fraction of specimens falling at or below a given impact resistance value, providing a complete picture of the distribution without assuming an underlying statistical model, making it particularly useful for small sample sizes. The 74% CF distribution rises steeply, with all specimens falling within a relatively narrow range of approximately 2,350 to 3,050 J/m, indicating consistent impact resistance performance across specimens. The 60% CF distribution, by contrast, begins at substantially lower values near 1,350 J/m and extends to nearly 4,000 J/m, producing a shallower, more gradual curve. While the two distributions overlap significantly in the 2,400–2,800 J/m range, the 60% CF population has a considerably longer tail in both directions. This broader spread is consistent with the more heterogeneous fracture behavior of the 60% CF group and its greater sensitivity to processing-induced variability such as local resin-rich regions. These results suggest that while the 60% CF composites are capable of achieving higher peak impact resistance values, the 74% CF composites offer more predictable and repeatable impact performance.

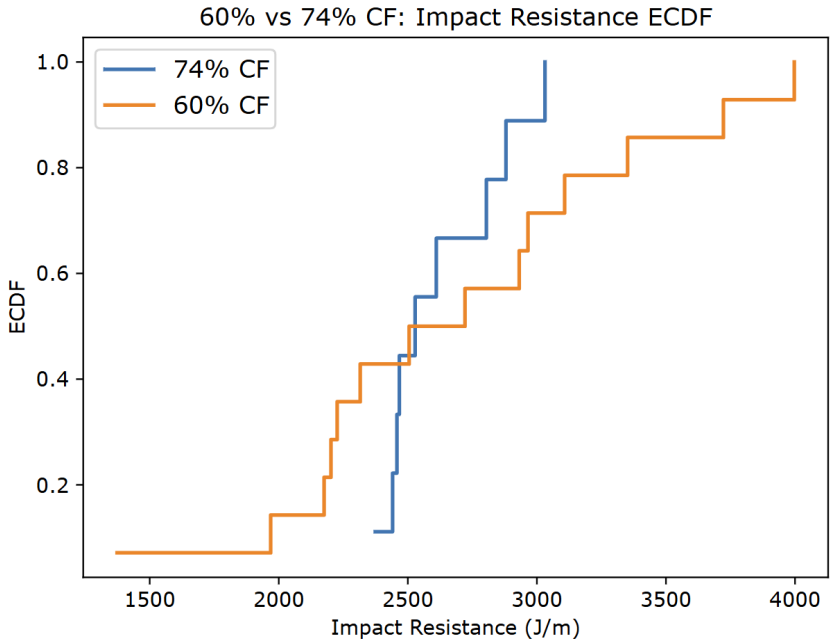


Figure 5-18. Impact resistance ECDF for 60% and 74% CF samples.

A strong positive correlation between percent dissipated energy and break energy was observed across both composite composites, as shown in Figure 5-19. This consistent linear trend across the 60% and 74% CF samples, suggests that the fundamental mechanism of energy absorption during impact is similar regardless of fiber volume fraction. The 74% CF specimens cluster tightly in the lower-to-mid range of both axes, with percent dissipated values between approximately 0.32 and 0.41 and break energies between approximately 7.5 and 9.6 J. The 60% CF specimens span a wider range, extending to percent dissipated values above 0.55 and break energies approaching 12.8 J. These higher-energy events in the 60% CF group correspond predominantly to complete break failures, where the full separation of the specimen requires greater total energy input. The clustering of the 74% CF data reflects the more constrained, hinge-dominant fracture mode of that composite, in which fracture is arrested before full separation and the specimen absorbs energy over a shorter displacement.

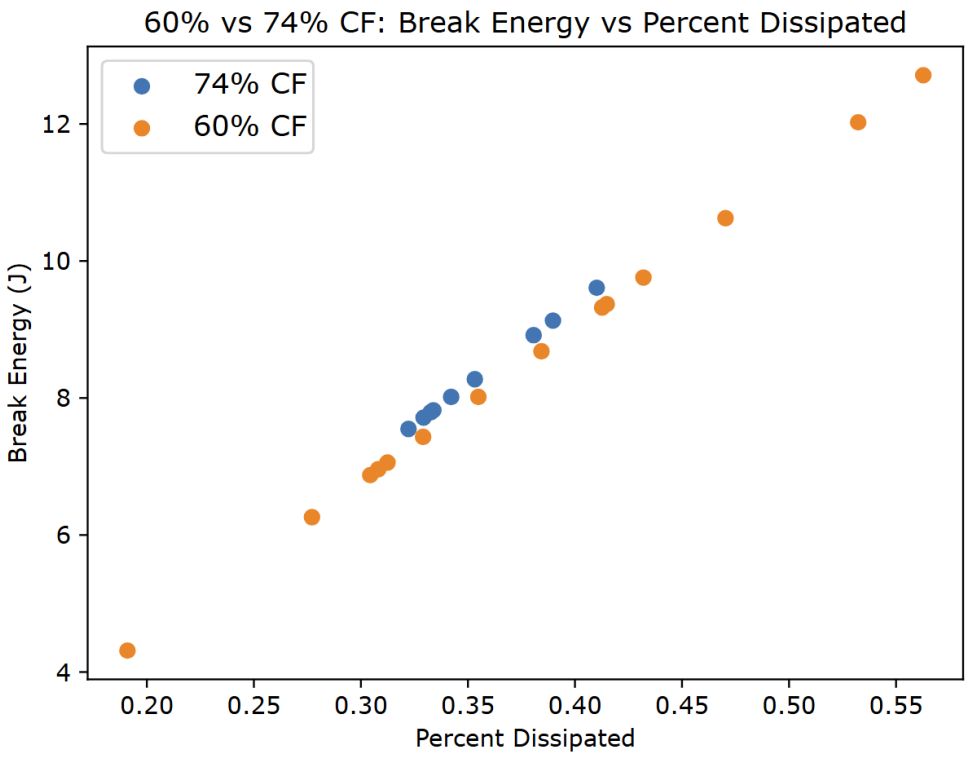


Figure 5-19. Break Energy vs Percent Dissipated CDF for 60% and 74% CF samples

5.4 Conclusion

Completely bio-based composites were created at PulFlex Inc using a bio-based polyurethane resin from BASF and a recycled carbon fiber from CrossLink. Baseline properties of the polyurethane confirmed that the resin performed within the range of expected properties for a bio-based polyurethane, while the carbon fiber performed slightly under expectation for a recycled carbon fiber. Together, the material was able to undergo pultrusion, with difficulties arising due to the hygroscopic nature of the resin and the degradation of (or lack of) sizing on the carbon fiber. With respect to fiber performance, compatibility issues arise between the resin and carbon fiber which leads to fracture along the fiber matrix. These incompatibilities tend to decrease at lower fiber volume loading. Ultimately, while the creation of a composite was a success, additional attention must be paid to tow uniformity and sizing, and resin chemical properties in order to ensure that

both systems are ready for real world applications at scale. This study provides great insight into the potential of fully green composites and the challenges still to overcome.

5.4.1 CRediT Statement of Contribution

The work in this chapter was heavily contributed to by Steven Mamolo, who contributed to the methodology, software, formal analysis of data, investigation, data curation, writing, editing, and data visualization. Jacob Harris contributed formal analysis, investigation, writing, editing, and data visualization. Chiamaka Odenigbo aided with investigation and editing. Luohaoran Wang contributed to the investigation and editing of the research presented in this chapter.

Chapter 6 Conclusion

With four years until the anticipated culmination of the Paris Agreement, the need for sustainable innovations across industries becomes pressing. An introduction of bio-based polymer composites that can also function as carbon sequestration materials aids in the active pursuit of this goal. Cellulose, a polysaccharide with β(1-4) glycosidic linkage , when fibrillated and mechanically ground, can approach nanosizes. This nanocellulose, which has been investigated for usage in wound therapy and drug delivery, is the subject of interest for enhancements in plant growth outlined in this thesis.

Cellulose nanofibril proved to improve the mass of CNF treated flax primary stems by 0.09 grams, an amount that was statistically significant at the 95% confidence interval, as compared to control plants. When observing other parameters, such as shoot length and root length, differences were not significant at the 95% confidence interval. Serendipity provided the opportunity to change nanocellulose morphologies. The hypothesis for growth, which is based on the breakdown of nanocellulose in soil be either root cap enzymes or cellulases exuded by microbes in the soil, provides an explanation for why cellulose nanocrystal results would prove more favorable than results in nanocrystal. This hypothesis held for experimentation with cellulose nanocrystal, which featured shoot heights in treated stems that were between 9% and 33% larger than the control and dry weights of between 11% to 55% of the control. These features maintained for internal

morphology, with plant linear density—the plant mass over the plant height—and plant matter area density—the plant mass over the occupied cross-sectional area—that exceeded both control values for all tested populations. Improvements in the experimentation between the first and second iterations of experiments yielded larger plants independent of the treatment conditions. Flax plants treated with cellulose nanocrystal were tested to obtain both their stem and fiber tesnile properties. Flax stems tested via tensile testing were found to have some values greater than the control, but with not enough separation to identify them as significant at the 95% confidence interval. Flax fibers were extracted from stems and loaded onto a paper frame to ascertain their tensile strength and modulus. Single treatment and weekly treatment fibers performed below control fibers. This may be due to differences in the quantity of elementary fibers in each treatment group's technical fiber bundle, which may be due to differences in the ease of retting. Weibull analysis provided little additional information regarding fiber reliability, due to low sample number. Griffith model provided insight into the potential non-linearity of the reliance of fiber diameter on material property, however low replicate number permeates into ill-fitting of regression models.

A techno-economic analysis is necessary to confirm the potential for farms to dedicate their land to flax farming and to implement our technologies. After determining the baseline cost for outdoor flax growth, models were created to include the cost of treating flax with cellulose nanocrystal and the cost of synthesizing cellulose nanocrystal from scratch, which would then be used as a growth additive. Exploratory synthesis confirms that it is possible to generate rod-like structures from flax, likening the structure to a cellulose microfibril, from macro-size flax ground in a commercial grinder. 87.91% of farm costs are due to nanocellulose when adding cellulose nanocrystal to flax.

This jumps to 89% when nanocellulose is synthesized on the farm. At the current rate of $750/kg of cellulose nanocrystal, there is the opportunity for farms to sell $1.1 million of excess CNC at 20,000 bushels of flax produced when using treatment doses for optimal growth (0.023g/seed) as defined by this thesis.

In addition to plant-based alternatives to glass fiber composites, this thesis investigated other bio-based composites. A carbon fiber made from recycled textiles and a polyurethane made from bio-based polyols was created at PulFlex, Inc using a process called pultrusion—a portmanteau of pull and extrusion. Materials characterization was conducted on these novel materials, with a single fiber tensile modulus 289.9 ± 99.9 GPa and ultimate tensile strength placed at 2.14 ± 0.79 for the carbon fiber, and polyurethane tensile modulus between 700 and 800 MPa. Composite properties were impacted by lack of sizing and hygroscopicness of the resin which led to non-wetting of the fiber. Resulting properties of the composite performed below expectations set with rule of mixture. This experiment highlighted necessary considerations for the synthesis of bio-based products.

Supplemental and future work conducted in the thesis expand upon previous work, with a focus on long-term applications and composite creation. Facilitating the transition to fully bio-based products in time to impact the course of the Paris Agreement, and other such climate change goals, is a focus for the author and a directive for future work.

Appendices

Appendix A: Supplemental Work

A.1 Controlled Growth of Arabidopsis on CNF Modified Growth Media

To ascertain exactly how the mechanism for enhanced growth occurs, it was necessary to create a sterile environment and induce growth in Arabidopsis, the plant version of a mouse-model. The growth chambers in the basement of the biological sciences building, while contained, does not provide 100% sterility. Soil, fertilizer water, and human scientists alter the sterility of the environment, even while seeds and pots can be sterilized. To create a sterile growth environment, typically seeds are sown on agarose media that has been sterilized. This procedure occurs in a laminar flow hood using surfaces and materialized that have been washed with 70% ethanol.

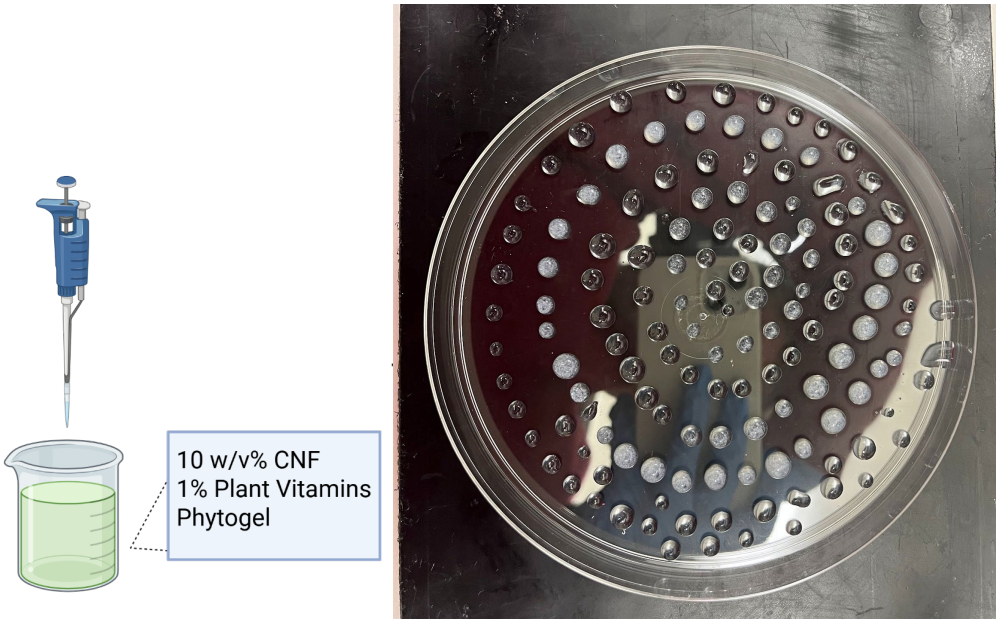
Remembering the sterile agarose media, we are able to recreate droplets with cellulose nanofibril paste in order to induce a growth-effect in Arabidopsis. To sterilize the Arabidopsis seeds, a sufficient amount of seeds was aliquoted into 1.5ml tubes. 70% ethyl alcohol was added to a tube of seeds and inverted several times to mix. After removing ethanol from the tube, it was replaced with 20% commercial bleach with tween-20. The bleach solution was evacuated and the seeds rinsed with autoclaved water. This washing step, with water, was repeated four to five times to sufficiently remove residual bleach from the seeds.

Sterilized seeds were then sown on plates of agarose media with sucrose. As seeds germinated, droplets of cellulose nanofibril in Murashige-Skoog were created. 0.753g of Murashige and Skoog basal medium, 0.35g of 2-(N-morpholino)ethanesulfonic acid (MES) buffer, and 4.34g of Phytogel were measured and mixed together in 500 mL of deionized water by magnetic stirring. While stirring, drops of 1M KOH were slowly added, with monitoring, until pH was between 5.8 and 6.

Upon reaching the necessary pH threshold, another 200mL of DD H_2O was added. 7.00g of cellulose nanofibril was measured and added to the 700 mL solution with stirring until the paste dispersed the CNF. The Erlenmeyer flask with the CNF-media solution was covered and autoclaved on a standard setting "PO2 Liquids 2" on the 5th floor of the Biological Sciences Building at the University of Michigan-Ann Arbor. Plates of ¼ x MS media with no sucrose, as well as a beaker of warm autoclaved water, were placed in the sterilized laminar flow hood. After the one hour autoclave cycle was complete, the CNF-MS media solution was placed back on a magnetic stir chamber at a speed of 230 RPM and heated to 60 °C, then 40 °C. It is important to maintain sterility and to move quickly during the following steps.

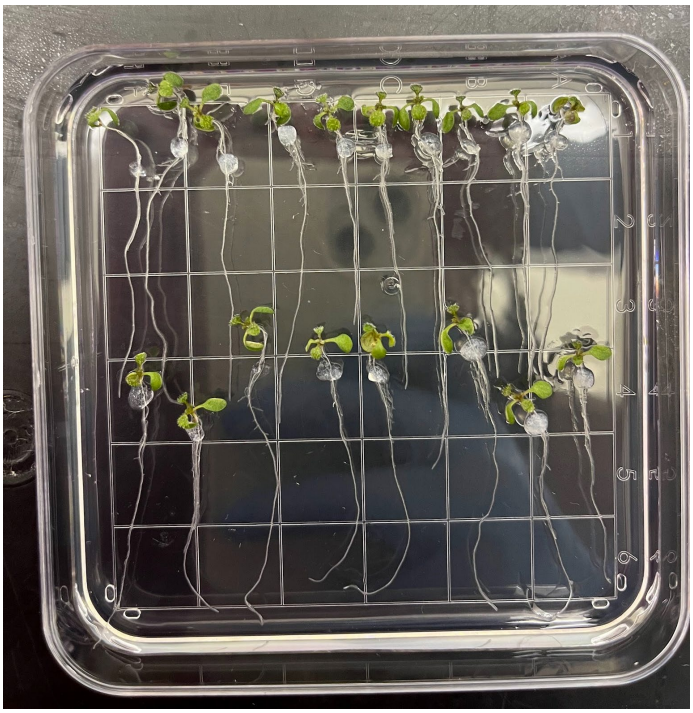
While CNF was under constant stirring, the previously germinated Arabidopsis plants were taken out from the incubator, removed = from the ¼ x MS media with sucrose, and gently washed in the warm autoclaved deionized water. These seedlings were then placed onto the new ¼ x MS media plates with no sucrose. The new plates were re-taped with breathable, growth specific tape put back in incubator.

Following a reseeding of germinated seedlings, the CNF solution was removed from heat. Moving quickly, droplets CNF was pipetted onto sterile empty plates in different sizes, with a 0.5 mL serving as the model for larger drops, 250 µL pipette for medium drops, 100 µL for small drops. Upon completion, the plates were closed, taped, and refrigerated for 2.5 hours, or until the drops had completely firmed.



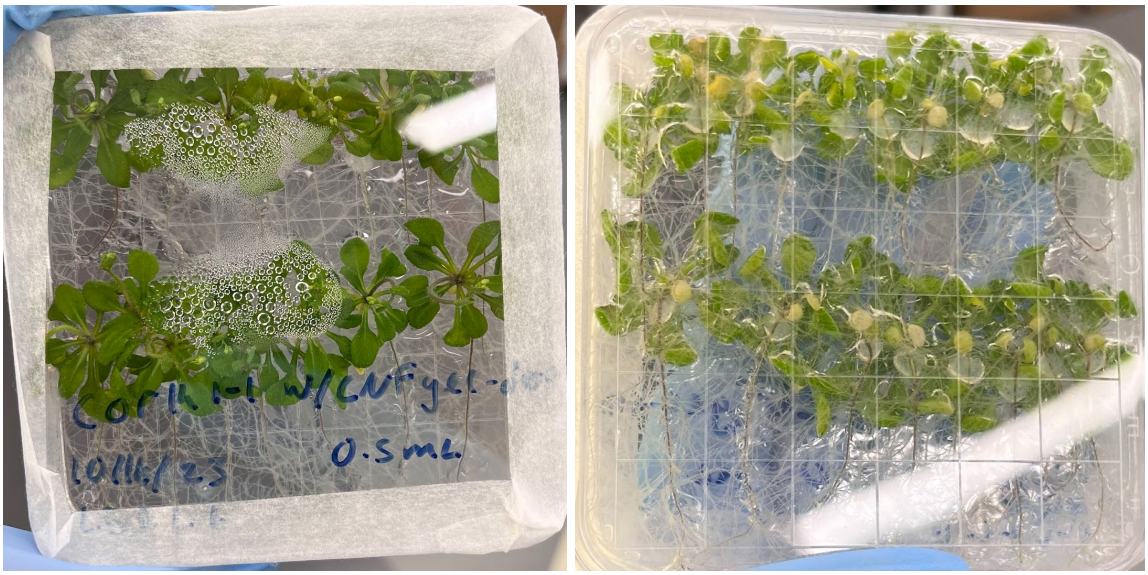
Appendix Figure 1. Procedural guidelines for creating CNF droplets.

The incubated plants and CNF droplets were removed from their chambers, surface sterilized, and place back in the laminar flow hood. The CNF droplets were carefully removed from their sterile plate and gently placed at the base of the plant—the top of the root node. This was repeated for all remaining seedlings before the Arabidopsis plants were resealed and placed back in the incubating growth chamber. Excess CNF droplets were returned to the refrigerator.



Appendix Figure 2. CNF droplets on pre-germinated Arabidopsis plants.

Droplets of CNF proved different in color and clarity based on the amount of cellulose nanoparticle present in the droplet. Due to the insolubility of CNF, proper dispersion in the heated water is only possible at high temperatures. Cooling in any amount leads to separation of the CNF from the water. Moreover, the thicker CNF particles tend to rest in the center of the pipette tip, leading to differing amounts in drop-size as one tip is used for numerous droplets. To maintain droplet size, switching pipette tips often was necessary.



Appendix Figure 3. CNF droplet treated Arabidopsis plants following two weeks of growth.

Following treatment with CNF droplets, Arabidopsis plants continued to grow as expected. Growth was not monitored alongside a control. Experiments could be vastly improved by using sonication to permanently suspend the CNF in the solution, prior to autoclaving. Improvements in drop formation have already been set forth, with CNF-MS media plates being created and solidified, then droplets were cut out with premeasured forms: the back of a 1 mL pipette tip.

This form of controlled growth media may be able to be used to observe cellulose nanoparticle seeking behavior in root caps of flax plants. Should this prove operational, flax plants would be able to grow and germinate on an amount of CNF-¼ x MS media which, due to its translucency, would be a great sterile observation site for how flax plants interact with cellulose nanoparticles as roots develop.

A.2 Creation of Hydrogels using Cellulose Nanocrystal

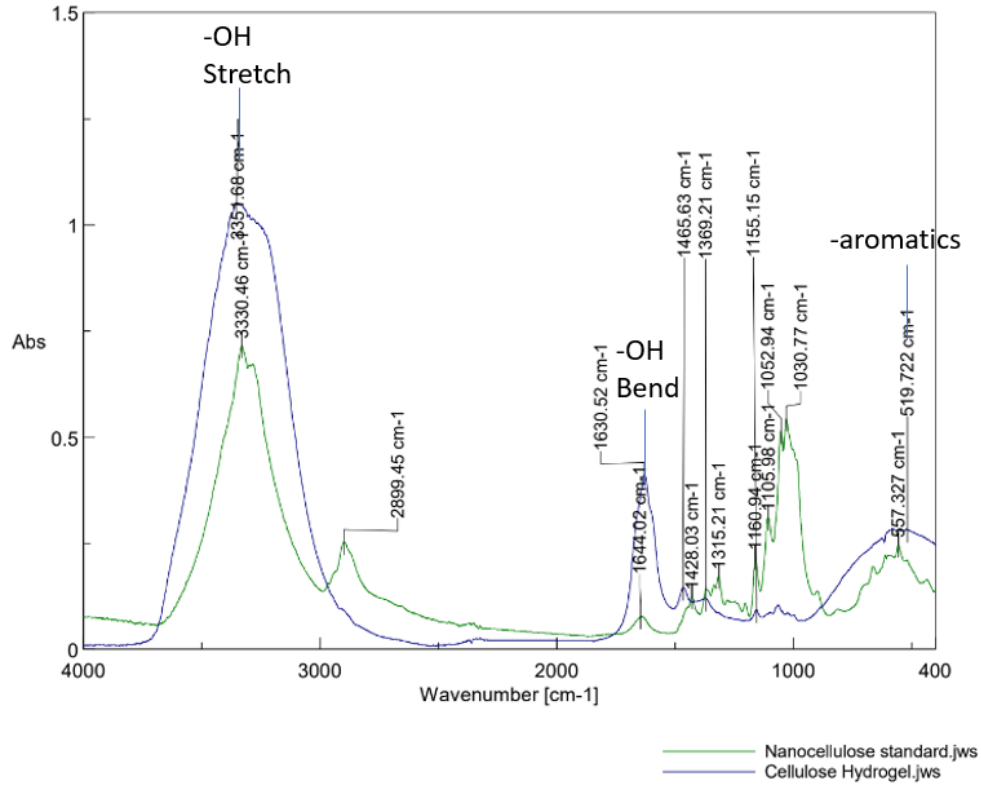
Considering the applications of cellulose nanocrystal enhanced growth, dosing, packaging, and delivery of cellulose nanocrystal is of heavy consideration. Hydrogels are cross-linked hydrophilic polymer chains that swell and recede with the presence of water[119]. Hydrogels have been investigated for uses in tissue engineering and wound care[119] and, due to its semi-permeable matrix, may also be the ideal system of choice to package and deliver cellulose nanocrystal to plants. Long-term goals from this project would be to package, and deliver, CNC via the hydgrogels matrix and water soluble nutirent ions through water.



Appendix Figure 4. Hydrogel synthesized from cellulose nanocrystals.

2 wt% Cellulose Nanocrystals were dispersed into a 1.9 wt% sodium hydroxide/10 wt% urea solution by sonicating for six minutes. The solution was then sectioned into ice cubes trays and placed in a freezer for more than 24 hours to allow gelation. After the solution had frozen, it was then thawed at room temperature, followed by immersion into ethanol (99 vol %) for coagulation. Solvent exchange was carried out after coagulation by immersing the gel in tap water.

In future iterations, a set of samples experiencing solvent exchange with a mixture of 1-part fertilizer water and 4-parts tap water will also be synthesized. The consistency of the sample will be observed, with plants added to stable hydrogels to determine the possibility of growth for flax plants on the hydrogels. Hydrogels will need to be observed by SEM, sessile drop contact angle measurement, FTIR, degradation in water, and degradation in soil. In the first iteration of hydrogel synthesis, Fourier Transform Infrared Spectroscopy was performed to compare synthesized hydrogels to pure cellulose nanocrystal to determine the presence or absence of characteristic peaks between the two materials.

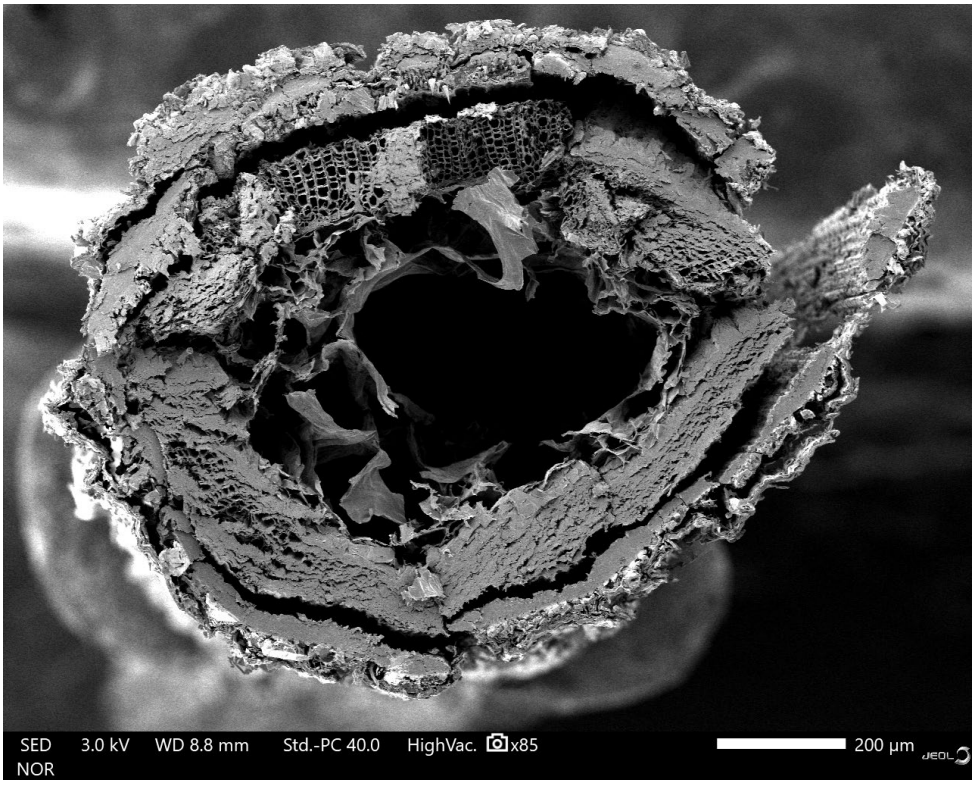


Appendix Figure 5. FTIR spectrograph comparing a standard of cellulose nanocrystal to synthesized cellulose hydrogel.

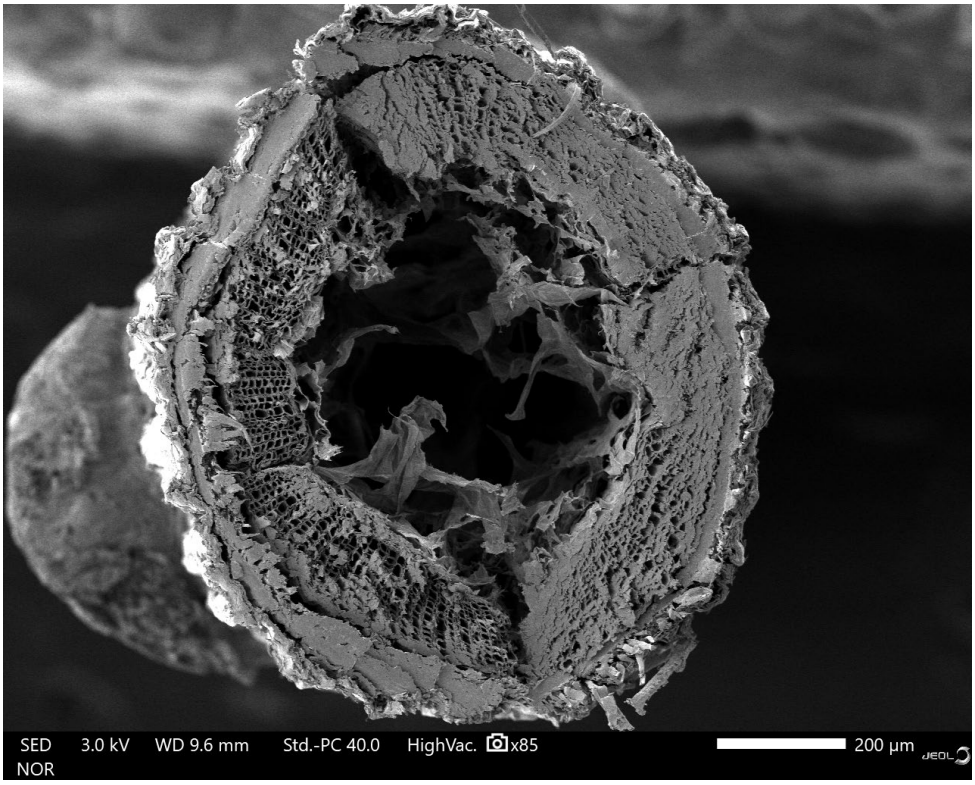
The presence of larger -OH stretch and -OH bending peaks corresponds directly to the addition of water in the sample, which tends to broaden -OH peaks. Peak broadening of the cyclohexane peaks

is present, as well as the absence of C-O-C peaks, which may be due to a change in the polymer structure due to cross-linking. Additional characterization methods are necessary to ascertain the chemical mechanism for cross-linking; Energy Dispersive X-ray Spectroscopy, paired with Scanning Electron Microscopy, may assist in determining why two characteristic carbon peaks (CH_2 peak at 2889 cm^{-1}, and the 1030 cm^{-1} C-O-C peak) disappear when cross-linking occurs.

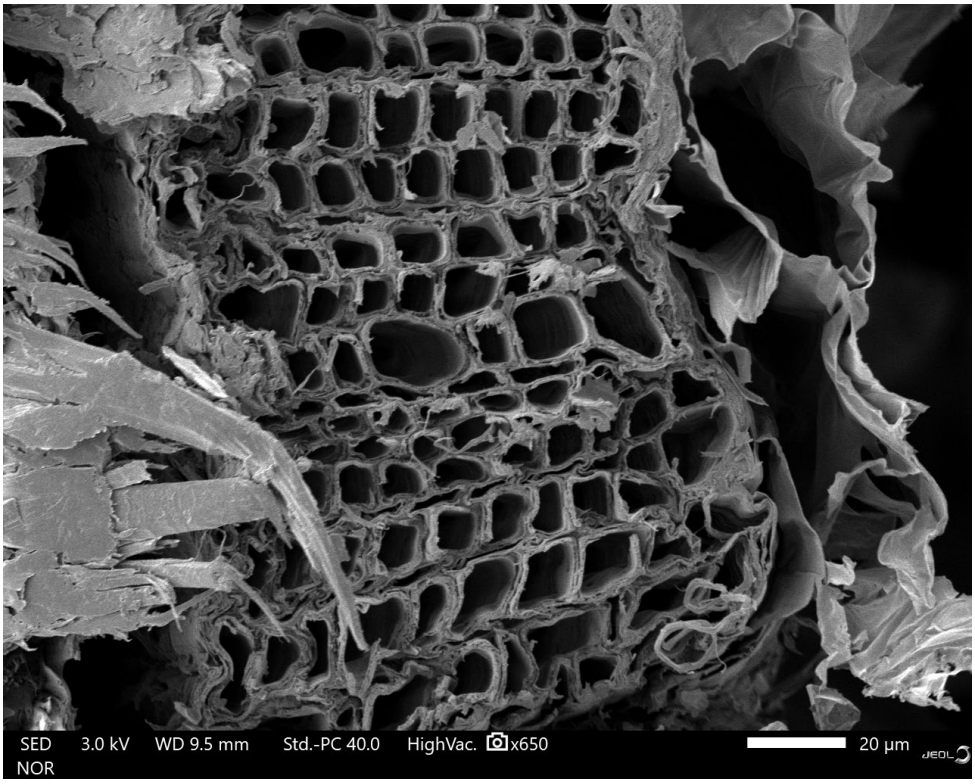
A.3 Scanning Electron Microscopy Images of Flax Stems and Fibers



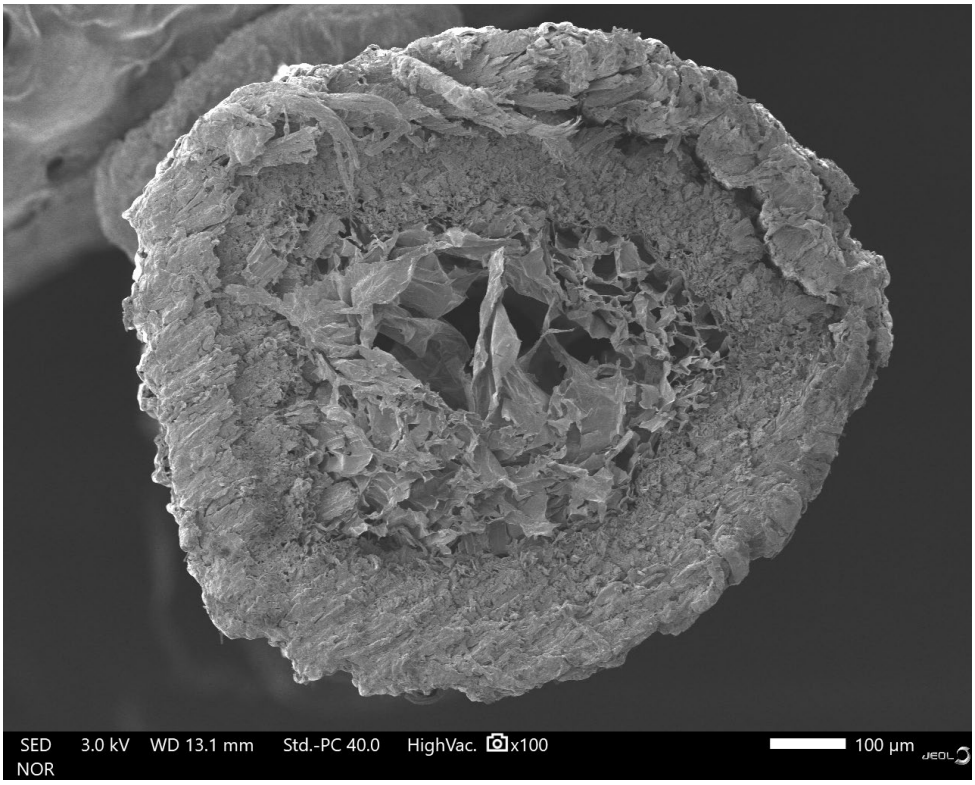
Appendix Figure 6. Cross-section of a control flax stem (Stem 1).



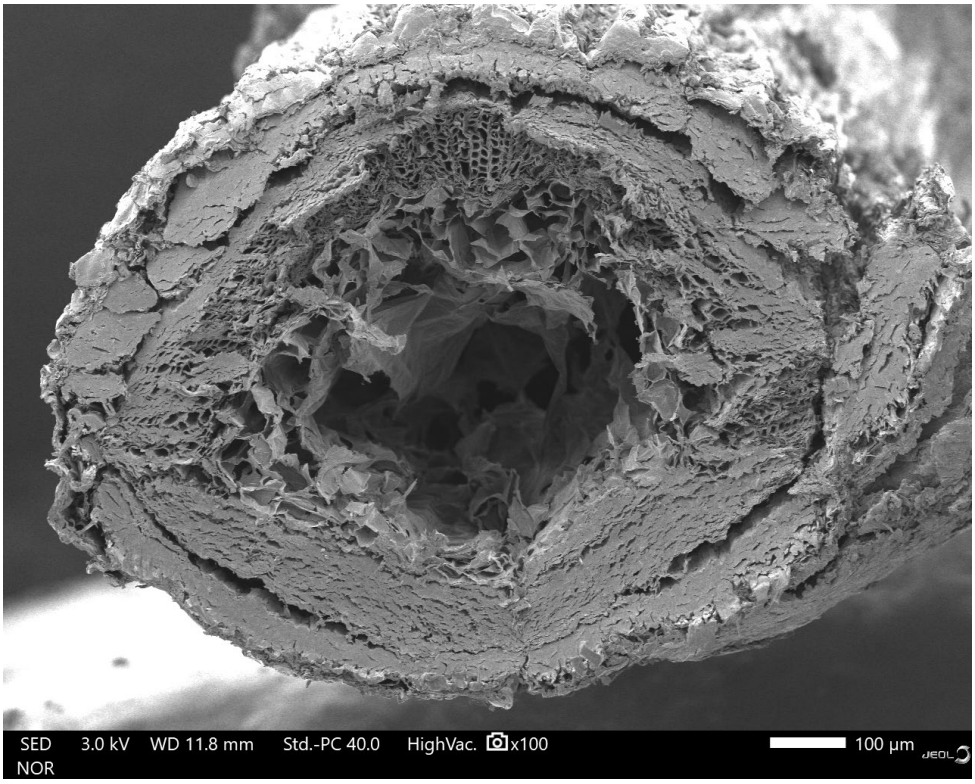
Appendix Figure 7. Cross-section of a control flax stem (Stem 4).



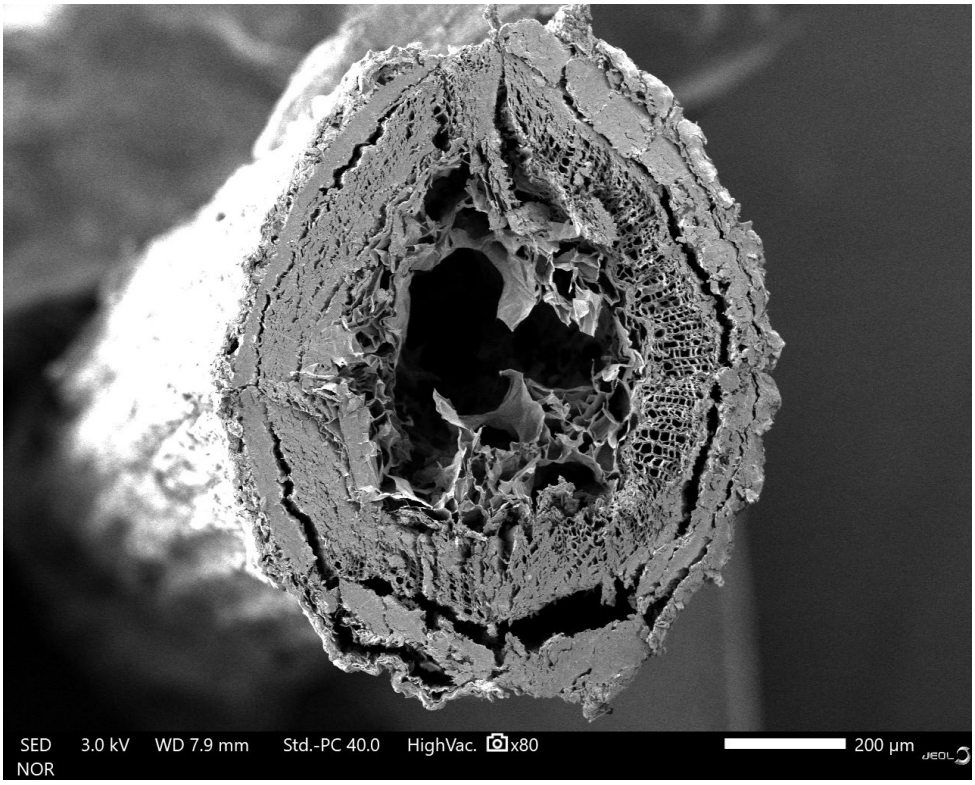
Appendix Figure 8. Xylem for an enzyme-retted flax stem, untreated. (Stem 4).



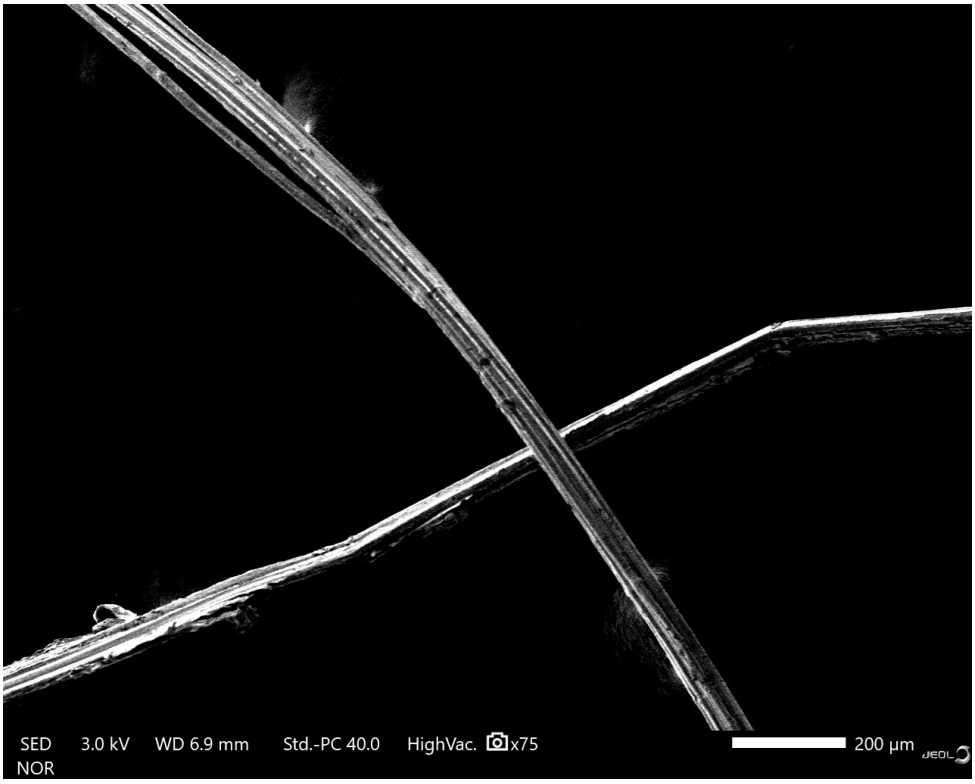
Appendix Figure 9. Cross-section for a flax stem treated with one single treatment of cellulose nanocrystal. (Stem 1).



Appendix Figure 10. Cross-section of a flax stem treated weekly with cellulose nanocrystal. (Stem 2).



Appendix Figure 11. Cross-section of a flax stem treated once a week for 12 weeks. (Stem 5).



Appendix Figure 12. Technical fibers derived from flax plants treated once a week for 12 weeks.



Appendix Figure 13. Technical flax fiber bundle derived from flax plants treated once a week for 12 weeks.

Appendix B: Future Work

B.1 Growth of CNC Treated Flax Plants on Small-Farm Scale

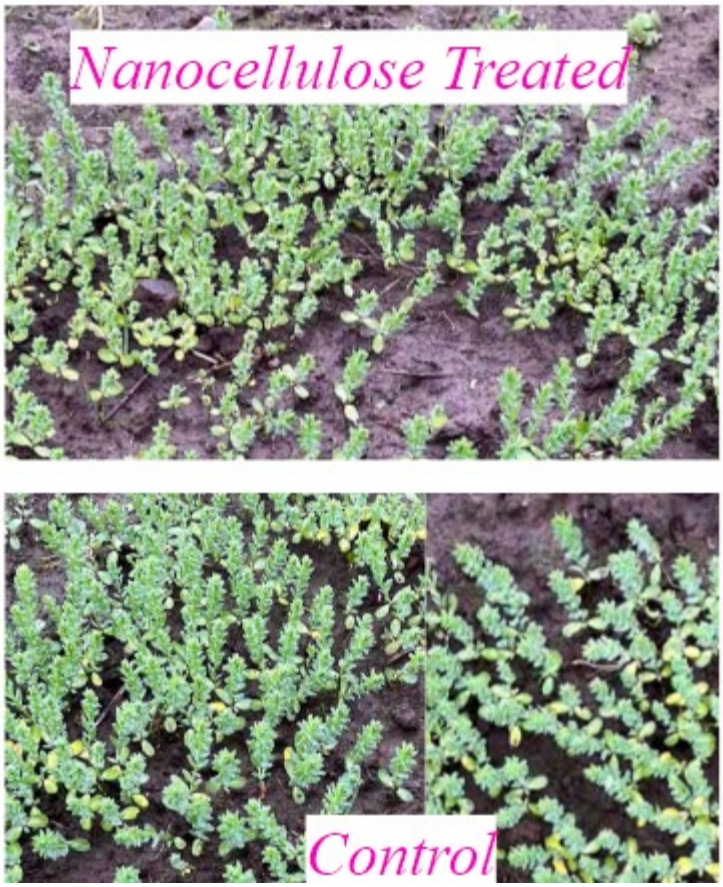
In order to apply research outcomes learned over the course of this doctoral thesis, we must extend beyond the laboratory space. In partnership with Coast Fibers, a flax fiber producer, farm, and research entity of out Oregon, we were able to experimentally apply cellulose nanocrystal in field to flax grown in winter.



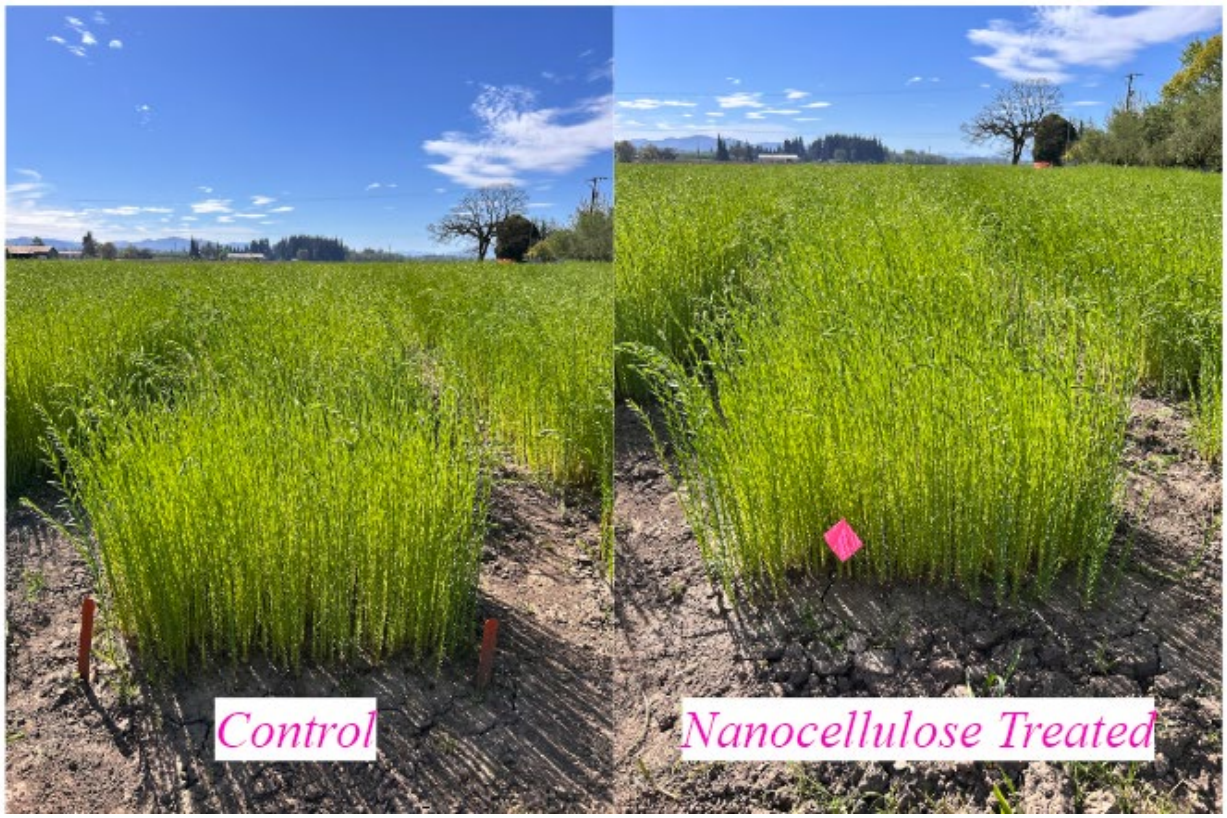
Appendix Figure 14. Winter flax planted in November 2025 at Coast Fiber's farm in Oregon.

1300 flax seeds were planted in soil. After planting, 300 grams of cellulose nanocrystal—which had been suspended in a large amount of water by sonication at the University of Michigan and shipped to Oregon—was incorporated into the soil. A control population of plants was planted in

a nearby plot. Plants were grown until flowering, with cultivation occurring at the point which plants no longer grow.



Appendix Figure 15. Flax photographed at 8 weeks of growth at Coast Fibers in Oregon.



Appendix Figure 16. Flax plants photographed at 14 weeks of growth at Coast Fibers. Control flax plants were observed to be between 24-30 inches with treated flax plants reaching heights of between 19-29 inches.

The expected timeline for these plants is cultivation and retting in the first weeks of June. These plants will then be sent to the University of Michigan for the extraction of their fibers and to undergo fiber testing and analysis.

Soil testing was conducted on soil from both plots, control and cellulose nanocrystal treated, in order to determine differences in microbial processing or uptake. These results are reported below in **Error! Reference source not found.**, where L stands for low, M stands for medium, H stands for high, VH stands for very high results when compared to a standard soil sample.

Appendix Table 1. Results from soil testing on soil obtained from field trial at Coast Fibers in Oregon.

Sample	*Organic Matter*	*Magnesium*	*Calcium*	*Sodium*	*Potassium*	*Phosphorous*
Control	3.9 M	308 L	1674 L	15.5 L	489 VH	134 VH
CNC Treated	3.8 M	343 L	1839 L	16.8 L	552 VH	137 VH

Differences in soil content may indicate interactions occurring in the soil, or different needs for treated plants versus control planting. Without additional metrics, these differences may be attributed to natural variations between the two plots. Due to the relative closeness of many values, it is important to observe these values as trends to be further explored by associates in the field, particularly biologists, who may have better testing methods to understand cation exchange and the depletion of these ions in the soil. Calcium, in particular, seems to have a larger change between treated and control and should be monitored. To confirm our hypothesis, a large shift in the present organic matter would have to be observed between treated and control plants, however this was not of note.

B.2 Creation of CNC Treated Flax Fiber-Epoxy Composite Materials

Long-term applications of this dissertation are attuned to the creation of composite materials to rival and replace e-glass fiber. Fiber reinforced composites for structural materials is how this concept manifests. As such, the creation of composites from these materials is essential. While fiber reinforced composite is the target, because of early success seen in Chapter 2.2.2, crushed stem composites were also of interest for analyzing improvements in composite quality.



Appendix Figure 17. Crushed hemp stem reinforced composites.

Retted flax, and separately hemp, stems were cut using garden shears and then further ground using a commercial blender were sectioned off to create 35% volume fraction composites with Epon828 as the matrix. Cut stem fragments were mixed into uncured resin and then poured into the molds under ambient pressure and temperature.



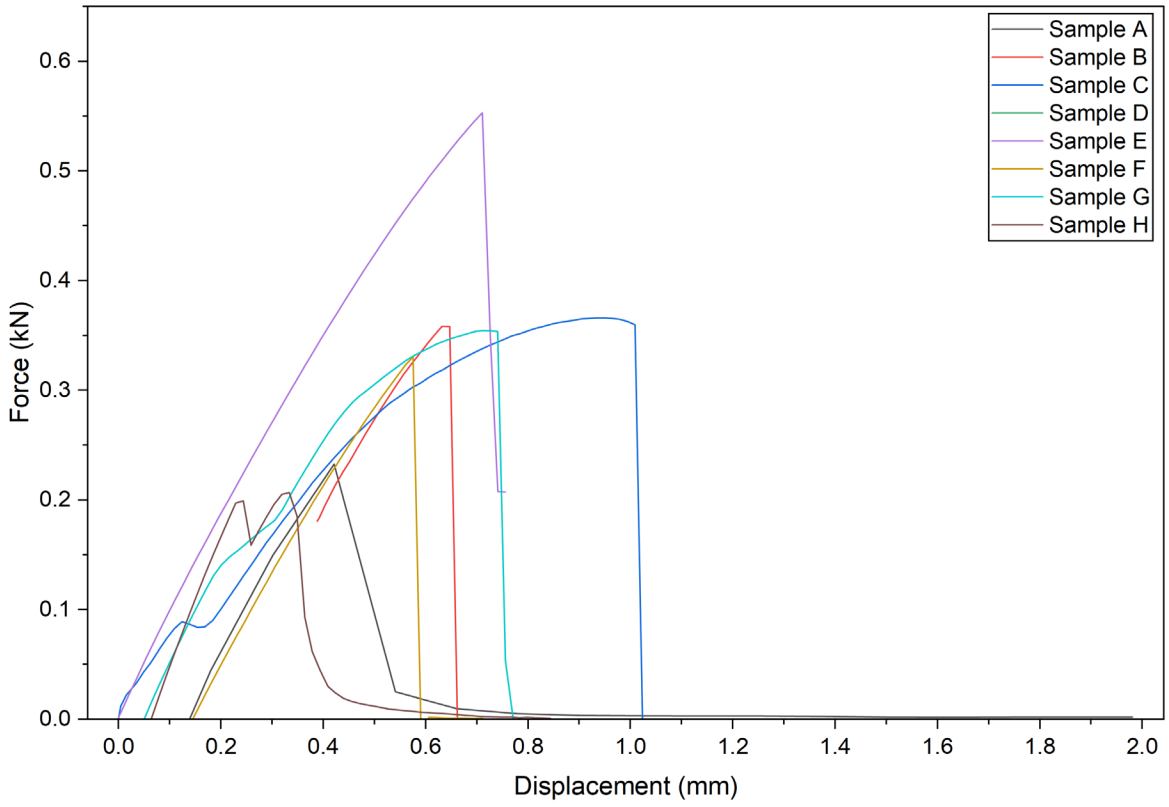
Appendix Figure 18. Crushed hemp stem composite.



Appendix Figure 19. Enzyme retted flax crushed flax stem composites.

Crushed flax stem composites contained a combination of retted stems from all treatment conditions discussed in Chapter 2.2.2. This was due to small biomass availability and a desire to prove the concept of viability. Future experiments will use fiber reinforced composite materials a improve upon the methodology for composite creation. Force-displacement curves were created from tested flax composites. Difficulty in testing arises when the instrument load becomes superior

to the compression strength of the composite. This results in crushing of the ends of the composite before fracture. Nevertheless, tensile testing of crushed stem composites is a possibility.



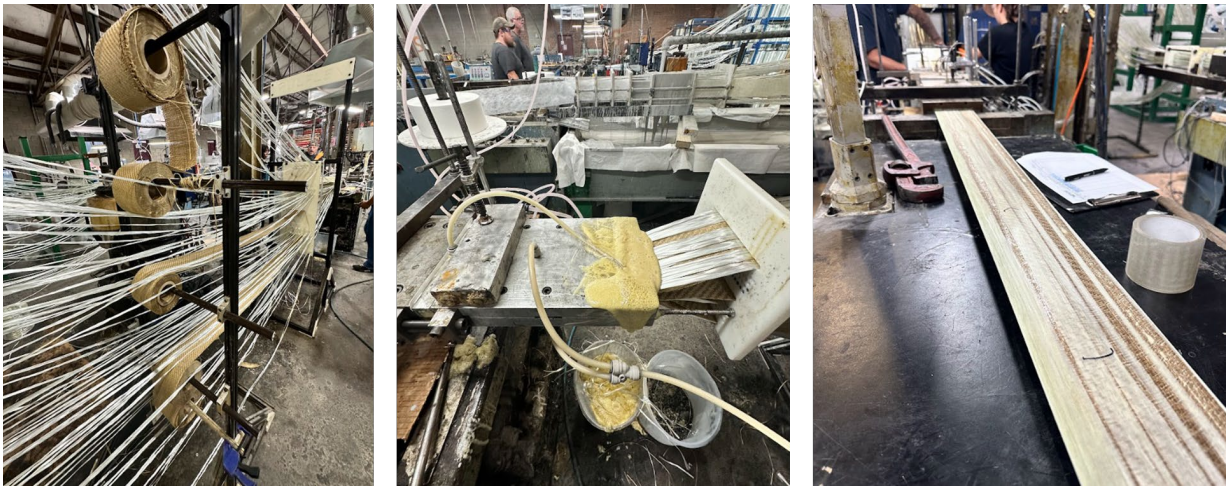
Appendix Figure 20. Force-displacement curve for CNC treated crushed flax stem composites.

Force-displacement curve exposes low loads; with uncertain volume fraction and cross-sectional area little can be said about the characteristic behavior of the composite.

B.3 Hybrid Flax-Carbon Fiber Composites via Pultrusion

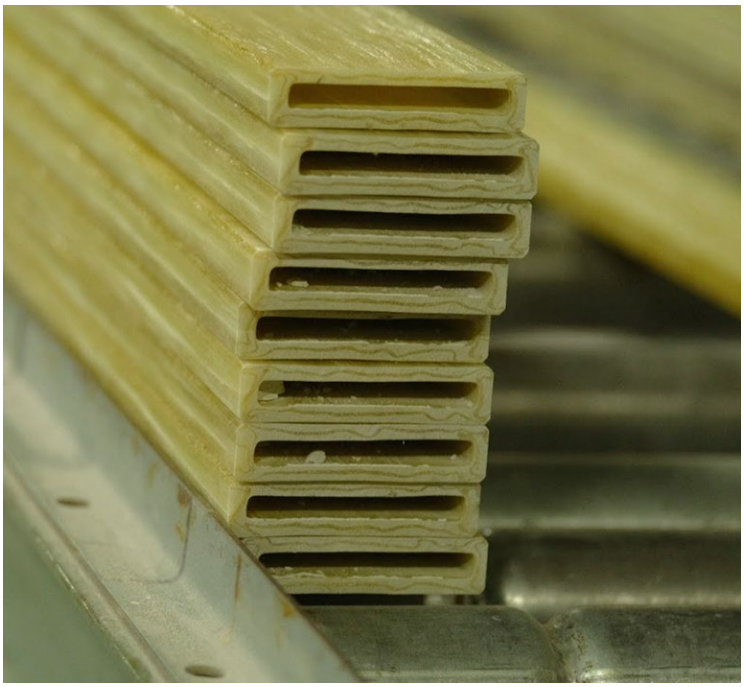
The original mission statement of the pultrusion project emphasized the use of a lignin-derived carbon fiber in addition to our bio-based carbon fiber to create a hollow rectangle shape. The targeted application discussion focused on battery separator module. Supply chain and experimental hurdles changed the original model to lack the lignin derived carbon fiber.

Serendipitous experimentation led to investigating a high lignin content fiber—flax fibers—as the replacement for the lignin derived carbon fiber.



Appendix Figure 21. Process for creating pultruded plaques of glass fiber and flax fiber.

Initial plaques were produced with glass fiber on the exterior and glass fiber on the interior. CrossLink carbon fiber was tested in addition to glass fiber. There was immense difficulty in the pultrusion process between carbon fiber and flax, as carbon fiber tows separated and knotted during many points in the pultrusion process.



Appendix Figure 22. Glass fiber-flax fiber reinforced pultruded coupons in hollow rectangle geometry.

A second processing day provided the opportunity to pultrude the hybrid composite in the hollow rectangle shape. Additional testing will be done on this geometry, with focus on natural fiber sizing.

Bibliography

1. The Paris Agreement | UNFCCC. https://unfccc.int/process-and-meetings/the-paris-agreement.
2. Successes in climate action. *Nat. Clim. Chang.* **16**, 1–1 (2026).
3. Gonçalves, R. M., Martinho, A. & Oliveira, J. P. Recycling of Reinforced Glass Fibers Waste: Current Status. *Materials (Basel)* **15**, 1596 (2022).
4. Bandwidth Study on Energy Use and Potential Energy Saving Opportunities in the Manufacturing of Lightweight Materials: Glass Fiber Reinforced Polymer Composites.
5. Pervaiz, M. & Sain, M. M. Carbon storage potential in natural fiber composites. *Resources, Conservation and Recycling* **39**, 325–340 (2003).
6. Zhang, M. *et al.* Cellulose-based materials for carbon capture and conversion. *Carbon Capture Science & Technology* **10**, 100157 (2024).
7. Duc, C. K. T., Tuan, N. T., Linh, T. C., Luong, H. V. T. & Pham, D. T. Sustainable recovery of cellulose from lotus seedpods: Integrating process optimization and environmental-preliminary economic analysis. *Bioresource Technology* **441**, 133603 (2026).
8. Biodegradability of cellulose fibers, films, and particles: A Review :: BioResources. https://bioresources.cnr.ncsu.edu/.
9. Bian, H. *et al.* Sensitive explosive loaded in porous cellulose for improved stability. *Materials Chemistry and Physics* **257**, 123700 (2021).

10. Li, J. & Kasal, B. Review on the Structure–Property Relationship of Lignocellulosic Materials Measured by Atomic Force Microscopy. *Biomacromolecules* **26**, 1404–1418 (2025).
11. Thomas, B. *et al.* Nanocellulose, a Versatile Green Platform: From Biosources to Materials and Their Applications. *Chem. Rev.* **118**, 11575–11625 (2018).
12. Hansini, A. M. P. *et al.* From Nature to Innovation: Advances in Nanocellulose Extraction and Its Multifunctional Applications. *Molecules* **30**, 2670 (2025).
13. Kaushik, M. *et al.* Transmission Electron Microscopy for the Characterization of Cellulose Nanocrystals. in *The Transmission Electron Microscope - Theory and Applications* (IntechOpen, 2015). doi:10.5772/60985.
14. Fratzl, P. & Weinkamer, R. Nature's hierarchical materials. *Progress in Materials Science* **52**, 1263–1334 (2007).
15. Barja, F. Bacterial nanocellulose production and biomedical applications. *J Biomed Res* **35**, 310–317 (2021).
16. Nanocellulose: A Comprehensive Review of Sustainable Applications and Innovations. *Journal of Renewable Materials* **13**, 1315–1346 (2025).
17. R, R. *et al.* Bacterial nanocellulose: engineering, production, and applications. *Bioengineered* **12**, 11463–11483.
18. Alberts, B. *et al.* The Plant Cell Wall. in *Molecular Biology of the Cell. 4th edition* (Garland Science, 2002).
19. Das, R., Lindstrom, T. & Khan, M. Nanocellulose preparation from diverse plant feedstocks, processes, and chemical treatments: A review emphasizing non-woods :: BioResources. https://bioresources.cnr.ncsu.edu/.

20. de Assis, C. A. *et al.* Cellulose micro- and nanofibrils (CMNF) manufacturing - financial and risk assessment. *Biofuels, Bioproducts and Biorefining* **12**, 251–264 (2018).
21. Babicka, M. *et al.* Nanocellulose Production Using Ionic Liquids with Enzymatic Pretreatment. *Materials (Basel)* **14**, 3264 (2021).
22. Theivasanthi, T., Anne Christma, F. L., Toyin, A. J., Gopinath, S. C. B. & Ravichandran, R. Synthesis and characterization of cotton fiber-based nanocellulose. *International Journal of Biological Macromolecules* **109**, 832–836 (2018).
23. Alkali-Controlled C–H Cleavage or N–C Bond Formation by N2-Derived Iron Nitrides and Imides | Journal of the American Chemical Society. https://pubs.acs.org/doi/10.1021/jacs.6b04984.
24. Li, N., Yang, S., Huang, Z. & Pan, X. Radical Reduction of Polymer Chain-End Functionality by Stoichiometric N-Heterocyclic Carbene Boranes. *Macromolecules* **54**, 6000–6005 (2021).
25. Poulose, A. *et al.* Nanocellulose: A Fundamental Material for Science and Technology Applications. *Molecules* **27**, 8032 (2022).
26. Meija, J. *et al.* Particle Size Distributions for Cellulose Nanocrystals Measured by Transmission Electron Microscopy: An Interlaboratory Comparison. *Anal Chem* **92**, 13434–13442 (2020).
27. Babaei-Ghazvini, A., Patel, R., Vafakish, B., Yazdi, A. F. A. & Acharya, B. Nanocellulose in targeted drug delivery: A review of modifications and synergistic applications. *International Journal of Biological Macromolecules* **278**, 135200 (2024).
28. Norizan, M. N. *et al.* Nanocellulose-Based Nanocomposites for Sustainable Applications: A Review. *Nanomaterials (Basel)* **12**, 3483 (2022).

29. Advances in nanocellulose-based composites for sustainable food packaging :: BioResources. https://bioresources.cnr.ncsu.edu/.
30. Taiz, L., Zeiger, E., Møller, I. & Murphy, A. *Fundamentals of Plant Physiology*. (2023). doi:10.1093/hesc/9781605357904.001.0001.
31. Mokshina, N., Chernova, T., Galinousky, D., Gorshkov, O. & Gorshkova, T. Key Stages of Fiber Development as Determinants of Bast Fiber Yield and Quality. *Fibers* **6**, 20 (2018).
32. Fuentes, C. A. *et al.* Effect of the middle lamella biochemical composition on the non-linear behaviour of technical fibres of hemp under tensile loading using strain mapping. *Composites Part A: Applied Science and Manufacturing* **101**, 529–542 (2017).
33. Crang, R., Lyons-Sobaski, S. & Wise, R. Parenchyma, Collenchyma, and Sclerenchyma. in *Plant Anatomy: A Concept-Based Approach to the Structure of Seed Plants* (eds Crang, R., Lyons-Sobaski, S. & Wise, R.) 181–213 (Springer International Publishing, Cham, 2018). doi:10.1007/978-3-319-77315-5_6.
34. Dolan, L. *et al.* Cellular organisation of the Arabidopsis thaliana root. https://dx.doi.org/10.1242/dev.119.1.71.
35. Investigating water transport through the xylem network in vascular plants | Journal of Experimental Botany | Oxford Academic. https://academic.oup.com/jxb/article/65/7/1895/542993.
36. Di Ruocco, G., Di Mambro, R. & Dello Ioio, R. Building the differences: a case for the ground tissue patterning in plants. *Proc Biol Sci* **285**, 20181746 (2018).
37. Passioura, J. B. Water Transport in and to Roots. *Annual Review of Plant Biology* **39**, 245–265 (1988).

38. Marinho, E. Cellulose: A comprehensive review of its properties and applications. *Sustainable Chemistry for the Environment* **11**, 100283 (2025).
39. Lab I - Plant Structure (1). https://ucmp.berkeley.edu/IB181/VPL/Ana/Ana1.html.
40. Gorshkov, O. *et al.* Intrusive Growth of Phloem Fibers in Flax Stem: Integrated Analysis of miRNA and mRNA Expression Profiles. *Plants (Basel)* **8**, 47 (2019).
41. Ezquer, I., Salameh, I., Colombo, L. & Kalaitzis, P. Plant Cell Walls Tackling Climate Change: Biotechnological Strategies to Improve Crop Adaptations and Photosynthesis in Response to Global Warming. *Plants (Basel)* **9**, 212 (2020).
42. Natural Cellulosic Fibers - Textile Fiber Microscopy - Wiley Online Library. https://onlinelibrary.wiley.com/doi/10.1002/9781119320029.ch1.
43. Tan, J., Walford, S.-A., Dennis, E. S. & Llewellyn, D. J. Trichomes at the Base of the Petal Are Regulated by the Same Transcription Factors as Cotton Seed Fibers. *Plant Cell Physiol* **61**, 1590–1599 (2020).
44. Chemical compositions of natural fibres. in *Advanced High Strength Natural Fibre Composites in Construction* 23–58 (Woodhead Publishing, 2017). doi:10.1016/B978-0-08-100411-1.00002-9.
45. Asim, M., Abdan, K. & Jawaid, M. A Review on Pineapple Leaves Fibre and Its Composites - Asim - 2015 - International Journal of Polymer Science - Wiley Online Library. https://onlinelibrary.wiley.com/doi/10.1155/2015/950567.
46. Crônier, D., Monties, B. & Chabbert, B. Structure and Chemical Composition of Bast Fibers Isolated from Developing Hemp Stem. *J. Agric. Food Chem.* **53**, 8279–8289 (2005).
47. Goyal, A., Sharma, V., Upadhyay, N., Gill, S. & Sihag, M. Flax and flaxseed oil: an ancient medicine & modern functional food. *J Food Sci Technol* **51**, 1633–1653 (2014).

48. Allaby, R. G., Peterson, G. W., Merriwether, D. A. & Fu, Y.-B. Evidence of the domestication history of flax (Linum usitatissimum L.) from genetic diversity of the sad2 locus. *Theor Appl Genet* **112**, 58–65 (2005).
49. Woigk, W. *et al.* Interface properties and their effect on the mechanical performance of flax fibre thermoplastic composites. *Composites Part A: Applied Science and Manufacturing* **122**, 8–17 (2019).
50. Chalard, M. *et al.* Flax fibre bundle: A remarkable multi-scale unidirectional composite material. *Composites Part A: Applied Science and Manufacturing* **196**, 108990 (2025).
51. Physical and Mechanical Characterization of Flax Fibers: From Elementary Fiber to Yarn. https://www.mdpi.com/2079-6439/13/7/87.
52. Zhu, J., Zhu, H., Njuguna, J. & Abhyankar, H. Recent Development of Flax Fibres and Their Reinforced Composites Based on Different Polymeric Matrices. *Materials (Basel)* **6**, 5171–5198 (2013).
53. Santos, M., Rodrigues, A. I., Malheiro, A. C. & Bacelar, E. The Landscape of Flax Production: Agronomic Drivers, Crop Management, and Approaches to Emerging Challenges. *Agriculture* **16**, 694 (2026).
54. Singhal, A., Jin, J., Banu, M. & Taub, A. Effect of enzyme retting conditions on bast bundle differentiation and mechanical properties of flax technical fibers. *Industrial Crops and Products* **205**, 117478 (2023).
55. Characterization of flax water retting of different durations in laboratory condition and evaluation of its fiber properties :: BioResources. https://bioresources.cnr.ncsu.edu/.
56. Singhal, A., Banu, M. & Taub, A. Improving the process of stem breaking for damage reduction in extracted natural fibers. *Journal of Manufacturing Processes* **86**, 143–151 (2023).

57. Bidhendi, A. J. & Geitmann, A. Relating the mechanics of the primary plant cell wall to morphogenesis. *J Exp Bot* **67**, 449–461 (2016).

58. Tripathi, D. K. *et al.* An overview on manufactured nanoparticles in plants: Uptake, translocation, accumulation and phytotoxicity. *Plant Physiology and Biochemistry* **110**, 2–12 (2017).

59. Li, W., Biraku, X., Nielsen, E., Taub, A. & Banu, M. Nanoparticle-driven growth enhances mechanical properties of flax stems. *Sci Rep* **15**, 30114 (2025).

60. Cooper, G. M. Photosynthesis. in *The Cell: A Molecular Approach. 2nd edition* (Sinauer Associates, 2000).

61. Alberts, B. *et al.* Chloroplasts and Photosynthesis. in *Molecular Biology of the Cell. 4th edition* (Garland Science, 2002).

62. Singh, S., Wu, X. & Zhang, H. Microbial enhancement of plant nutrient acquisition.

63. Poulose, A. *et al.* Nanocellulose: A Fundamental Material for Science and Technology Applications. *Molecules* **27**, 8032 (2022).

64. Tasnim, R., Wang, L., Parit, M. & Zhang, Y.-J. Interactions of Cellulose Nanofibrils with a Foliar Fertilizer and Wild Blueberry Leaves: Potential to Enhance Fruit Yield. *ACS Agric. Sci. Technol.* **2**, 712–718 (2022).

65. Weiland, K. *et al.* Excellence in Excrements: Upcycling of Herbivore Manure into Nanocellulose and Biogas. *ACS Sustainable Chem. Eng.* **9**, 15506–15513 (2021).

66. McCarthy, C. *et al.* Chemical analysis of elephant dung as a potential organic fertilizer in Malawian agricultural systems: a preliminary study. *Discov Agric* **3**, 283 (2025).

67. McCarthy, C. *et al.* Chemical analysis of elephant dung as a potential organic fertilizer in Malawian agricultural systems: a preliminary study. *Discov Agric* **3**, 283 (2025).

68. Baley, C., Gomina, M., Breard, J., Bourmaud, A. & Davies, P. Variability of mechanical properties of flax fibres for composite reinforcement. A review. *Industrial Crops and Products* **145**, 111984 (2020).

69. Langhorst, A., Rieland, J., Banu, M., LOVE, B. & Taub, A. SUPERCRITICAL FLUID TREATMENTS OF FLAX FIBERS FOR IMPROVED MECHANICAL PROPERTIES. in (2023). doi:10.12783/asc38/36644.

70. Biraku, X. Investigation of Nanoparticles Incorporation During Plant Growth to Improve Natural Fiber Properties. (University of Michigan, 2024).

71. Segal, L., Creely, J. J., MartinJr, A. E. & Conrad, C. M. An Empirical Method for Estimating the Degree of Crystallinity of Native Cellulose Using the X-Ray Diffractometer. *Textile Research Journal* **29**, 786–794 (1959).

72. Otenda, B. *et al.* Starch-Hibiscus-Cellulose Nanofibrils Composite Films as a Model Antimicrobial Food Packaging Material. *Journal of Natural Fibers* **19**, 1–14 (2022).

73. Chylińska, M., Szymańska-Chargot, M. & Zdunek, A. Imaging of polysaccharides in the tomato cell wall with Raman microspectroscopy. *Plant Methods* **10**, 14 (2014).

74. Chen, G., Zhang, B., Zhao, J. & Chen, H. Improved process for the production of cellulose sulfate using sulfuric acid/ethanol solution. *Carbohydrate Polymers* **95**, 332–337 (2013).

75. Sullivan, E. M., Moon, R. J. & Kalaitzidou, K. Processing and Characterization of Cellulose Nanocrystals/Polylactic Acid Nanocomposite Films. *Materials* **8**, 8106–8116 (2015).

76. Koch, K. E. CARBOHYDRATE-MODULATED GENE EXPRESSION IN PLANTS. *Annu Rev Plant Physiol Plant Mol Biol* **47**, 509–540 (1996).

77. KOSHLAND Jr., D. E. Stereochemistry and the Mechanism of Enzymatic Reactions. *Biological Reviews* **28**, 416–436 (1953).

78. Jeandet, P., Formela-Luboińska, M., Labudda, M. & Morkunas, I. The Role of Sugars in Plant Responses to Stress and Their Regulatory Function during Development. *Int J Mol Sci* **23**, 5161 (2022).

79. Standard Test Method for Tensile Strength and Young's Modulus of Fibers. https://store.astm.org/c1557-20.html.

80. Langhorst, A. *et al.* Mechanical property enhancement of flax fibers via supercritical fluid treatment. *Sci Rep* **14**, 18819 (2024).

81. Sadeghi, P. *et al.* Experimental and Statistical Investigations for Tensile Properties of Hemp Fibers. *Fibers* **12**, 94 (2024).

82. Yang, Z. A rapid method for determining Weibull parameters of carbon fiber strength. *Composites and Advanced Materials* **34**, 26349833251366332 (2025).

83. Kumar, R., Mikkelsen, L. P., Lilholt, H. & Madsen, B. Weibull parameters determined from a comprehensive dataset of tensile testing of single carbon fibres. *Data Brief* **55**, 110717 (2024).

84. Griffith, A. A. VI. The phenomena of rupture and flow in solids. *Philos Trans A Math Phys Eng Sci* **221**, 163–198 (1921).

85. Jafarypouria, M., Lomov, S. V. & Abaimov, S. G. The effect of variable fiber diameters in unidirectional fiber-reinforced bundles on stress redistributions around fiber breaks. *International Journal of Solids and Structures* **324**, 113687 (2026).

86. Granda, L. A. *et al.* Semichemical fibres of *Leucaena collinsii* reinforced polypropylene composites: Young's modulus analysis and fibre diameter effect on the stiffness. *Composites Part B: Engineering* **92**, 332–337 (2016).

87. FAOSTAT. https://www.fao.org/faostat/en/#data/QCL.

88. Flax Profile. https://www.agmrc.org/commodities-products/grains-oilseeds/flax-profile.

89. Foulk, J. A., Akin, D. E. & Dodd, R. B. Fiber Flax Farming Practices in the Southeastern United States. *Crop Management* **2**, 1–6 (2003).
90. Ag and Food Statistics: Charting the Essentials - Agricultural Trade | Economic Research Service. https://www.ers.usda.gov/data-products/ag-and-food-statistics-charting-the-essentials/agricultural-trade.
91. Cotton and Wool - Cotton Sector at a Glance | Economic Research Service. https://www.ers.usda.gov/topics/crops/cotton-and-wool/cotton-sector-at-a-glance.
92. History | Discover Flax Opportunities — Join Us Today. *PA Flax Project* https://www.paflaxproject.com/history.
93. Bombeck, P.-L. *et al.* Predicting the most appropriate wood biomass for selected industrial applications: comparison of wood, pulping, and enzymatic treatments using fluorescent-tagged carbohydrate-binding modules. *Biotechnol Biofuels* **10**, 293 (2017).
94. Shu, D. *et al.* Nanocellulose synthesis via synergistic application of solid acid and cellulase. *International Journal of Biological Macromolecules* **291**, 139158 (2025).
95. Ma, H., Guna, V., Raju, T., Murthy, A. N. & Reddy, N. Converting flax processing waste into value added biocomposites. *Industrial Crops and Products* **195**, 116434 (2023).
96. Sellier, J. & Pestana De Jesus, W. Enabling carbon fiber applications across key market sectors. *Chemical Fibers International* **70**, 38–40 (2020).
97. Pultrusion Resins and Their Importance in the Manufacturing Industry. https://www.tencom.com/blog/pultrusion-resins.
98. Eckold, G. Manufacture. in *Design and Manufacture of Composite Structures* 251–304 (Woodhead Publishing, 1994). doi:10.1533/9781845698560.251.

99. Shaw-Stewart, D. & Sumerak, J. E. The pultrusion process. in *Pultrusion for Engineers* 19–65 (Woodhead Publishing, 2000). doi:10.1533/9781855738881.19.

100. Wang, L. *et al.* A Theory-Guided Machine Learning and Molecular Dynamics Approach for Characterizing Fast-Curing Polyurethane Systems. *Polymers* **18**, 679 (2026).

101. Isa, A. *et al.* A Review on Recycling of Carbon Fibres: Methods to Reinforce and Expected Fibre Composite Degradations. *Materials (Basel)* **15**, 4991 (2022).

102. Ateeq, M. A state of art review on recycling and remanufacturing of the carbon fiber from carbon fiber polymer composite. *Composites Part C: Open Access* **12**, 100412 (2023).

103. Butenegro, J. A., Bahrami, M., Abenojar, J. & Martínez, M. Á. Recent Progress in Carbon Fiber Reinforced Polymers Recycling: A Review of Recycling Methods and Reuse of Carbon Fibers. *Materials* **14**, 6401 (2021).

104. Shu, J. *et al.* Recovery of carbon fiber from carbon fiber reinforced polymer waste via microwave molten-carbonate pyrolysis. *Journal of Analytical and Applied Pyrolysis* **183**, 106840 (2024).

105. Ren, Y. *et al.* Evaluation of Mechanical Properties and Pyrolysis Products of Carbon Fibers Recycled by Microwave Pyrolysis. *ACS Omega* **7**, 13529–13537 (2022).

106. Khan, A. *et al.* Low temperature synthesis of carbon fibres from post-consumer textile waste and their application to composites: An ecofriendly approach. *Diamond and Related Materials* **130**, 109504 (2022).

107. Fan, W., Yongzhen Wang, & Liu. Textile production by additive manufacturing and textile waste recycling: a review | Environmental Chemistry Letters | Springer Nature Link. https://link.springer.com/article/10.1007/s10311-024-01726-2.

108. Lim, S. Y., Choi, D., Younis, S. A., Kim, K.-H. & Lee, J. Fabrication of carbon materials from textile waste and their sustainable application toward electrode production. *Renewable and Sustainable Energy Reviews* **226**, 116401 (2026).

109. Materials Market Report, 2023.

110. Minig, C., Reglitz, K. & Steinhaus, M. Odor-Active Compounds in Flexible Polyurethane Materials. *Indoor Air* **2024**, 2415739 (2024).

111. James, D. H. & Castor, W. M. Styrene. in *Ullmann's Encyclopedia of Industrial Chemistry* (John Wiley & Sons, Ltd, 2011). doi:10.1002/14356007.a25_329.pub2.

112. Xu, Z. *et al.* Cascade degradation and upcycling of polystyrene waste to high-value chemicals. *Proceedings of the National Academy of Sciences* **119**, e2203346119 (2022).

113. Yuksel, O. *et al.* Material characterization of a pultrusion specific and highly reactive polyurethane resin system: Elastic modulus, rheology, and reaction kinetics. *Composites Part B: Engineering* **207**, 108543 (2021).

114. Rossignolo, G., Malucelli, G. & Lorenzetti, A. Recycling of polyurethanes: where we are and where we are going. *Green Chemistry* **26**, 1132–1152 (2024).

115. Ponomar, M. *et al.* Sessile Drop Method: Critical Analysis and Optimization for Measuring the Contact Angle of an Ion-Exchange Membrane Surface. *Membranes (Basel)* **12**, 765 (2022).

116. Cox, H. L. The elasticity and strength of paper and other fibrous materials. *Br. J. Appl. Phys.* **3**, 72 (1952).

117. Kwok, D. Y. & Neumann, A. W. Contact angle measurement and contact angle interpretation. *Advances in Colloid and Interface Science* **81**, 167–249 (1999).

118. Mo, Y., Huang, X. & Hu, C. Recent Advances in the Preparation and Application of Bio-Based Polyurethanes. *Polymers* **16**, 2155 (2024).

119. Kumar Ja, Pratim Gas & Gupta. Complementing the circular economy with a life cycle assessment of sustainable hydrogels and their future prospects. in *Sustainable Hydrogels* 489–503 (Elsevier, 2023). doi:10.1016/B978-0-323-91753-7.00010-7.